QUASI-STATIC NONLINEAR ANALYSIS OF A CELESTIAL ICOSAHEDRON SHAPED VACUUM LIGHTER THAN AIR VEHICLE

THESIS

Kyle D. Moore, Second Lieutenant, USAF

AFIT-ENY-MS-18-M-280

DEPARTMENT OF THE AIR FORCE
AIR UNIVERSITY

AIR FORCE INSTITUTE OF TECHNOLOGY

Wright-Patterson Air Force Base, Ohio

AFIT-ENY-MS-18-M-280

QUASI-STATIC NONLINEAR ANALYSIS OF A CELESTIAL ICOSAHEDRON SHAPED VACUUM LIGHTER THAN AIR VEHICLE

THESIS

Presented to the Faculty

Department of Aeronautical Engineering

Graduate School of Engineering and Management

Air Force Institute of Technology

Air University

Air Education and Training Command

in Partial Fulfillment of the Requirements for the

Degree of Master of Science in Aeronautical Engineering

Kyle D. Moore, BS

Second Lieutenant, USAF

March 1, 2018

AFIT-ENY-MS-18-M-280

QUASI-STATIC NONLINEAR ANALYSIS OF A CELESTIAL ICOSAHEDRON SHAPED VACUUM LIGHTER THAN AIR VEHICLE

Kyle D. Moore, BS
Second Lieutenant, USAF

Committee Membership:

Anthony Palazotto, PhD
Chair

William Baker, PhD
Member

Jaimie Tiley, PhD
Member

Abstract

Due to the many drawbacks associated with a traditional lighter than air vehicle (LTAV), there is a desire for a LTAV which generates lift from an internal vacuum. To date, two feasible designs (the icosahedron and the hexakis icosahedron) for this so called vacuum lighter than air vehicle (VLTAV) have been studied at the Air Force Institute of Technology (AFIT). This research looks to show the feasibility of a new design for a VLTAV, the celestial icosahedron. This research includes a boundary condition study which proves the symmetric nature of the celestial icosahedron's frame with laterally constrained and unconstrained vertices. This research also presents three feasible designs of various structural diameters (0.8001, 1.2192, and 0.7576 meters) for the celestial icosahedron.

Acknowledgments

I would like to thank my advisor, Dr. Anthony Palazotto, for his support and guidance throughout my research. I would also like to thank the other committee members for this thesis, Dr. William Baker and Dr. Jaimie Tiley. Dr. Jamie Tiley, from the Air Force Office of Scientific Research, is also the sponsor of this research.

Kyle D. Moore

Table of Contents

Page

List of Figures

List of Tables

List of Acronyms

ADA Americans with Disabilities Act

AFIT Air Force Institute of Technology

CAE Complete Abaqus Environment

CNT carbon nanotube composite

DOF degrees of freedom

FEA finite element analysis

FEM finite element model

FS factor of safety

ISR intelligence, surveillance, and reconnaissance

LTAV lighter than air vehicle

VLTAV vacuum lighter than air vehicle

VM Von Mises

W/B weight-to-buoyancy

List of Symbols

ν	Poisson's Ratio
ρ_a	Mass density of air (kg/m^3)
ρ_s	Mass density of shell (kg/m^3)
a	Acceleration due to gravity (m/s^2)
B_s	Buoyant force of shell (N)
D	Diameter (m)
E	Young's Modulus (Pa)
ft	Feet
g	Grams
kg	Kilograms
m	Meters
N	Newtons
nm	Nanometers (*1e-09 m*)
P_{crit}	Critical pressure (Pa)
Pa	Pascals (N/m^2)
R	Radius (m)
r_{beam}	Beam radius (m)
s	Seconds
t_{beam}	Beam thickness (m)
t_{skin}	Skin thickness (m)
U	Displacement (m)
W_s	Shell weight (N)

QUASI-STATIC NONLINEAR ANALYSIS OF A CELESTIAL ICOSAHEDRON SHAPED VACUUM LIGHTER THAN AIR VEHICLE

I. Introduction

1.1 Chapter Overview

When humans first took flight more than two centuries ago, it was with the use of a lighter than air vehicle (LTAV). The first LTAVs used heated air to generate lift; later, lifting gases such as hydrogen and helium were used. The many drawbacks of traditional LTAVs prompted the development of an alternate design. Instead of using traditional lifting gases, it is possible to generate lift by evacuating the internal air from the vehicle, creating an internal vacuum and giving us a vacuum lighter than air vehicle (VLTAV).

This chapter will outline the research objectives of this thesis, the motivation behind the need for a feasible VLTAV, the background of VLTAVs, as well as the assumptions and methodology of this research.

1.2 Objective

The objective of this thesis is to determine the feasibility of a VLTAV using the celestial icosahedron design. This research looks to accomplish this by characterizing the nonlinear, quasi-static response of the celestial icosahedron design. This will be done using the finite element analysis (FEA) program Abaqus [1]. For this research, a model's factor of safety (FS) is defined as the given material's yield stress divided by its corresponding maximum Von Mises (VM) stress experienced. A model's weight-

to-buoyancy (W/B) ratio is defined as the model's weight divided by the buoyancy produced by the volume it displaces. These results will be compared to the results obtained from similar research conducted on the hexakis icosahedron-shaped VLTAV. The specific research objectives are:

- Modify Brian Cranston's original 0.3048 meter diameter model by removing the skin and applying a loading condition representative of a uniform external pressure equal to sea-level pressure [2]
- Use the modified model to determine which boundary conditions ensure a symmetric response within the frame
- Modify the dimensions (beam thickness/radius, skin thickness, and structural diameter) of Cranston's original 0.3048 meter diameter model using Matlab
- Produce and analyze three feasible VLTAV designs
  - 0.8001 meter diameter model with minimum W/B ratio and FS$\geq$1.50
  - 1.2192 meter diameter model with minimum W/B ratio and FS$\geq$1.15
  - Minimum diameter model with W/B ratio less than 1 and FS$\geq$1.50

1.3 Motivation

For the better part of the last century, LTAV flight has been achieved through the use of lifting gases such as helium and hydrogen. Although LTAVs have a multitude of both military and civilian applications, these traditional LTAVs may not be the optimal design. To start, traditional LTAVs require expensive helium gas to generate lift; although hydrogen weighs less and is more abundant, it is also extremely flammable, deeming it unsafe for LTAV applications. In his paper from 1983, *Lighter*

Than Air Craft Using Vacuum, David Noel states that the biggest drawback of traditional LTAVs is the fact that they leak [3]. Because LTAVs leak their lifting gas, they must keep reserves on board. By keeping reserves of gas on board, the weight of the ship is increased and the potential payload of the ship is reduced. Because only a finite amount of spare gas can be held on board, the ship must eventually come down to refuel thus limiting the vehicle's loiter time.

One way to circumvent these problems is to generate lift via an internal vacuum. By evacuating the air inside of the ship, the net weight of the ship is decreased —no gas at all is lighter than any lifting gas we know of today. By reducing the overall weight of the vehicle, larger payloads can be used. Leaks are still inevitable, even with VLTAVs, due to the structural materials and manufacturing capabilities currently available. With VLTAVs though, lifting gas does not need to be resupplied after it has escaped due to leaks; the air that has seeped into the vehicle can simply be pumped back out using an on-board pump [3]. It is important to note that the inclusion of an on-board pump increases the vehicle's W/B ratio, effectively reducing the weight of the payload able to be carried.

This reveals another advantage of VLTAVs. In order to change altitude, a traditional LTAV must either take on or release ballast to change its buoyancy. Again a vacuum would be able to pump out air when positive buoyancy is needed and let air in when negative buoyancy is desired. Because VLTAVs never need to have their lifting gases refueled, theoretically they would be able to achieve indefinite loiter times [3].

Because VLTAVs could potentially stay afloat far longer than their traditional counterparts, their possible applications are numerous. Noel stated that the most obvious application for a VLTAV is transport, whether it be of people or cargo. The potential endurance and range of VLTAVs would be very beneficial in transporting people and goods very long distances. Another application for VLTAVs that Noel

sees is energy harvesting. He believes that in the future, smaller VLTAVs would be able to loiter at cloud level to harvest water, while larger vehicles equipped with solar arrays could rise above the clouds and collect solar energy [3].

Because of the potential for extended endurance and range, this research will focus on the military-specific applications of VLTAVs that are available. The ability to stay aloft indefinitely is a great asset to intelligence, surveillance, and reconnaissance (ISR). Currently, ISR is predominantly conducted using unmanned aircraft or small ground-based vehicles. Both options have limited mission times and the latter can be limited by adverse terrain. This new technology could potentially lead to an airborne ISR vehicle capable of indefinite loiter times.

1.4 Background

A LTAV that uses an internal vacuum (instead of lifting gases) to generate lift was first proposed in 1663 by the Italian, Jesuit priest, Francesco Lana de Terzi. In the 17th century, Terzi proposed constructing a boat-like structure attached to four thin, copper spheres. The spheres would have all of their internal air evacuated. By doing so, Terzi would take advantage of Archimedes' principle and generate positive buoyancy. With a strong understanding of Archimedes' principle, Terzi was able to theoretically design a LTAV that utilized an internal vacuum to generate lift. What Terzi did not fully understand though, was mechanics of materials and shell buckling. Although Terzi's design would be able to generate positive buoyancy, the structure itself would not survive. In order to create a structure that was light enough to float, the thickness of the spheres would have to be so small, that they would instantaneously buckle under atmospheric pressure [4].

Because Terzi's design was deemed not feasible very early on, VLTAVs have only existed in theory for the last three and a half centuries. In 1983, David Noel wrote

about VLTAVs and championed their advantages over their traditional, lifting gas utilizing, counterparts. In his paper *Lighter Than Air Craft Using Vacuum*, Noel explains the cube-square rule. The cube-square rule states that the volume of a sphere increases as the cube of its radius, while its surface area increases as the square of its radius. The obtainable lift of a hollow sphere with an internal vacuum is proportional to its volume, while the weight of the sphere is proportional to its surface area. Therefore, according to the cube-square rule, Noel says, if the radius of a vacuum were increased enough, lift could be generated no matter the weight of the material used to construct it. Recognizing that no materials exist yet to create a homogeneous spherical shell structure of a reasonable size, Noel first proposes using a more rigid, geodesic sphere design to construct a vacuum [3].

In 2012, an Air Force Institute of Technology (AFIT) master's student, Trent Metlen, proposed a geodesic sphere-like structure that could be used to construct a VLTAV. While working on his PhD dissertation at AFIT, Brian Cranston proposed a second structure. Both designs were composed of a rigid frame structure covered by a membrane-like skin. The first design, the icosahedron, had a frame consisting of 20 equilateral triangles with 12 total vertices. The more spherical hexakis icosahedron had 120 triangles with 62 vertices. Over the last six years, the two designs have been analyzed both quasi-statically and dynamically by subsequent AFIT master's students [5]. Along with the hexakis icosahedron, Cranston proposed another even more spherical design, the celestial icosahedron. This icosahedron design is composed of a frame made up of 9 intersecting rings spaced out and revolved at 45 degree increments. Like the icosahedron's and the hexakis icosahedron's frames, the celestial icosahedron's frame is covered with a thin, membrane-like skin [2],[6].

1.5 Assumptions

One of the major benefits of FEA is the ability to simplify a complex structure into a much simpler, and easier to analyze representative model. In order to obtain valuable information, the assumptions taken into account during the creation and analysis of the model must be known and understood. It is assumed that the mesh produced by Cranston is sufficiently converged.

Although some of the materials being tested are experimental and still in development, it is assumed that they are attainable and manufacturable. It is also assumed that the materials had the isotropic elastic material properties stated and that Schwemmer's findings for the hexakis icosahedron, indicating that a carbon nanotube composite (CNT), with an epoxy resin matrix, frame and a Graphene skin provided the best results (lowest W/B ratio for a given diameter), apply to the analysis of the celestial icosahedron design [7],[8]. To simplify calculations, it is assumed that air acts as an ideal gas. This assumption limits both the operating temperature and altitude of the vehicle. The FS for a given structure is assumed to be the structure's respective material's yield stress divided by the maximum VM stress it experiences.

Reduction of the volume displaced by the structure due to deformation of the frame structure is considered negligible for all buoyancy calculations. All of the results obtained are dependent upon a perfect vacuum existing within the structure of the vehicle. Finally, it is assumed that the boundary conditions modeled can be defined exactly.

1.6 Methodology

In order to characterize the quasi-static, nonlinear response of the celestial icosahedron, four finite element models (FEMs) were produced and analyzed. All four models were based on the original celestial icosahedron model constructed by Brian

Cranston within the FEA program Abaqus's Complete Abaqus Environment (CAE). Because sea-level pressure is the highest pressure the exterior of this structure would ever encounter, all loading conditions were selected in order to simulate a uniform pressure equal to sea-level pressure. The first model was 0.3048 meters in diameter and had no attached membrane (frame only). A system of loads simulating a uniform pressure equal to that at sea-level was applied to this model in order to study the effects that different boundary conditions have on the symmetry of the celestial icosahedron's quasi-static, nonlinear response. CNT's material properties were used to model the frame. Convergence issues during analyses of the icosahedron and the hexakis icosahedron demonstrated the need for boundary conditions. Finally, a linearity study was conducted on the models in which the the magnitude of the deformation at a specific point on the frames was tabulated and plotted against the corresponding percentage of the total applied load at given increments. For all analyses following the boundary condition study, the boundary condition which produced symmetry was used.

The next three models represented the full structure, a frame structure covered by a thin, membrane-like skin. These models are modifications of Cranston's original 0.3048 meter model. Part dimensions (beam radius/thickness and skin thickness), as well as the structural diameter of the original model were modified using the Matlab script found in Appendix B. The frame was modeled using CNT's material properties, and the skin was modeled using Graphene's material properties. All part dimensions take into account the respective materials' smallest manufacturable dimensions, to include the minimum c-ratio for the beams. C-ratio is the ratio of the beams thickness to its radius. A quasi-static, nonlinear step was used to characterize the model's response to a uniform pressure equal to that of sea-level pressure. The first two full models (frame and skin) had fixed structural diameters (0.8001 and 1.2921 meters

respectively) while the third had a variable diameter that was to be optimized. The Matlab script (Appendix B) was also used to compare iterations' respective FS as well as W/B ratios for each of these models.

For the final iterations of all three models, the same point that was tracked for the frame only models was tracked to highlight the effect of the addition of a skin on the linearity of the models' responses. Additionally, a point within the skin was tracked as well. Results of both the boundary condition study as well as the full structure analyses were then compared to the results of the icosahedron and the hexakis icosahedron respectively.

1.7 Overview

- Chapter I: Thesis objective, motivation, background, assumptions, and methodology
- Chapter II: Theoretical and historical overview, as well as background of previous research
- Chapter III: Detailed methodology
- Chapter IV: Analysis results and discussion
- Chapter V: Summary of results and conclusions, as well as recommendations for future research

II. Literature Review

2.1 Chapter Overview

The earliest recorded occurrences of manned and unmanned flight utilized lighter than air vehicle (LTAV) technology, and for the last few centuries, humans have been experimenting with the idea of a vacuum lighter than air vehicle (VLTAV), a LTAV that uses an internal vacuum to achieve positive buoyancy.

Although initial studies took place during the later years of the Renaissance, research on VLTAVs has been conducted at the Air Force Institute of Technology (AFIT) by the master's and doctoral students T. Metlen (2012), R. Adorno-Rodriguez (2014), M. AlGhofaily (2015), L. Just (2015), B. Cranston (2016), J. Schwemmer (2017), and J. Snyder (2017) over the last six years. These researchers analyzed, both quasi-statically and dynamically, the icosahedron and hexakis icosahedron VLTAVs. Their work is used as guidance in the analysis of the celestial icosahedron VLTAV.

In order to analyze the celestial icosahedron, finite element analysis (FEA) is utilized. A nonlinear-solution method is necessary in order to characterize the structure's behavior under the loading of a uniform pressure equal to standard sea-level pressure directed towards the center of the structure. The Newton-Raphson solution method will be explained in detail.

While previous designs for VLTAVs have been analyzed using the material properties for a variety of different structural materials, the celestial icosahedron design is analyzed using the material properties for a carbon nanotube composite (CNT) (frame material) and Graphene (skin material). Schwemmer's research showed that CNT and Graphene preformed best during his analysis of the hexakis icosahedron [7],[8]. CNT and Graphene, as well as their respective properties, will be discussed in this chapter.

2.2 Lighter Than Air Vehicles

2.2.1 Theory

LTAVs take advantage of Archimedes' principle in order to generate lift. Archimedes' principle, illustrated in Figure 2.1, states that an object immersed in a fluid is acted upon by a force equal to the weight of the fluid displaced by the object [9]. If this upward force is greater than the overall weight of the object, positive buoyancy is generated. The concept described here is that of the weight-to-buoyancy (W/B) ratio (specifically a W/B<1). In order to generate an upward force greater than the overall weight of the vehicle (W/B<1), traditional LTAVs must be filled with a fluid that is less dense than the surrounding fluid. Historically, lighter than air gases, such as hydrogen and helium, have been used to accomplish this task.

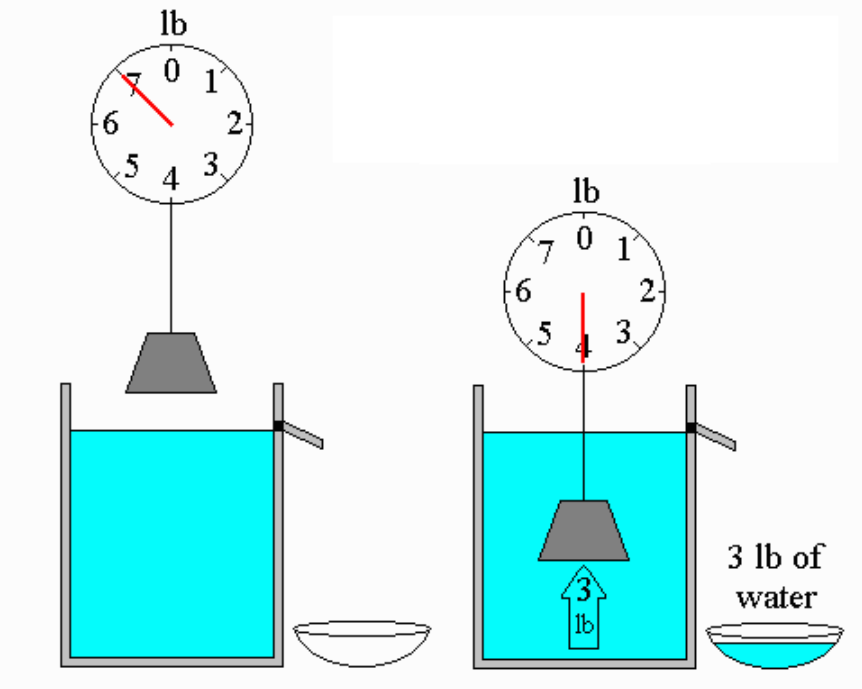

Figure 2.1. Archimedes' Principle illustrated with a 7 lb weight [10]

2.2.2 Historical Lighter Than Air Vehicles

As early as the 3rd century BC, LTAV technology has been utilized in the form of small, unmanned, Chinese signaling lanterns. These lanterns, known now as Kong-ming lanterns, were essentially small, unmanned hot-air balloons [11]. During the last three centuries, LTAVs have been used extensively in various manned applications as well. In 1783 Jean-François Pilâtre de Rozier conducted the first untethered, piloted flight when he ascended 3,000 feet over Paris in a Montgolfier brothers-designed hot-air balloon [12]. Hot-air balloons heat the air inside of a balloon suspended over a basket. Once heated, the air inside of the balloon becomes less dense than the surrounding air. The vehicle's overall W/B ratio drops below 1, positive buoyancy is achieved, and lift is generated. As early as the American Civil War, hot-air balloons were being used in intelligence, surveillance, and reconnaissance (ISR) missions.

Less than 150 years after the first untethered, piloted flight using a LTAV, Count Ferdinand von Zeppelin founded the German Airship Travel Corporation which conducted regular, nonstop transatlantic flights using rigid airships like the one shown in Figure 2.2 [13]. Various types of LTAVs have been used throughout history; modern LTAVs can be classified as having a rigid, semi-rigid, or non-rigid structure [12].

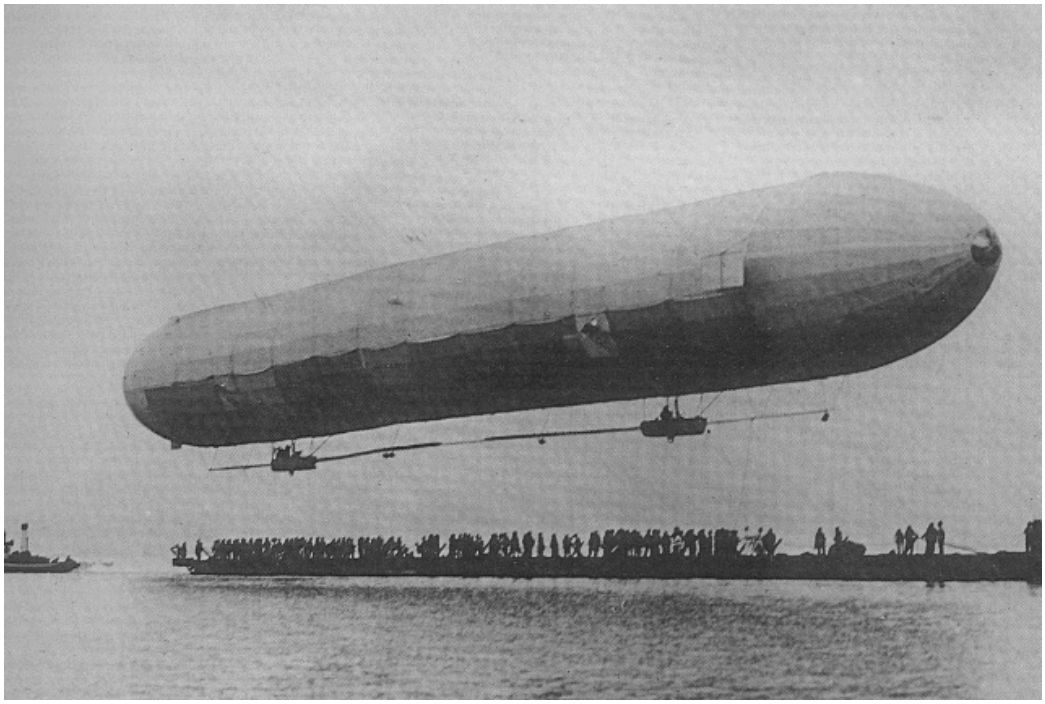

Figure 2.2. The first successful rigid airship, the Zeppelin LZ 1 [14]

Rigid airships are composed of a rigid frame covered by a membrane. The lifting gas for a rigid airship is contained in cells within the structure. Semi-rigid airships are similar to rigid airships except for the way with which the lifting gas is stored. The lifting gas is stored within the pressurized structure itself, held in by the membrane. A non-rigid airship has no rigid frame. Instead, the membrane is pressurized and given its shape by the lifting gas alone. Non-rigid airships are commonly referred to as blimps [12].

Throughout history, all operational LTAVs have utilized a lifting gas in order to create positive buoyancy (W/B<1). Up until the last century, hydrogen was the most commonly used lifting gas in LTAVs. Although helium is less abundant and slightly more dense than hydrogen, helium has taken over as the most popular lifting gas in LTAVs due to hydrogen's flammability. The world is in the midst of a massive helium shortage, with prices expected to increase dramatically over the next few years [15]. Because of this potential increase in cost, engineers are looking to LTAVs that utilize

alternative means of creating lift.

One such alternative to using helium as a lifting gas is to not use a lifting gas at all. For centuries, engineers have proposed, but not yet constructed, a LTAV that uses an internal vacuum to generate lift. The first LTAV that used an internal vacuum instead of a lifting gas was proposed by the Italian Jesuit priest, Francesco Lana de Terzi, in 1670. Terzi's flying ship concept utilized four thin, 7.5 meter diameter, copper spheres with internal vacuums to generate positive buoyancy [16]. These spheres would be mounted over a ship-like structure which could carry people and supplies. A sail would also be attached to steer the vehicle. Terzi, in effect, proposed the world's first VLTAV. Terzi's calculations do indeed work out; if the air could be completely evacuated from the four spheres, enough air could be displaced by the structure to decrease the W/B ratio to a value below 1.

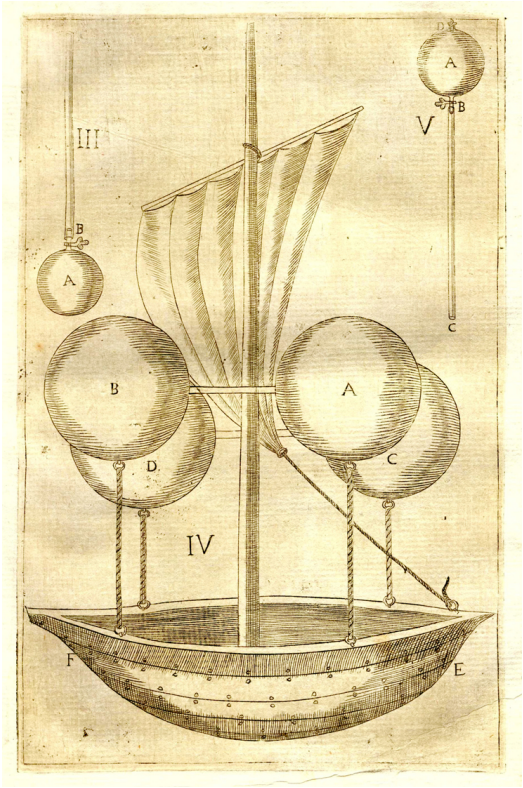

Figure 2.3. Illustration of Terzi's flying ship concept [4]

From the very beginning, critics of Terzi claimed that the thin-walled spheres would not be strong enough to withstand the surrounding atmospheric pressure once all of the internal air has been evacuated. Terzi's critics were correct, the proposed shells were too thin to achieve the required rigidity to withstand atmospheric pressure. Although not yet discovered in the 17th century, what Terzi's critics were describing was shell buckling. Had the thickness of the shells been increased to prevent buckling, the overall weight of the assembly would have been too heavy to achieve positive buoyancy. Given the materials available during Terzi's time, the flying ship concept was not feasible.

To this day, shell buckling still presents a challenge. No known material in the form of a homogeneous shell is able to withstand atmospheric pressure while maintaining an internal vacuum. In their 2006 patent, A. Akhmeteli and A. Gavrilin mathematically proved this as shown in Equations (2.1) - (2.7) [17],[18],[19].

The weight of and the buoyant force produced by a spherical thin-walled shell are given by Equations (2.1) and (2.2) respectively. Where R is the radius of the sphere, t is the thickness of the shell, a is the acceleration due to gravity, and ρ_s and ρ_a are the mass densities of the shell's material and air respectively.

$$W_s = 4\pi R^2 t \rho_s a \tag{2.1}$$

$$B_s = \frac{4}{3}\pi R^3 \rho_a a \tag{2.2}$$

Equation (2.3) shows that for any structure to be positively buoyant, its weight must be less than the buoyant force it generates.

$$W_s < B_s \tag{2.3}$$

Substituting Equations (2.1) and (2.2) into Equation (2.3) and solving for t gives Equation (2.4). This is the shell thickness necessary for positive buoyancy.

$$t < \frac{R}{3}\frac{\rho_a}{\rho_s} \tag{2.4}$$

Substituting Equation (2.4) into the critical pressure Equation (2.5) from classical buckling theory gives Equation (2.6). Where E and ν are the shell material's Young's Modulus and Poisson's ratio respectively.

$$P_{crit} = \frac{2ER^2}{\sqrt{3(1-\nu^2)}}\frac{1}{R^2} \tag{2.5}$$

$$P_{crit} = \frac{2E\rho_a^2}{\sqrt{3(1-\nu^2)}}\frac{1}{9\rho_s^2} \tag{2.6}$$

In order to compare different materials' resistance to buckling, a strength-mass per unit volume ratio can be solved for by isolating (E/ρ_s^2) in Equation (2.6). Equation (2.7) represents the required strength-mass density ratio to prevent shell buckling.

$$(E/\rho_s^2) = \frac{9P_{crit}\sqrt{3(1-\nu^2)}}{2\rho_a^2} \tag{2.7}$$

To determine the (E/ρ_s^2) requirement for a spherical thin-walled homogeneous shell at sea-level pressure, set P_{crit} equal to atmospheric pressure at sea-level (101,325 *Pascals*), ρ_a is equal to 1225 kg/m^3 [20], and assume that ν is equal to *0.33*. This gives a (E/ρ_s^2) equal to 496,799.10 $m^7/(kg \cdot s^2)$. A value far higher than any known materials' (E/ρ_s^2) today [17].

Because of this material limit preventing the use of a homogeneous shell structure, Akhmeteli and Gavrilin then proposed a non-homogeneous layered shell in which a "thick honeycombed section sandwiched between and bonded to two relatively thin layers" created a thin-walled sphere.

This layered wall structure provides geometric stiffening and prevents the shell buckling that occurs in homogeneous shells constructed from existing materials [17].

2.3 Previous AFIT Research

Because geometric stiffening is still the only feasible solution to the shell buckling problem, the AFIT students previously mentioned proposed and analyzed stronger, geodesic sphere-like rigid frames covered by a membrane that could support atmospheric pressure while maintaining an internal vacuum
[2],[5],[6],[7],[8],[18],[19],[21],[22],[23],[24],[25].

Although a sphere offers the most internal volume for the smallest surface area (large volume-surface area ratio), and therefore the most lift, the buckling problem led Metlen and the other researchers to propose and analyze an icosahedron-shaped frame with 20 faces and 12 vertices. For large structural diameters though, the difference in volume-surface area ratios between the icosahedron and a sphere is substantial. Increasing the diameter of the structure results in a considerable difference in lift that is able to be generated for the two different shapes. Because lift is decreased as the frame becomes less spherical, it is beneficial to create the most spherical frame possible while maintaining structural rigidity. An improvement on the icosahedron is the hexakis icosahedron that was proposed by Cranston. The hexakis icosahedron has 120 faces and 62 vertices producing a structure more spherical than the icosahedron [2],[5],[6],[7],[8],[18],[19],[21],[22],[23],[24],[25]. The icosahedron design and the hexakis icosahedron design are shown Figure 2.4.

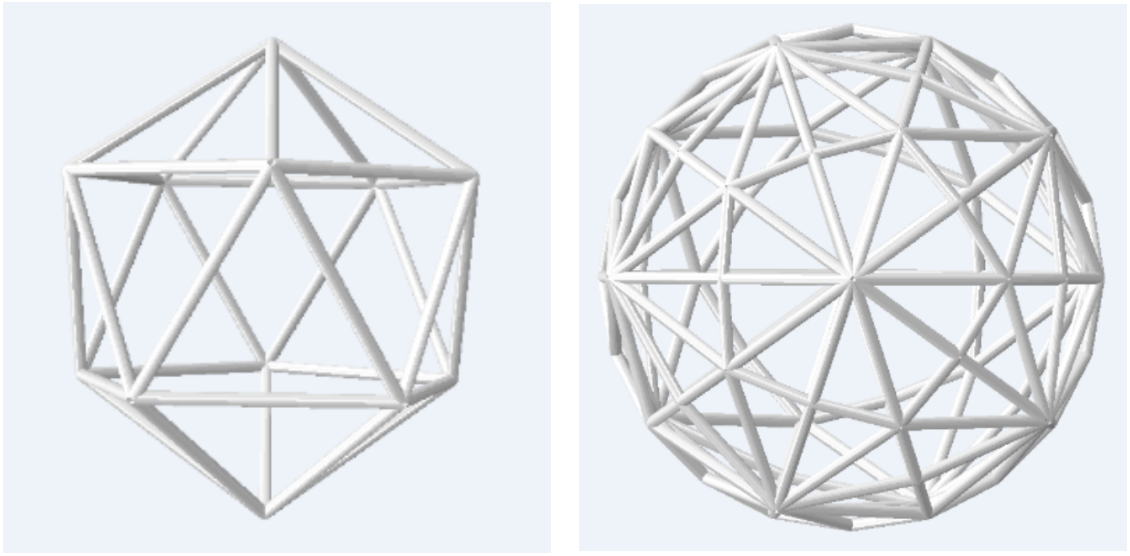

(a) **(b)**

Figure 2.4. The icosahedron (a) and hexakis icosahedron (b) frames [21]

In 2012, Metlen proposed two different methods of geometrically stiffening a sphere. He ultimately settled on a geodesic sphere composed of a frame made up of cylindrical rods, covered by a thin membrane-like skin. Metlen performed linear quasi-static analysis on variations of this geodesic sphere design, the icosahedron, using the FEA program, Abaqus. Metlen also carried out efficiency and W/B studies as well. Adorno-Rodriguez studied Metlen's icosahedron design using quasi-static nonlinear FEA. In characterizing the icosahedron's structural response, Adorno-Rodriguez discovered that membrane behavior dominates the skin's response and geometric stiffening is generated throughout the structure. The overall buoyancy of the structure was not significantly effected by the skin's displacement ($\leq$4% reduction). Although material advancements are necessary, Adorno-Rodriguez determined that it would be feasibly possible to manufacture an icosahedron VLTAV in the near-future [5],[23],[24].

In 2015, AlGhofaily verified quasi-static nonlinear FEA of the icosahedron through experimental testing of additively manufactured scale models. He subjected the structure to a compressive load and observed its response. Just conducted a dynamic

analysis of the icosahedron design, validating previous FEA with experimental modal analyses. Just investigated a previously observed snapback response while himself observing chaotic behavior in the frame under certain loading and boundary conditions [18],[19],[25].

The next year, Cranston experimentally validated previous FEA on the icosahedron model. He then went on to study the feasibility of Metlen's icosahedron, as well as his new hexakis icosahedron and celestial icosahedron designs. Cranston concluded that the icosahedron was not feasible using real materials that could be manufactured due to material failure while the hexakis icosahedron yielded promising results. Further research on the celestial icosahedron design is necessary in order to determine its feasibility. Schwemmer quasi-statically analyzed and optimized the hexakis icosahedron design. He sought to minimize the diameter of the structure while maintaining structural rigidity as well as positive buoyancy (W/B<1). Schwemmer tested different combinations of structural materials as well as part dimensions, ultimately producing two feasible designs with structural diameters of 1.2192 and 4.5720 meters (4 and 15 feet respectively). Both designs have a CNT frame, with the 1.2192 meter design having a Graphene skin and the 4.572 meter design having a Spectra skin. The 1.219 meter design had a W/B ratio of 0.7654 and the 4.5720 meter design had a W/B ratio of 0.9907. Snyder continued research on the hexakis icosahedron, conducting both FEA and experimental analysis of the design. Snyder looked at both the quasi-static nonlinear response, as well as the dynamic response [2],[6],[7],[8],[21],[22].

2.4 The Celestial Icosahedron Design

As was previously discussed, a perfectly spherical structure results in an optimal W/B ratio for any given structural diameter. In his research, Cranston constructed the most spherical icosahedron design to date, the celestial icosahedron. The celestial

icosahedron differs from the icosahedron and hexakis icosahedron in that its frame is not composed of flat, connected triangular faces. Instead, the celestial icosahedron's frame is made up of 9 intersecting rings, spaced out and revolved at 45 degree increments as seen in Figure 2.5 [2],[6].

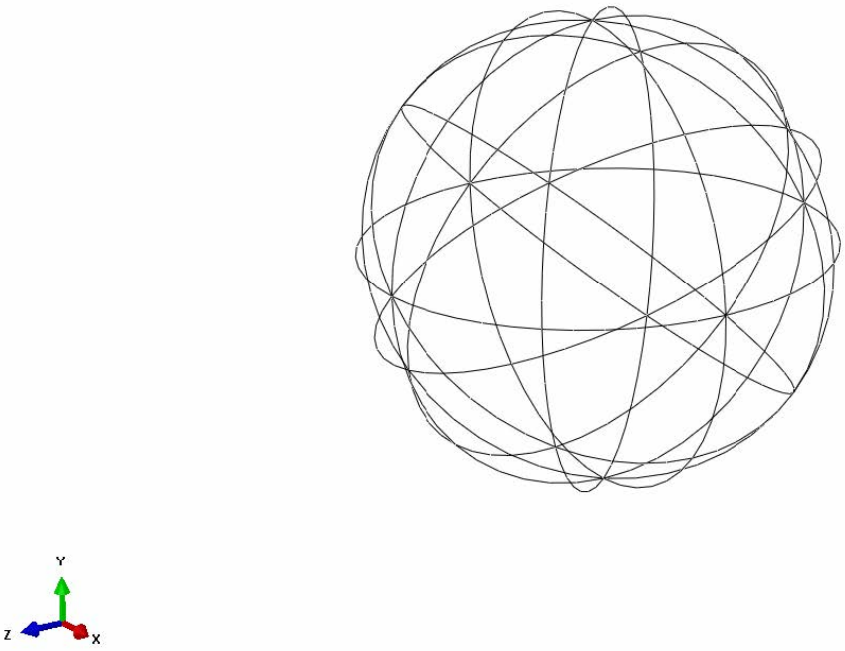

Figure 2.5. Celestial icosahedron frame

The intersecting rings form 48 curved, spherical triangles of equal area. Like the icosahedron and the hexakis icosahedron, the celestial icosahedron is covered with a thin, membrane-like skin. Cranston built the original 0.3048 meter diameter finite element model (FEM) using Abaqus's Complete Abaqus Environment (CAE). The frame is modeled with 552 B31 beam elements and the skin is modeled with 1827 M3D4R membrane elements. Cranston conducted very little analysis of the celestial icosahedron design, only running analyses for a structure made entirely out of Spectra

1000 with a beam radius of 2.23e-03 meters, a beam thickness of 1.11e-04 meters, and a skin thickness of 1.92e-05 meters [2],[6].

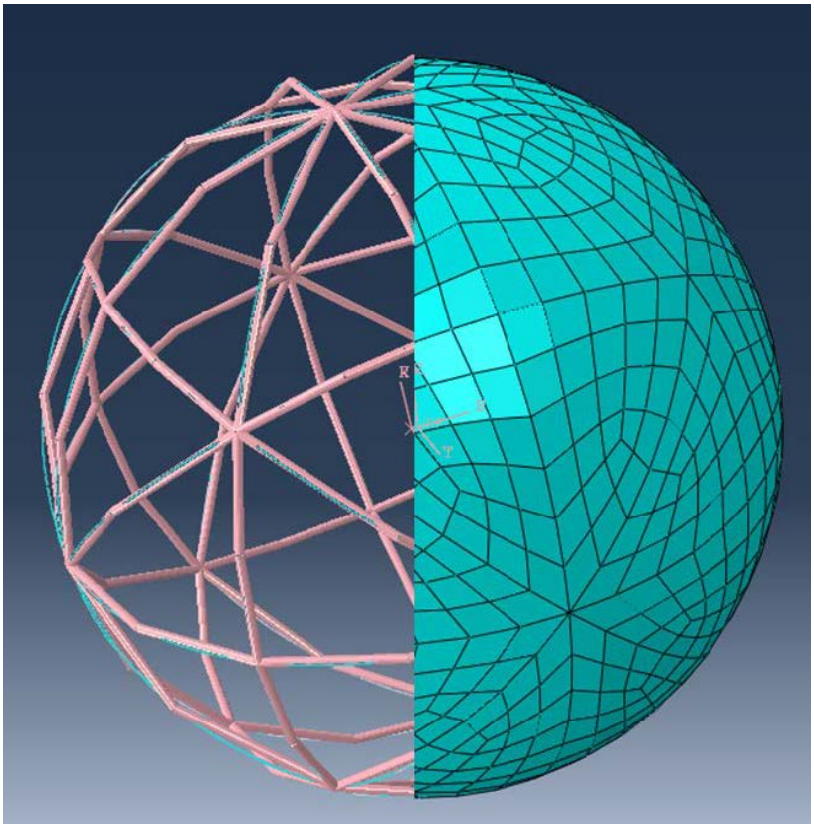

Figure 2.6. Cutaway of frame structure with attached skin

2.5 Structural Materials

Had Terzi's flying ship been constructed, it would have failed due to the homogeneous copper spheres' inability to provide the required strength while being light enough to float. The (E/ρ_s^2) of copper is 1379.40 $m^7/(kg \cdot s^2)$ [26]. This value is far lower than the required (E/ρ_s^2) calculated in Section 2.2.2. Today, almost three and a half centuries later, there are still no materials available that meet this requirement.

Because the materials do not exist to create a homogeneous shell strong enough to resist atmospheric pressure at sea level alone without a supporting frame, the AFIT students previously mentioned have studied a variety of different structural

material combinations for the frame and skin of both the icosahedron and the hexakis icosahedron. The materials tested include: Beryllium, CNT, Graphene, and Spectra. The latest AFIT research into VLTAVs shows that a CNT, with an epoxy resin matrix, frame covered with a Graphene skin performs best [7],[8].

Although Graphene's most well-known property is its strength-weight ratio (the best of any current material), Graphene also acts as an impenetrable barrier. Structural materials that do not leak in air are crucial for VLTAVs. Although CNT and Graphene have very desirable material properties (Table 2.1), there are manufacturing limits for these materials. These manufacturing limits have prevented optimal solutions in the past. For a CNT frame, the smallest manufacturable beam radius and thickness is 8.00e-03 meters and 2.00e-04 meters respectively. Cranston also noted that a beam constructed of CNT must have a c-ratio$\geq$0.020. For structural diameters less than 1.524 meters, Schwemmer showed that optimal results were achieved with a c-ratio=0.025. The smallest manufacturable Graphene skin thickness is 3.30e-10 meters [2],[6],[7],[8].

Table 2.1. Structural material properties

Material	Density (kg/m^3)	Poisson's Ratio	Young's Modulus (GPa)	Yield Stress (GPa)
CNT	1250	0.33	293	3.8
Graphene	2000	0.10	500	50

2.6 Finite Element Analysis Theory

Because of the complex geometry of the structure being analyzed for this research, FEA is utilized. The finite element method is a numerical method which is useful in solving for complex problems in the statics and dynamics field as well as other domains such as heat transfer [27].

In order to solve a problem using FEA, the problem must first be classified. It is up to the modeler to decide whether the analysis must take into account details such as nonlinear behavior, dynamic effects, buckling, and so on [27]. Without proper classification of the problem, an accurate model cannot be produced. The lack of automatic problem classification is one of the drawbacks of current FEA software available to engineers today.

A model problem must then be generated. It is important to decide which features of the actual specimen are important to the analysis and must be represented in the model. For example, depending on the analysis being done certain distributed loads may be able to be represented as point loads, some complex geometries may be simplified, and so on. A modeler makes these decisions based on what information is needed from the analysis, computational cost, and the degree of accuracy required from the analysis. Once the analyst has a model problem, they may use an FEA software package to carry out the preprocessing, numerical analysis, and postprocessing steps [27].

During the preprocessing step, the modeler must input data that describes various details of the model such as geometry, material properties, loads, and boundary conditions. A mesh must then be created that discretizes the model into nodes and elements. It is important for the modeler to choose elements that accurately represent the information that needs to be obtained [27].

The modeler then submits the meshed model for numerical analysis which is done automatically by the FEA solver. The FEA solver generates matrices that describe the behavior of each element, which are then combined to create a global matrix for the entire structure. This matrix is used to solve equations that describe the model's behavior at each of the nodes. The exact calculations carried out are dependent on the problem classification from the first step. Once the numerical analysis is completed,

the FEA software presents the solution in a graphical form. Once again, it is up to the analyst to tell the software the specifics of which outputs are needed [27].

For all of the analyses carried out for this research, B31 beam elements were used to model the frame structure and M3D4R membrane elements were used to model the skin. B31 elements are three-dimensional, 2-node linear, Timoshenko beam elements. Abaqus's user's manual states that the software "assumes that the transverse shear behavior of Timoshenko beams is linear elastic with a fixed modulus and, thus, independent of the response of the beam section to axial stretch and bending." M3D4R elements are three-dimensional, four-node membrane elements with reduced integration. According to the Abaqus User's Manual, membrane elements should be "used to represent thin surfaces in space that offer strength in the plane of the element but have no bending stiffness" [1]. Illustrations of the B31 and M3D4R elements, along with their respective degrees of freedom can be found in Figures 2.7 and 2.8.

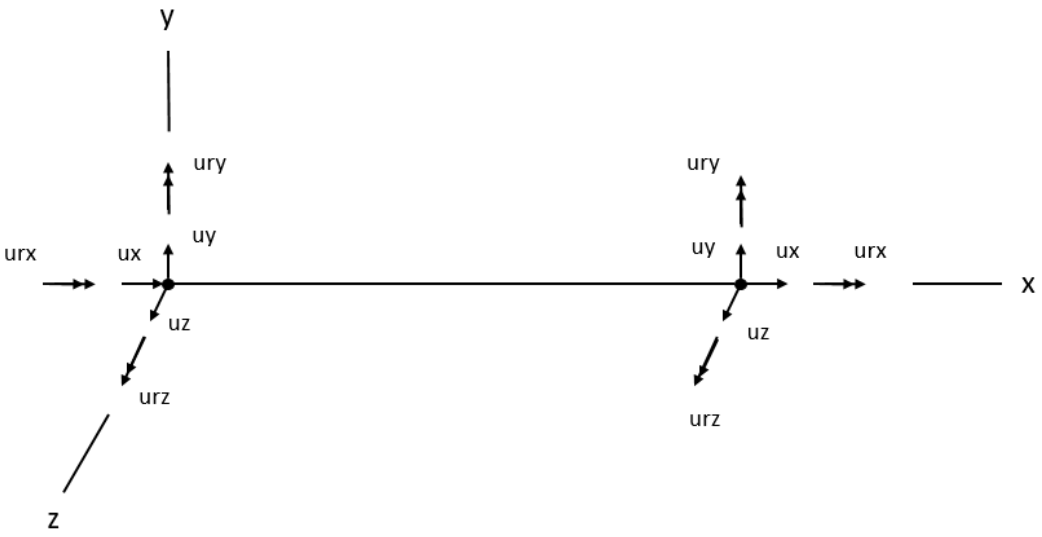

Figure 2.7. B31 beam element and its degrees of freedom

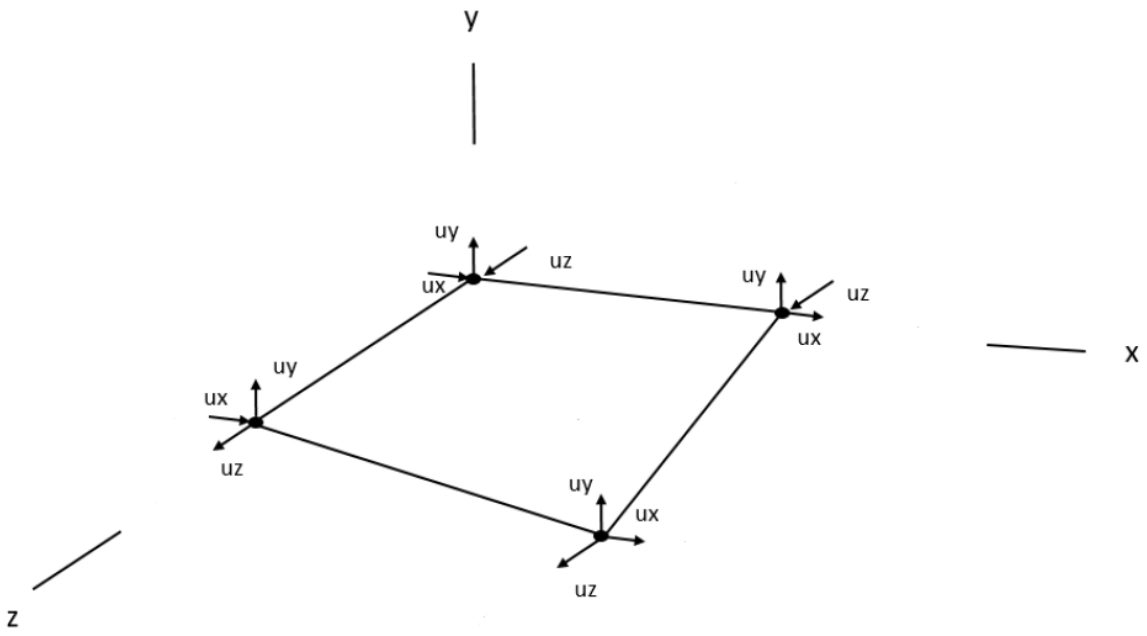

Figure 2.8. M3D4R membrane element and its degrees of freedom

Adaptive automatic stabilization was also used in the analyses for this research. Adaptive automatic stabilization reduces instabilities and eliminates rigid body modes which can have negative effects on the solution in a model which uses membrane elements. An adaptive stabilization scheme differs from a scheme with a constant damping factor in that the damping factor can vary spatially and temporally. Abaqus's user manual states that "the damping factor is controlled by the convergence history and the ratio of the energy dissipated by viscous damping to the total strain energy" [1]. Adaptive automatic stabilization gives the membrane elements the ability to handle transverse loads.

2.6.1 Nonlinear Solution

Nonlinearity in a structural problem may result from material nonlinearity, contact nonlinearity, and geometric nonlinearity. In structural mechanics, problems become nonlinear because the model's stiffness becomes dependent on deformation. This can

also lead to the applied load becoming a function of deformation [21],[22],[27].

$$[K]\{D\} = \{R\} \tag{2.8}$$

In a linear system, both the stiffness, [K],and the reactions, {R}, are independent of the structure's response and the FEA structural equation, Equation (2.8), can be solved easily using linear algebra. The degrees of freedom (DOF), {D}, cannot be solved without knowing [K] and {R} but those quantities cannot be determined without first solving for {D} in a nonlinear system. If the system is nonlinear, Equation (2.8) cannot be used to solve for {D} and a nonlinear solution method must be used [21],[22],[27].

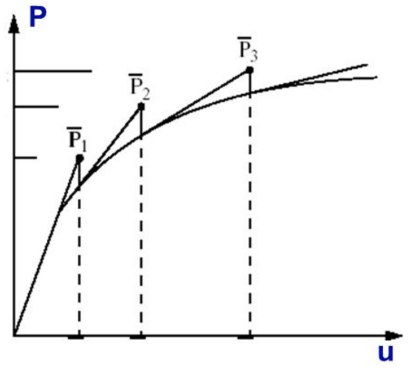

Figure 2.9. Graphical representation of the Newton-Raphson Method

One nonlinear solution method is Newton-Raphson (this is the solution method Abaqus Standard uses for nonlinear analysis). The following is an application of Newton-Raphson to generate a P versus u curve for a nonlinear spring. This relationship is represented in Equation (2.9) where k, u, and P represent the stiffness coefficient, displacement, and load respectively [21],[22],[27].

$$ku = P \tag{2.9}$$

At $t = 0$, $u_0 = 0$ is assumed and the load, P_1, is applied. The displacement at the end of the first increment, u_1 will now be estimated. The first increment is governed by Equation (2.10) where k_0 is the initial spring stiffness, u_A is the initial estimate of u_1, and ΔP_1 is equal to P_1 because the initial load was assumed to be 0 [21],[22],[27].

$$k_0 u_A = \Delta P_1 \tag{2.10}$$

After the first increment is completed, the error is calculated using Equation (2.11) where ku_A represents the resistive force of the spring at that state [21],[22],[27].

$$e_A = P_1 - ku_A \tag{2.11}$$

After one increment, the estimate is not exact and more increments must be executed in order to reduce the error. The second increment moves from point A to point B and is represented by Equation (2.12) [21],[22],[27].

$$k_A \Delta u = e_A \tag{2.12}$$

Equation (2.13) gives the error calculation after the second increment where u_B=Δu+u_A [21],[22],[27].

$$e_B = P_1 - ku_B \tag{2.13}$$

After a sufficient number of increments have been carried out, ΔP_2 is applied and the process is repeated. Accuracy of the solution can be increased by taking more increments as well as reducing the size of those increments [21],[22],[27].

2.7 Summary

In this chapter, the theory behind LTAVs was briefly explained. LTAVs have been ubiquitous in human flight for more than 250 years. The many drawbacks of traditional LTAVs has limited their usefulness in ISR and brought about the need to improve upon the concept.

One alternative to traditional LTAVs are VLTAVs, which use an internal vacuum to generate lift. Previous AFIT students have experimented with different structures and materials with the goal of producing a feasible VLTAV for ISR use. By implementing quasi-static nonlinear FEA, a new design, the celestial icosahedron, can be studied.

III. Research Methodology

3.1 Chapter Overview

To date, no in depth analyses have been conducted on the feasibility of the celestial icosahedron as a design for a vacuum lighter than air vehicle (VLTAV). Because no physical celestial icosahedron exists yet, it is necessary to construct a model in order to run analyses on the structure. In order to generate an accurate representation of the celestial icosahedron's response to a quasi-static, nonlinear loading condition, an accurate finite element model (FEM) must be submitted for analysis [2],[6].

The model used for this research was created by Cranston in the Complete Abaqus Environment (CAE). Cranston's original model is 0.3048 meters in diameter; the model consists of a frame structure, meshed with 552 B31 beam elements (Figure 3.1), covered by a skin, meshed with 1827 M3D4R membrane elements (Figure 3.2) [2],[6].

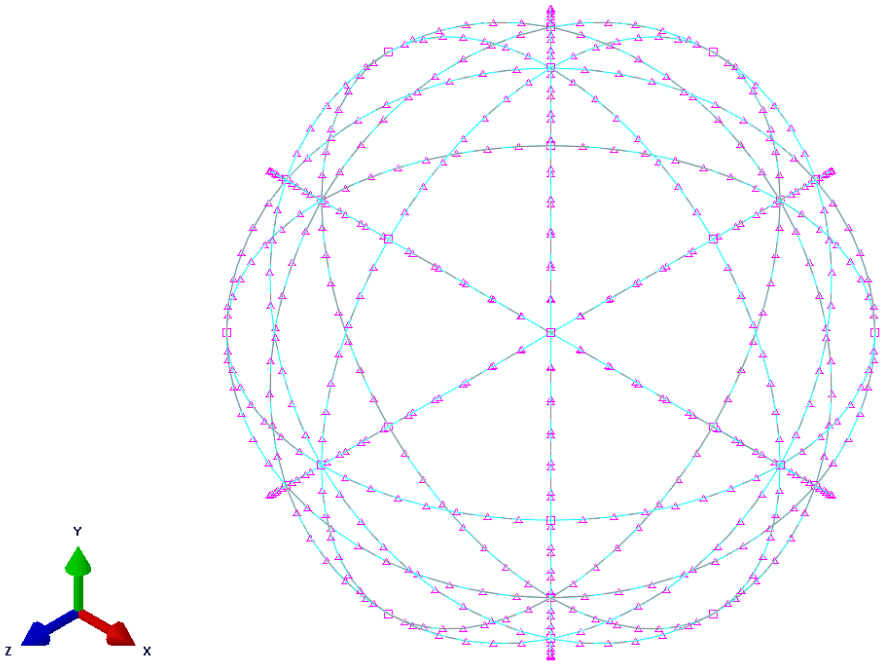

Figure 3.1. 552 B31 element mesh of the frame part

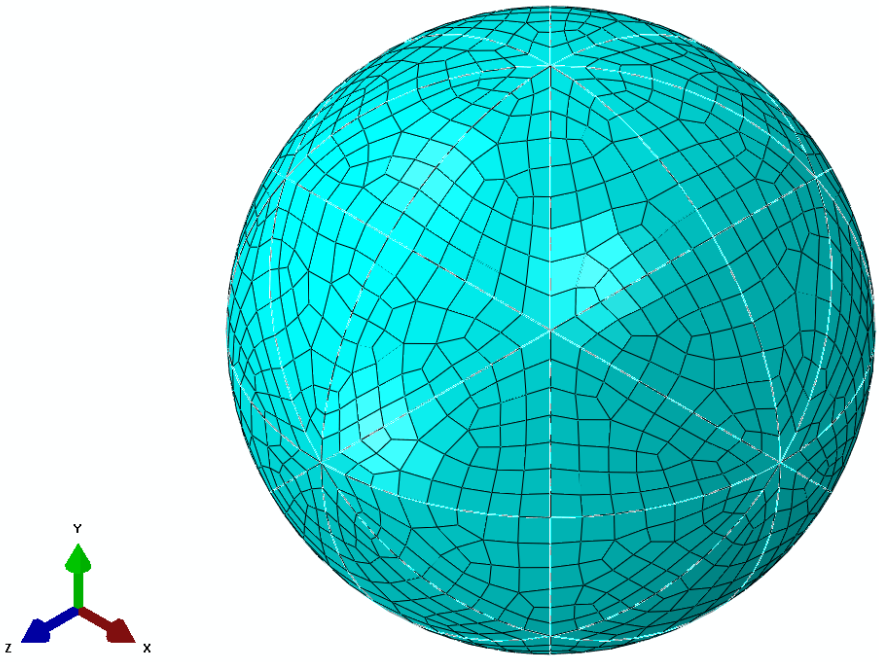

Figure 3.2. 1827 M3D4R element mesh of the skin part

The frame structure is modeled as a set of thin walled pipes with radii and thicknesses equal to 2.23e-03 and 1.11e-04 meters respectively. Cranston's original model's skin thickness is 1.92e-05 meters and both the frame and skin are modeled using the material properties of Spectra. The input file for this model has been extracted from CAE and incorporated into a Matlab script (Appendix B) for model modification and results extraction. This chapter will cover the boundary condition study as well as the analysis of the three full models produced for this research. The three full models include two models with fixed structural diameters of 0.8001 and 1.2921 meters respectively, as well as a model with the smallest achievable diameter. The significance of these diameters will be discussed in the following sections.

3.2 Boundary Condition Study

The actual structure will have no boundary conditions while in operation. During flight, the entire structure will be free to move and be completely unconstrained. For

the full FEM, boundary conditions are needed in order for the model to run. Without boundary conditions, singularities occur. This phenomena was also observed by Adorno-Rodriguez. In order to most accurately model a realistic flight condition, non-intrusive boundary conditions that maintain symmetry must be used. To determine which boundary conditions yielded these results, a boundary condition study similar to the one conducted by Adorno-Rodriguez for the icosahedron was carried out [23],[24].

Like Adorno-Rodriguez's boundary condition study, the boundary condition study for the celestial icosahedron sought to characterize the effects of different boundary conditions on the symmetry of the structure's response. This was done by removing the skin from the frame, and comparing the frame's response under the different boundary conditions [23],[24].

Because Cranston's original model (frame and skin) is loaded using a uniform pressure equal to that of sea-level pressure (101,325 Pascals) directed towards the center of the structure, the model for the boundary condition study (frame only) needs a modified loading condition which simulates a uniform pressure equal to sea-level pressure directed towards the center of the structure. This is done by first placing a reference point at the center of gravity at each of the 48 curved, spherical triangles made up by the intersecting rings of the frame. The center of gravity of any geometric entity within the structure can be found using the query function within CAE. Those 48 reference points are then tied to the beams which make up the triangle they are surrounded by using a coupling constraint (all rotational degrees of freedom are constrained). A reference point can be seen tied to its surrounding beams in Figure 3.3.

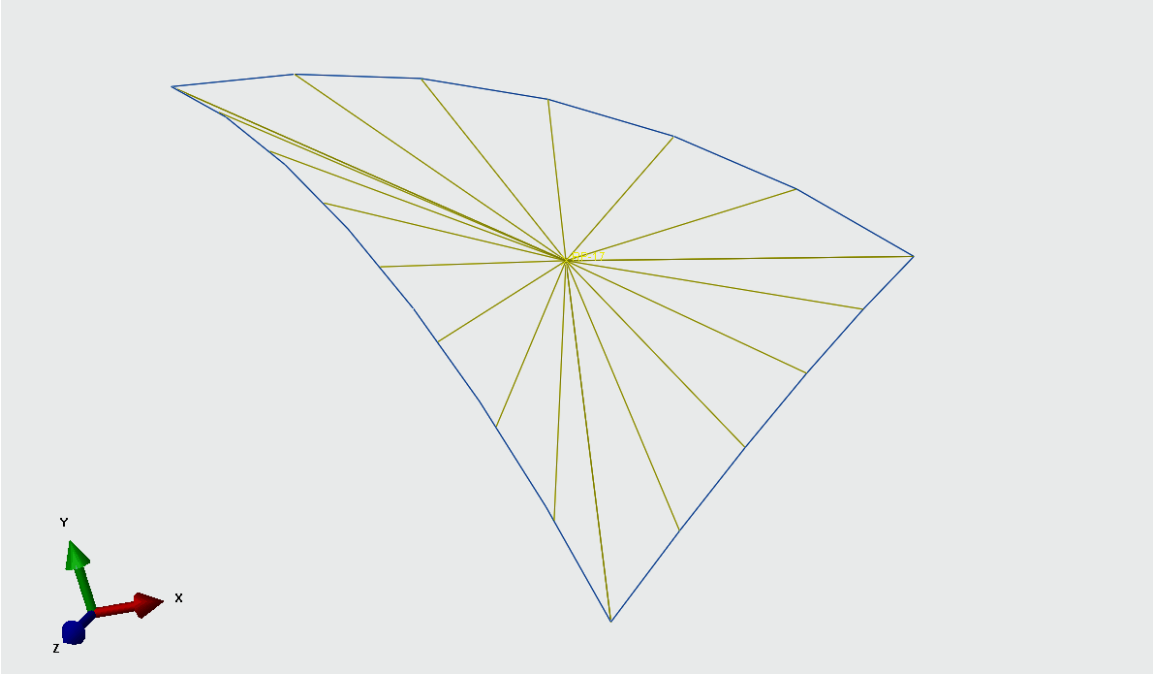

Figure 3.3. Reference point tied to surrounding beams

Concentrated loads equal to 616.056 Newtons directed towards the center of the structure are then applied to each of the 48 individual reference points, creating a system of 48 loads. The magnitude of the individual concentrated loads is determined by multiplying sea-level pressure by the surface area of the reference point's respective curved triangular sections. Figure 3.4 shows a reference point at the center of gravity of one of the curved, spherical triangles (highlighted in red).

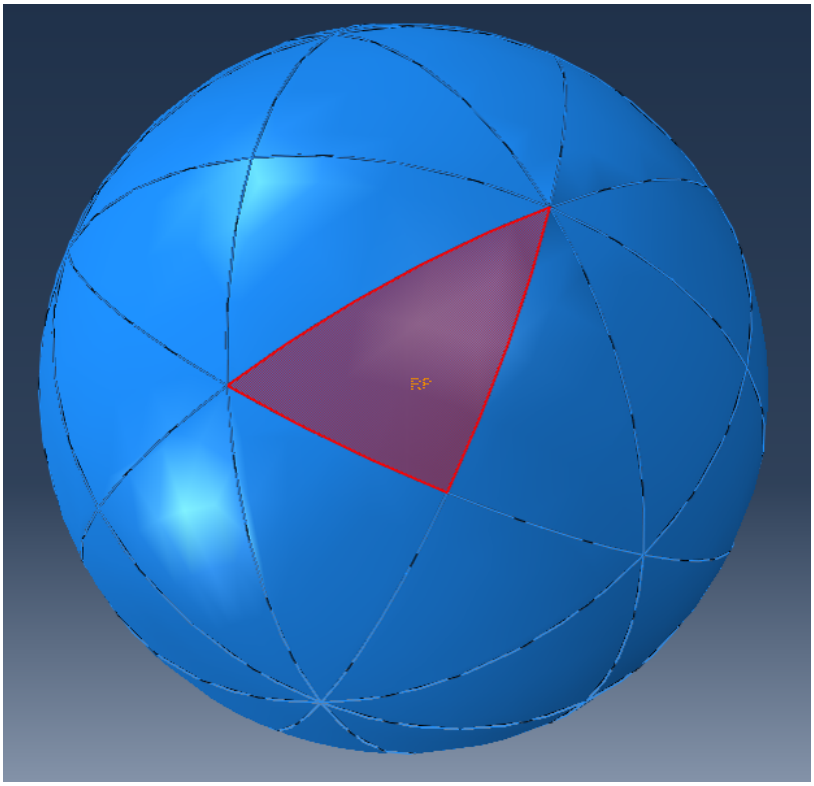

Figure 3.4. Reference point placed at the center of gravity of one of the curved, spherical triangles (highlighted in red)

Applying concentrated loads of this magnitude, which are then distributed evenly across the structure of the frame, simulates a uniform pressure, equal to sea-level pressure, directed towards the center of the structure. An image of the frame structure with the concentrated loads applied to the reference points can be seen in Figure 3.5.

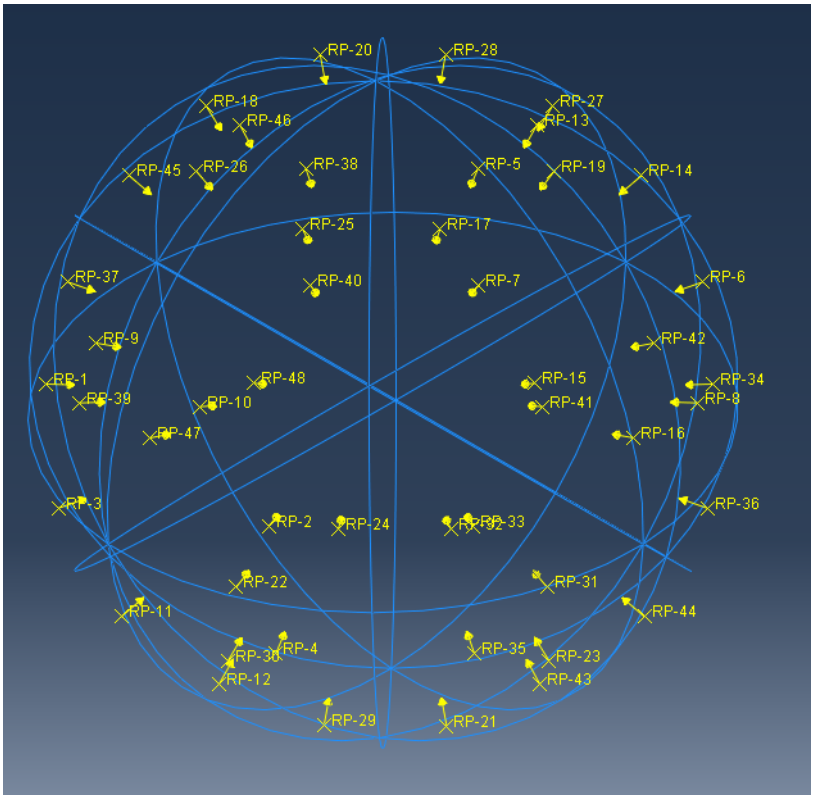

Figure 3.5. Concentrated loads applied to each individual reference point

The three boundary conditions compared in this study (Figures 3.6-3.8) were the same boundary conditions compared for the icosahedron by Adorno-Rodriguez. Boundary condition 1 has the structure completely constrained at the bottom vertex (U1=U2=U3=UR1=UR2=UR3=0) and free at the top vertex. Boundary condition 2 has the structure completely constrained at the bottom vertex (U1=U2=U3=UR1=UR2=UR3=0) and laterally constrained at the top vertex (U1=U3=0). Boundary condition 3 has both vertices (top and bottom) laterally constrained (U1=U3=0). Boundary condition 3 is the only boundary condition which allows rigid body motion of the structure in the y-direction (2-direction). In order to be thorough, boundary conditions representative of each type of constraint available within Abaqus were chosen: longitudinal (U2), lateral (U1 and U3), complete (U1, U2, U3, UR1, UR2, and UR3) as well as combinations of each.

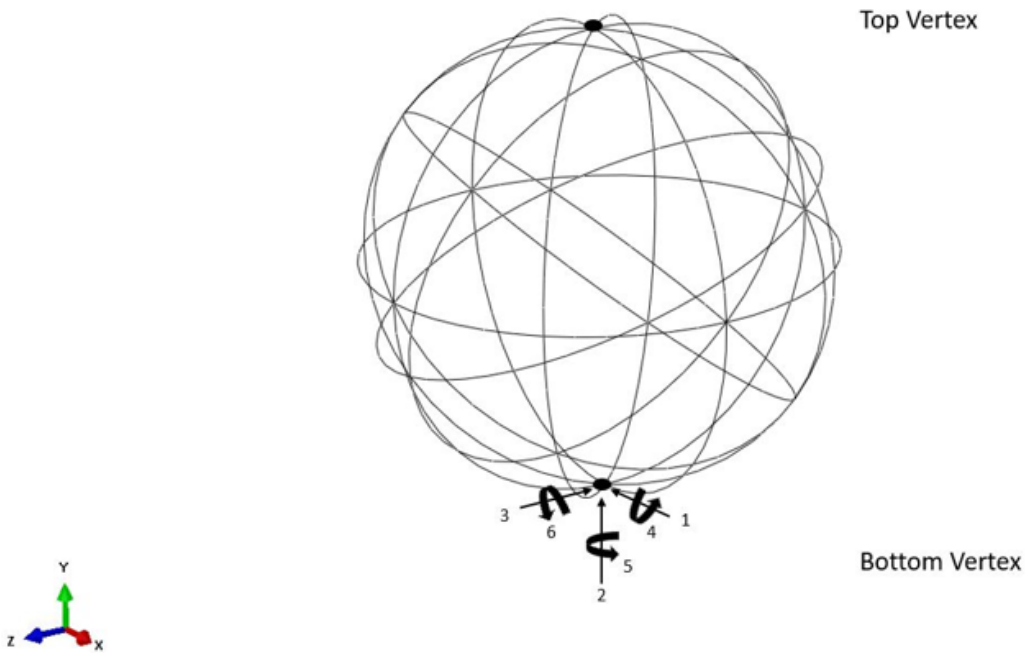

Figure 3.6. Boundary condition 1

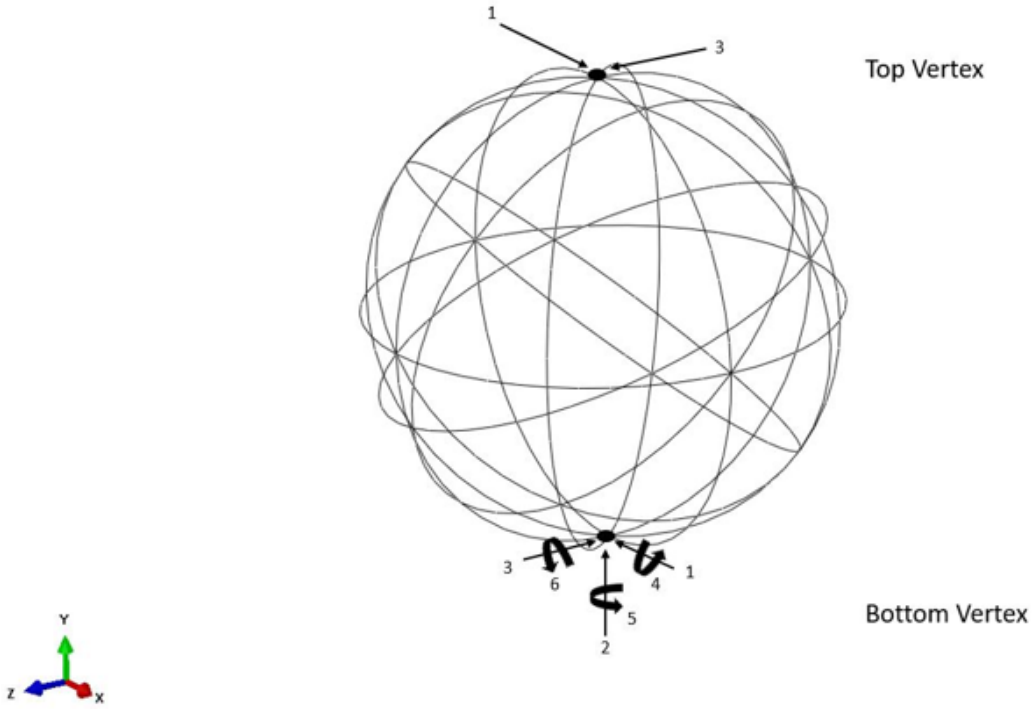

Figure 3.7. Boundary condition 2

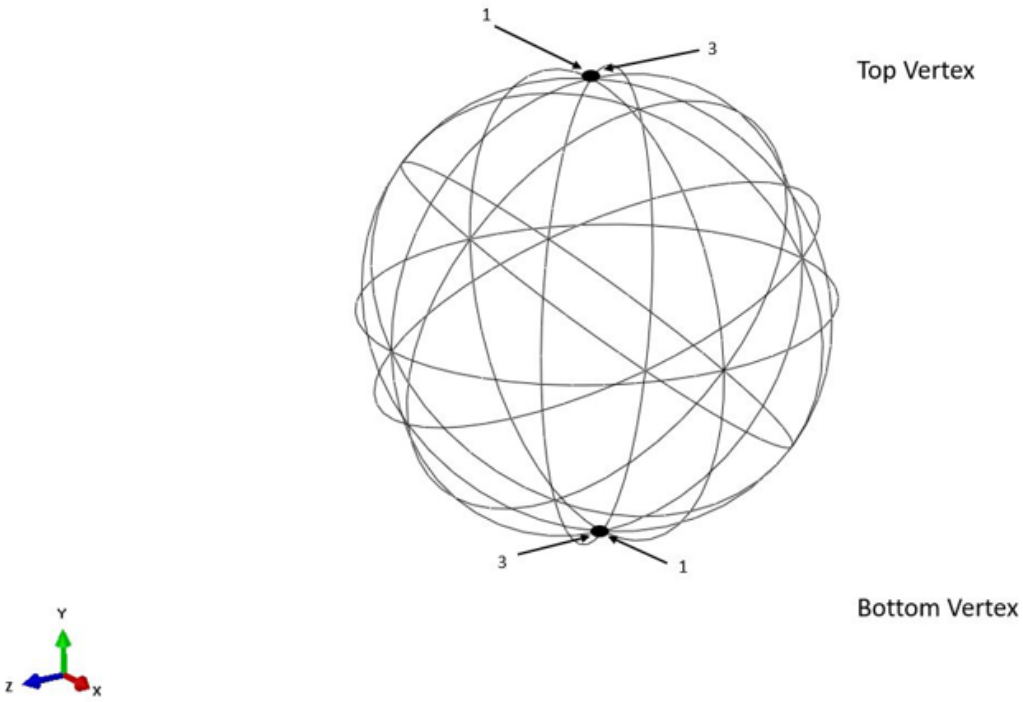

Figure 3.8. Boundary condition 3

Additionally, a model with no boundary conditions (Figure 3.9) was tested for academic purposes. Results for an unconstrained model would later be used to judge the degree of symmetry for each of the three boundary conditions being tested.

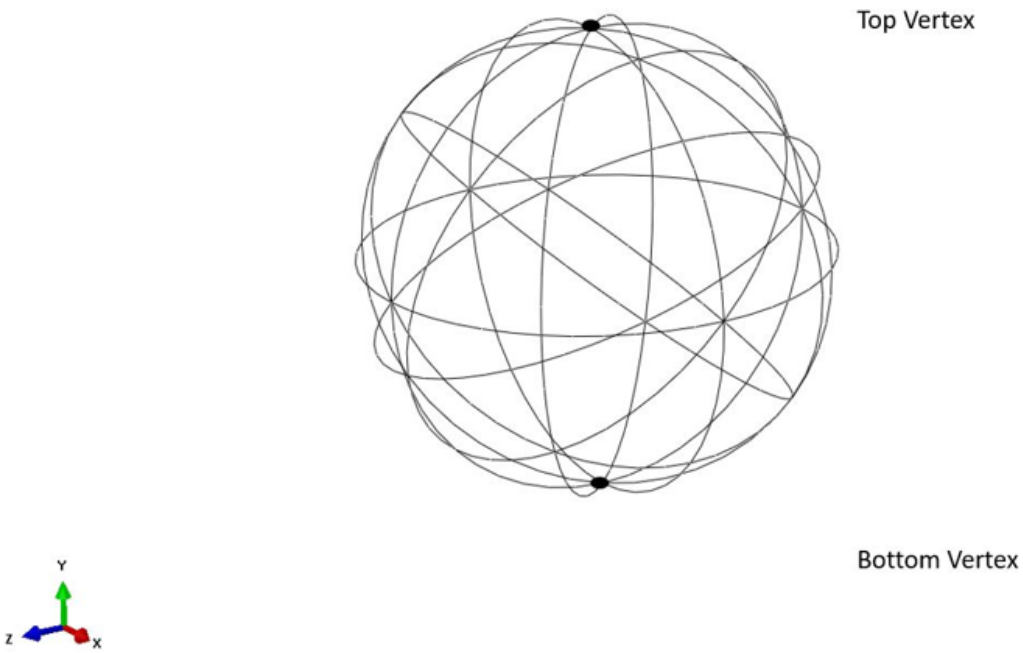

Figure 3.9. Unconstrained model

Because the goal of this study is to compare the effects of the different boundary conditions on the symmetry of the structure's response, it is important to be consistent with part dimensions as well as material properties. The boundary condition study was carried out on model with a structural diameter of 0.3048 meters. The pipe dimensions for the frame structure were based on the minimum manufacturable dimensions for carbon nanotube composite (CNT) (8e-03 meter radius and 2e-04 meter thickness). The material properties for CNT were used for the analysis in Abaqus.

A Newton-Raphson nonlinear, static step with an initial step size of 1e-03 was used; the maximum number of increments was specified to be 1e+08. Automatic adaptive stabilization was used when running these models. Default values for the dissipated energy fraction (0.0002) and the maximum ratio of stabilization to strain energy (0.05) were used for this analysis.

All four models were run using the exact same conditions with exception of the differing boundary conditions. Contour plots of the frame's displacement were com-

pared as well as the displacement along the path shown in Figure 3.10. This path was specifically chosen because it follows a ring directly affected by the different boundary conditions. Because of this, any lack of symmetry within the structure's response will be highlighted. The entirety of the boundary condition study was conducted within CAE. Symmetry is important in this study because it leads to the most even distribution of stress and displacement. An even distribution of stress and displacement leads to lower maximum values (magnitude) for stress and displacement.

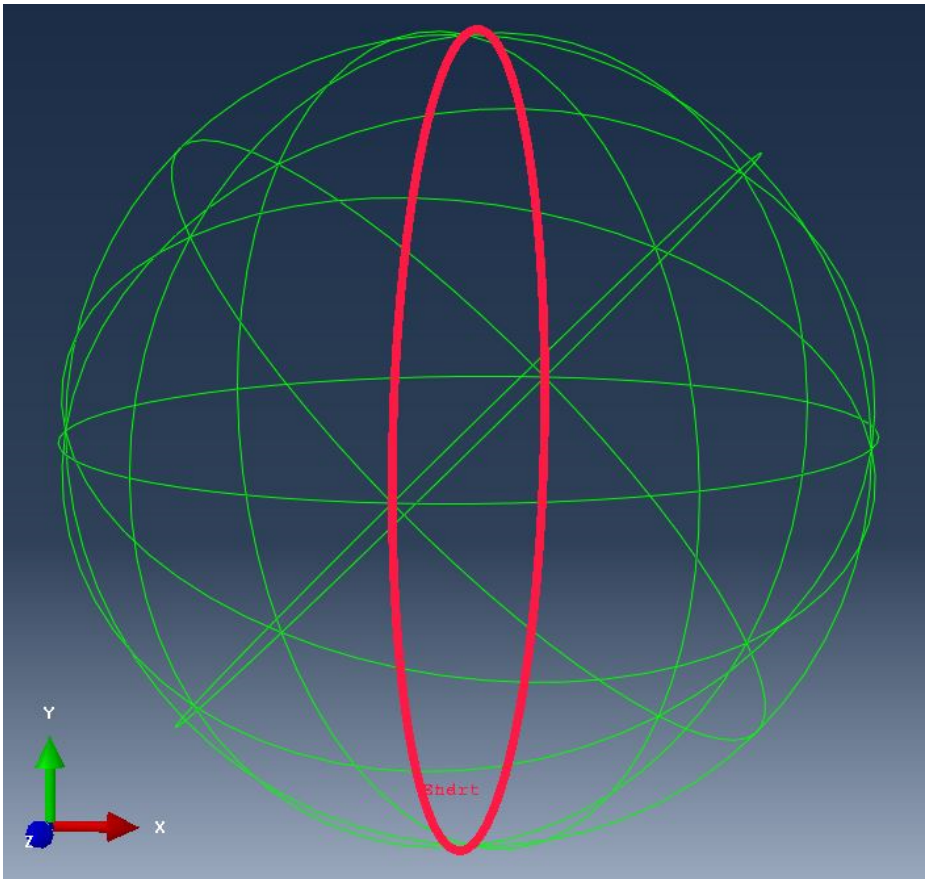

Figure 3.10. Path along ring where the displacements were compared across all four models

The path shown in Figure 3.10 is composed of connections made up of 2 and 4 rings. Examples of 2 ring and 4 ring connections along the path can be seen in Figures 3.11 and 3.12 respectively.

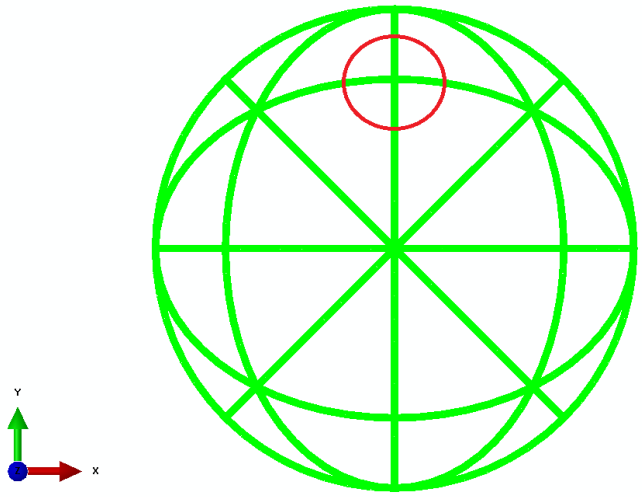

Figure 3.11. 2 ring connection

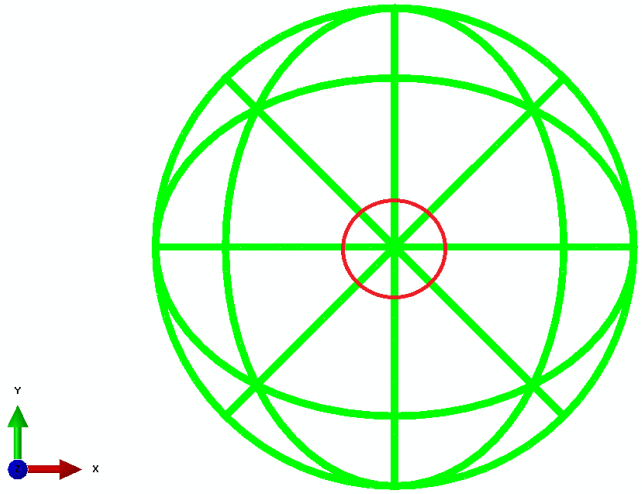

Figure 3.12. 4 ring connection

Additionally, a location near the bottom vertex within the frame (Figure 3.13) was tracked for each of the four models. This was done by tabulating the magnitude of the deformation at that location for each step of the simulation. This portion of the boundary condition study will capture any nonlinear behavior within the frame if it exists.

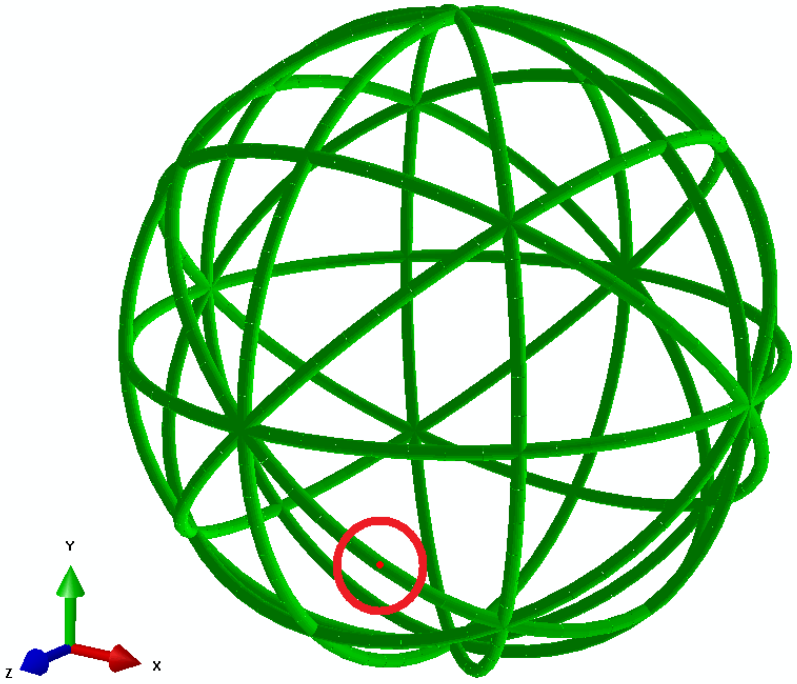

Figure 3.13. Location of the tracked point on the frame

3.3 0.8001 Meter Diameter Model

Because the structure's weight-to-buoyancy (W/B) ratio decreases as the diameter of the structure increases, the minimum W/B ratio is limited by the structure's maximum diameter. Ultimately, the celestial icosahedron VLTAV could one day be used for intelligence, surveillance, and reconnaissance (ISR) in cramped, urban environments. In order for the VLTAV to be most useful, it is necessary that it is able to fit through doorways. The Americans with Disabilities Act (ADA) Accessibility Guideline for Buildings and Facilities requires a minimum opening of 32 inches (0.8128 meters) for wheelchair access [28]. For academic purposes, the maximum allowable diameter for the celestial icosahedron structure will be held constant at 0.8001 meters (31.5 inches). Thus, the maximum W/B ratio for this study will be achieved with a structural diameter of 0.8001 meters.

Analysis of a 0.8001 meter diameter celestial icosahedron achieving minimum W/B

ratio was carried out by modifying Cranston's original model using the Matlab script found in Appendix B. The structural diameter was held constant at 0.8001 meters and the frame's pipe radius and thickness was held constant at 8.00e-03 and 2.00e-04 meters respectively. The pipe dimensions correspond to the minimum manufacturable dimensions of CNT. The frame and the attached skin were modeled using the material properties for CNT and Graphene respectively (Table 2.1).

The skin thickness acted as the independent variable for this optimization process; the skin thickness was incrementally reduced (starting at 1.00e-05 meters) using the previously mentioned Matlab code until the structure's overall factor of safety (FS) reached a value of 1.50 and the W/B ratio was minimized. Once again the criteria for a viable model are: $W/B<1$ and $FS\geq1.50$.

All of the models for the 0.8001 meter diameter study were loaded with a uniform pressure directed towards the center of the structure, equal to sea-level static pressure (101,325 Pascals). The top and bottom vertex were constrained in the 1 and 3 directions (U1=U3=0). This boundary condition corresponds to boundary condition 3 from the boundary condition study. Figure 3.14 shows the model in CAE with the applied loading condition described above.

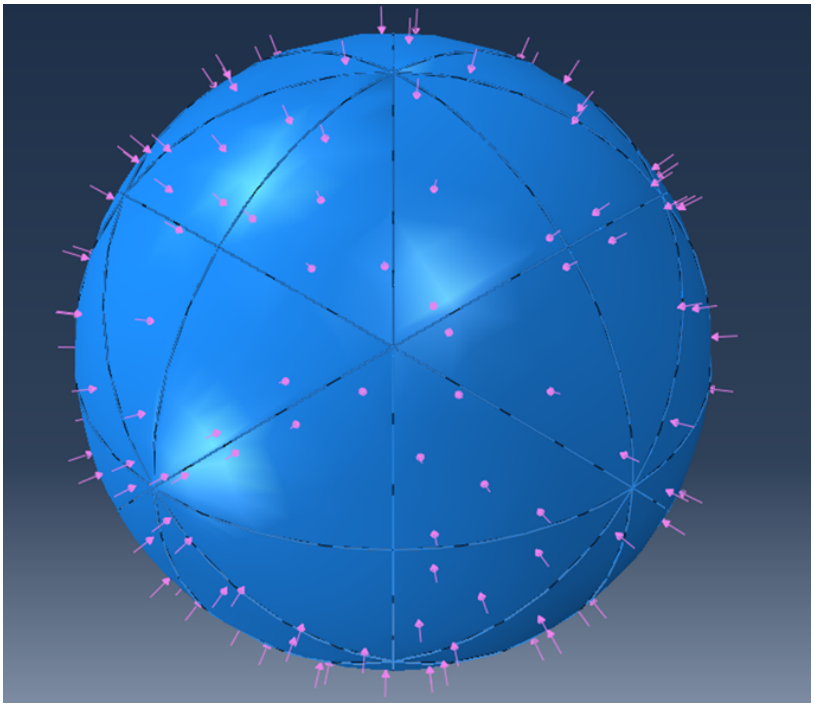

Figure 3.14. CAE image of the celestial icosahedron model with the loading condition applied

All of the models were analyzed using Abaqus through the command line. This, along with all of the dimensions modifications, was done using the Matlab code found in Appendix B. A detailed explanation of how the Matlab code is used can be found in Appendix A. The same Newton-Raphson nonlinear, static step from the boundary condition study was used. The same automatic adaptive stabilization settings from the boundary condition study were used as well.

In order to capture the skin's effect on the linearity of the structure's response, the same point on the frame from Figure 3.13 was tracked for the last iteration of the 0.8001 meter diameter model. The magnitude of the deformation and the corresponding percentage of sea-level pressure applied at that step were tabulated. Due to the large number of increments needed for the convergence of this model, the magnitude and corresponding pressure were tabulated for every 500 increments. Additionally, a point on the skin (Figure 3.15), was tracked with its deformation

values tabulated following the same steps listed above. By tracking points in the frame and the skin separately, sources of nonlinearity within the structure (if they exist) can be pointed out.

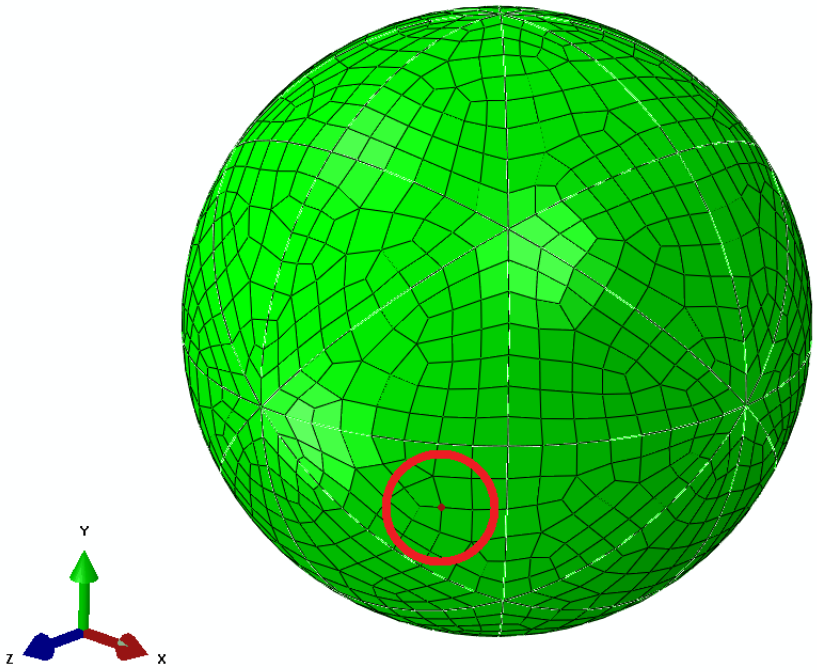

Figure 3.15. Location of the tracked point on the skin

3.4 1.2192 Meter Diameter Model

A 1.2192 meter diameter model was created and analyzed in order to easily compare the performance of the celestial icosahedron to that of the hexakis icosahedron. To date the smallest feasible design for the hexakis icosahedron is 1.2192 meters in diameter. The criteria for a feasible design includes a W/B<1 and a FS≥1.15. A FS of 1.15 was chosen as it corresponds to the FS of Schwemmer's feasible 1.2192 meter diameter design [7],[8].

The Matlab code found in Appendix B was used to increase the diameter of the model to 1.2192 meters. The code was also used to vary the skin thickness as well

as the beam dimensions as necessary. The initial skin thickness corresponded to the minimum skin thickness achieved for the 0.8001 meter diameter model (7.85e-07 meters). The initial beam dimensions (radius and thickness) were based on the minimum manufacturable dimensions for beams constructed of CNT, 8.00e-03 and 2.00-04 meters respectively. The beam dimensions were increased as necessary, while holding the c-ratio constant at 0.025.

The same material properties (CNT frame with a Graphene skin), loading conditions (uniform external pressure equal to sea-level pressure), and boundary conditions (top and bottom vertices constrained in the lateral directions) from the 0.8001 meter diameter model were used. Additionally, the same Newton-Raphson nonlinear, static step, as well as the automatic adaptive stabilization settings from previous study was used. The code was then used to run the .inp file, analyzing the models using Abaqus through the command line.

The procedure carried out on the 0.8001 meter diameter model to check for linearity was conducted on the final iteration of the 1.2192 meter diameter model as well. Locations on the frame (Figure 3.13) and the skin (Figure 3.15) were tracked, and the magnitude of the deformation was tabulated for every 500 increments. These values were plotted against the percentage of the total applied pressure at each corresponding increment. This portion of the study was carried out in order to determine what effect the changing of the structural diameter of the model has on the linearity of the system.

3.5 Minimum Diameter Model

The goal of this study was to determine the smallest possible structural diameter for a feasible design (FS$\geq$1.50). Any W/B ratio resulting in positive buoyancy (W/B$<$1) satisfies the design requirements.

For the minimum diameter study, the same material properties (CNT frame with a Graphene skin), loading conditions (uniform external pressure equal to sea-level pressure), and boundary conditions (top and bottom vertices constrained in the lateral directions) from the previous two studies were used. Additionally, the same Newton-Raphson nonlinear, static step, as well as the automatic adaptive stabilization settings from the previous two studies were utilized in the minimum diameter study. The minimum diameter study was conducted after the results of the 0.8001 and 1.2921 meter studies had been obtained. These results were used in choosing the initial structural dimensions for the minimum diameter study. An initial structural diameter of 0.8000 meters was modeled with a skin thickness of 7.85e-07 meters. Additionally, the minimum manufacturable pipe dimensions were chosen to characterize the frame's structure.

The Matlab code (Appendix B) was used to modify (reduce) the structural diameter as well as the skin thickness incrementally until the both the W/B ratio and FS requirements were met. The same code was then used to run the .inp file, analyzing the models using Abaqus through the command line. Once again, detailed instructions on the use of the Matlab code described above can be found in Appendix A.

The same linearity study conducted on the 0.8001 and 1.2192 meter diameter models was carried out for the final iteration of the minimum diameter model. The locations depicted in Figures 3.13 and 3.15 were tracked and the magnitude of their deformations were tabulated for every 500 increments. These values were plotted against the percentage of the total applied pressure corresponding to their respective increments. This study was conducted in order to track the reduction in the structural diameter's effect on the linearity of the system.

3.6 Summary

The purpose of this chapter is to describe the research methodology carried out in this thesis. This research was conducted using a FEM of a celestial icosahedron shaped VLTAV which was then modified as needed using the Matlab script found in Appendix B. The Finite Element solver Abaqus was used to analyze this structure in the boundary condition, 0.8001 and 1.2921 meter diameter, and minimum diameter studies.

IV. Results and Discussion

4.1 Chapter Overview

This chapter details the results of the feasibility study of the celestial icosahedron vacuum lighter than air vehicle (VLTAV). The study includes the boundary condition study as well as models with three different structural diameters: 0.8001 meters, 1.2192 meters, and a minimum diameter.

4.2 Boundary Condition Study

Figures 4.1 and 4.2 show the contour plots of the deformation (magnitude) for boundary conditions 1 and 2. The deformations seen here are magnified by a factor of 1.50e+03 in order emphasize the results. This is done by changing the deformation scale factor which can be found within the options menu in the Complete Abaqus Environment (CAE). Qualitatively the contour plots for these two boundary conditions look identical, suggesting that the top constraint of boundary condition 2 (U1=U3=0) has no effect on the overall symmetry of the structure's response. For both cases, it is clear that completely constraining the bottom vertex (U1=U2=U3=UR1=UR2=UR3=0) results in an uneven distribution of deformation, with larger deformations occurring in the top half of the structure.

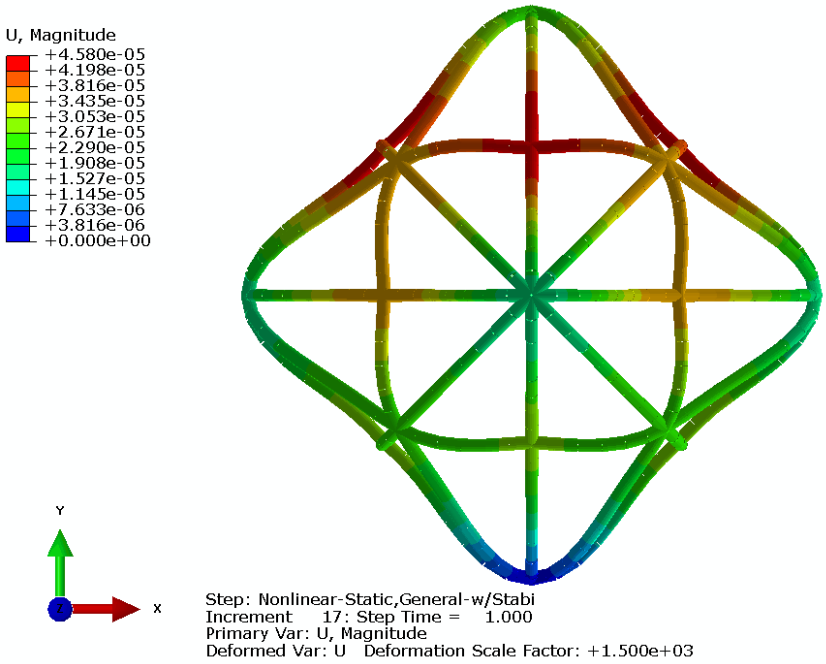

Figure 4.1. BC 1: Contour plot of deformation (magnitude)

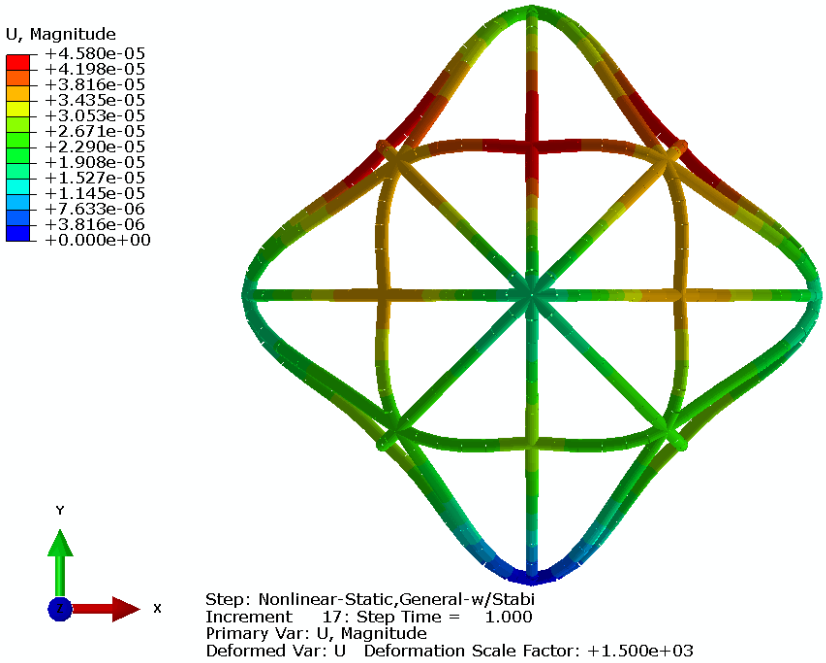

Figure 4.2. BC 2: Contour plot of deformation (magnitude)

Similarly, Figures 4.3 and 4.4 show the contour plots of the deformation (magnitude) for boundary condition 3 and the unconstrained case. Once again the deformations have been magnified by a factor of 1.50e+03. These two contour plots, are completely symmetric in terms of deformation. Qualitatively speaking, the magnitudes of the deformations appear to be equal at connections where an equal number of rings are coming together; for example, all two ring connections appear to experience an equal magnitude of deformation. The contour plots for boundary condition 3 and the unconstrained case confirm that constraining a vertex in the lateral directions (U1 and U3) has no effect on the structure's symmetry when a uniform load directed towards the center of the structure is applied.

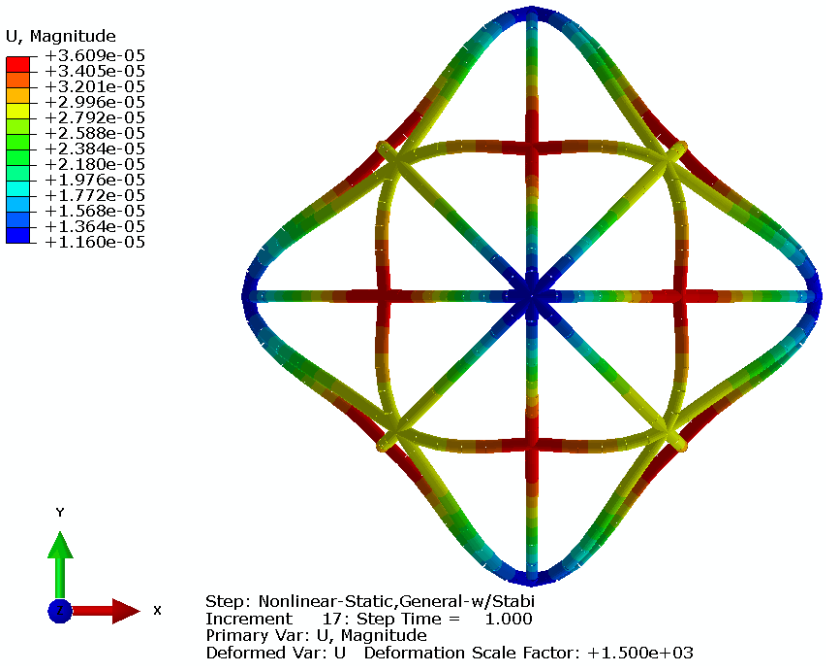

Figure 4.3. BC 3: Contour plot of deformation (magnitude)

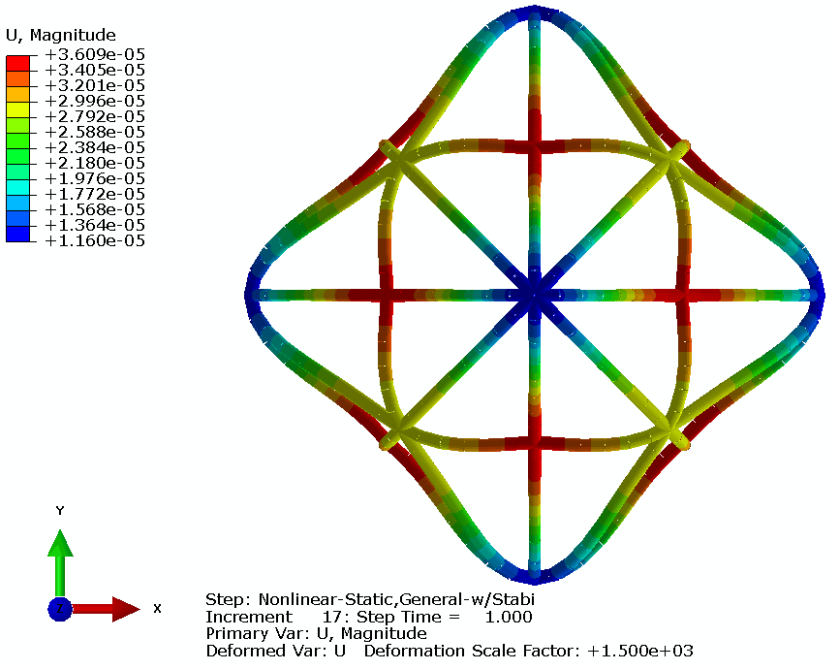

Figure 4.4. Unconstrained: Contour plot of deformation (magnitude)

Figures 4.5-4.7 were produced to quantitatively confirm the qualitative results derived from the contour plots above. Figure 4.5 shows all four cases' deformations along the path described in Figure 3.10. It is clear that boundary conditions 1 and 2 result in an unsymmetric response while boundary condition 3 and the unconstrained case result in symmetry. The unsymmetric distribution of deformation leads to larger maximum values of deformation for the first two boundary conditions. This can be seen in the two peaks located at 90 and 180 degrees. The two peaks for boundary conditions 1 and 2 are roughly 1.00e-05 meters higher than those for boundary condition 3 and the unconstrained case.

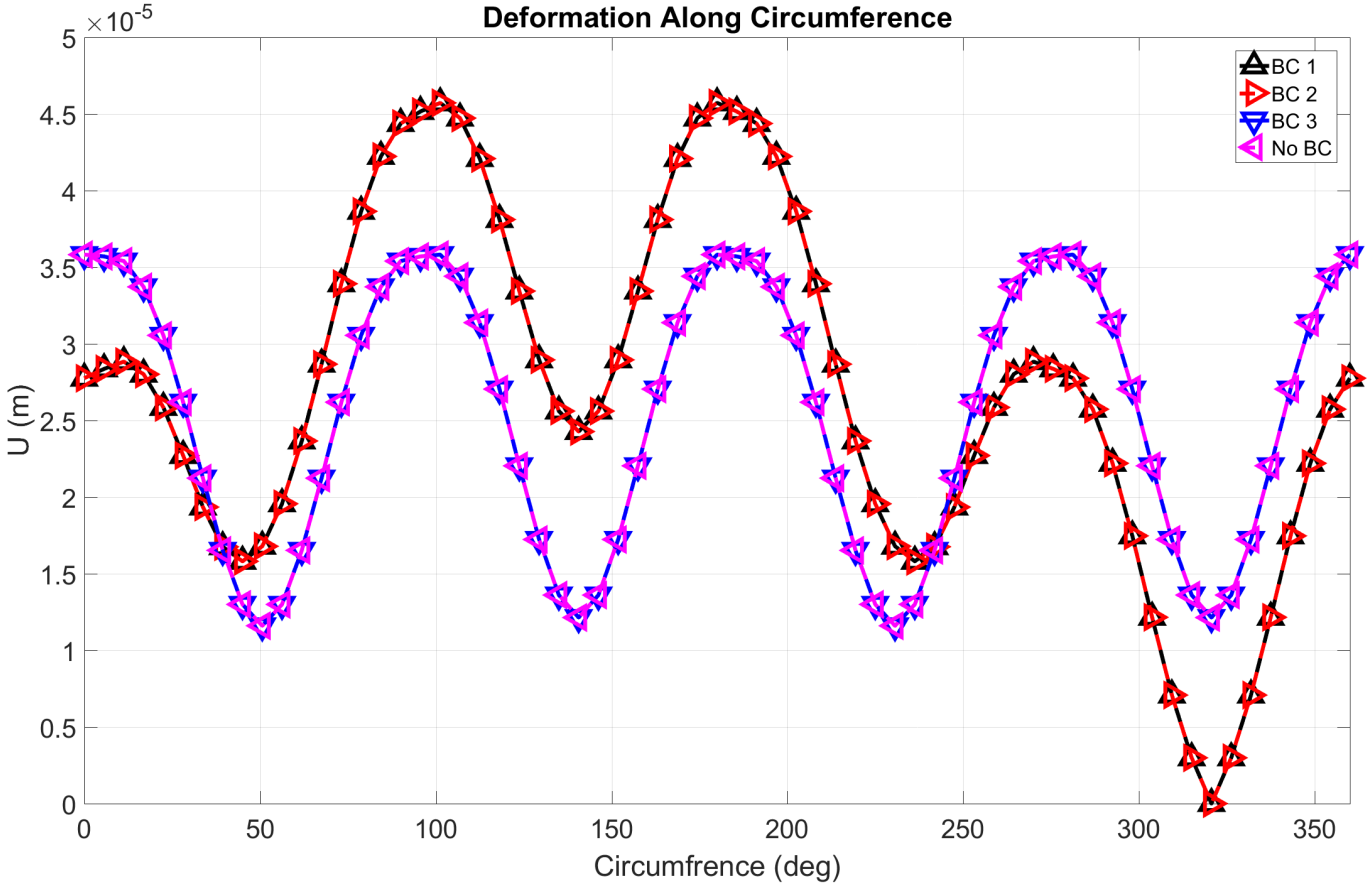

Figure 4.5. Plot of deformation (meters) vs. circumference (degrees) for BC 1, BC 2, BC 3, and unconstrained cases

Figure 4.6 shows the results of boundary conditions 1 and 2 only. This highlights the lack of symmetry resulting from the complete constraint of the bottom vertex. It is clear that the largest deformations occur on the top half of the structure (away from the complete constraint) where there is a connection of 2 rings. The second largest deformations also occur at the 2 ring connections, but on the bottom half of the structure (closest to the complete constraint). As expected, the deformations at the sturdier, 4 ring connections are smaller, with the magnitudes decreasing as the locations get closer to the constrained bottom vertex. Because of the complete constraint applied to it, the 4 ring connection at the bottom vertex has no deformation.

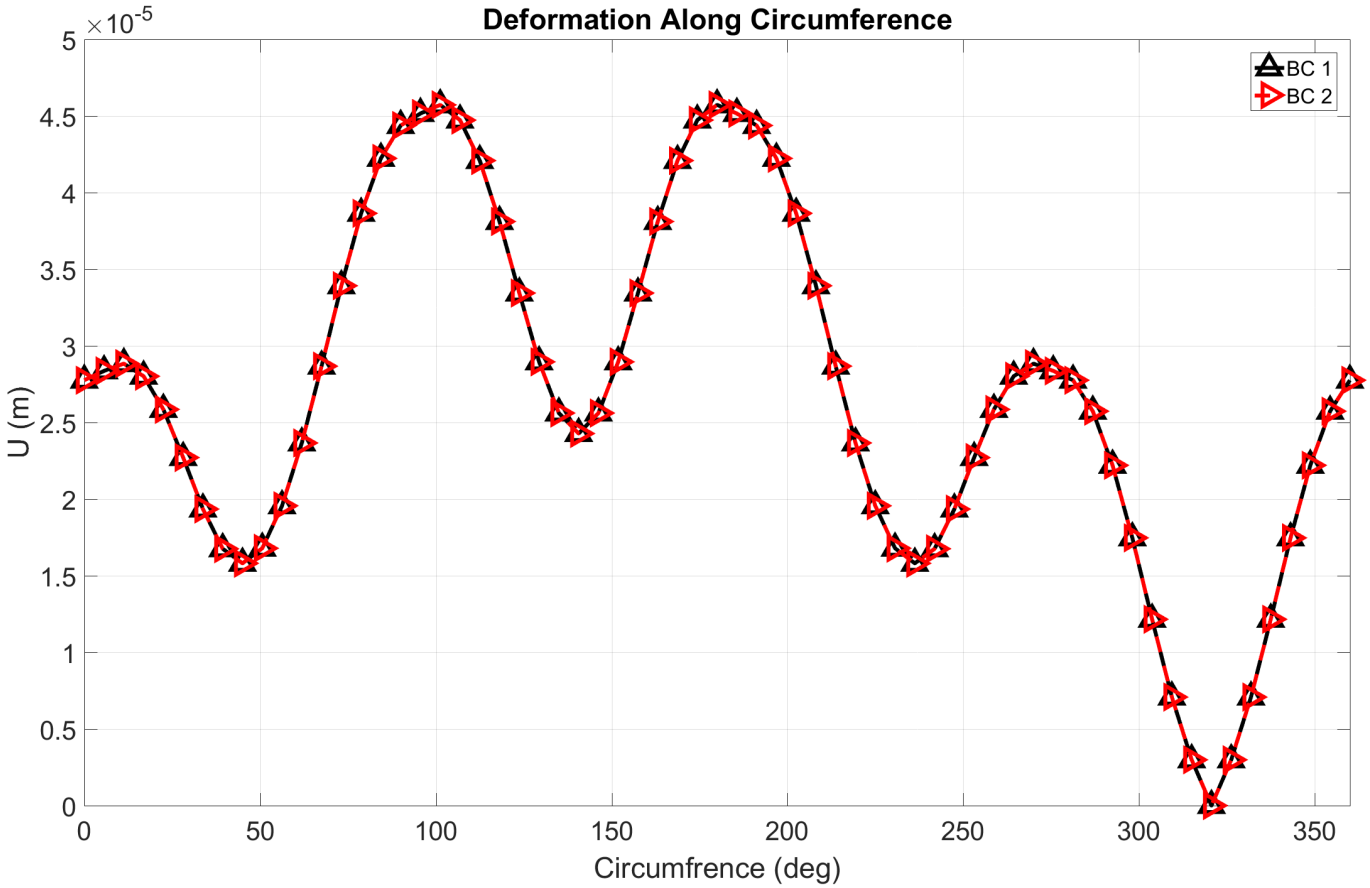

Figure 4.6. Plot of deformation (meters) vs. circumference (degrees) for BC 1 and BC 2 cases

Figure 4.7 shows the results of boundary condition 3 and the unconstrained case. The symmetry of both cases is apparent in the co-sinusoidal plot with a period of 90 degrees. The peaks in the plot correspond to the 2 ring connections of the structure, and the valleys correspond to the more rigid 4 ring connections. Each peak and valley has a 45 degree spacing in between, corresponding to the 45 degree spacing of the rings.

Because boundary condition 3 and the unconstrained case result in identical, symmetric plots, these two cases can be used interchangeably in future studies. Because Abaqus runs into convergence issues when models are run without boundary condi-

tions though, boundary condition 3 was used for the remainder of this research. The results of the boundary condition study are tabulated in Table 4.1.

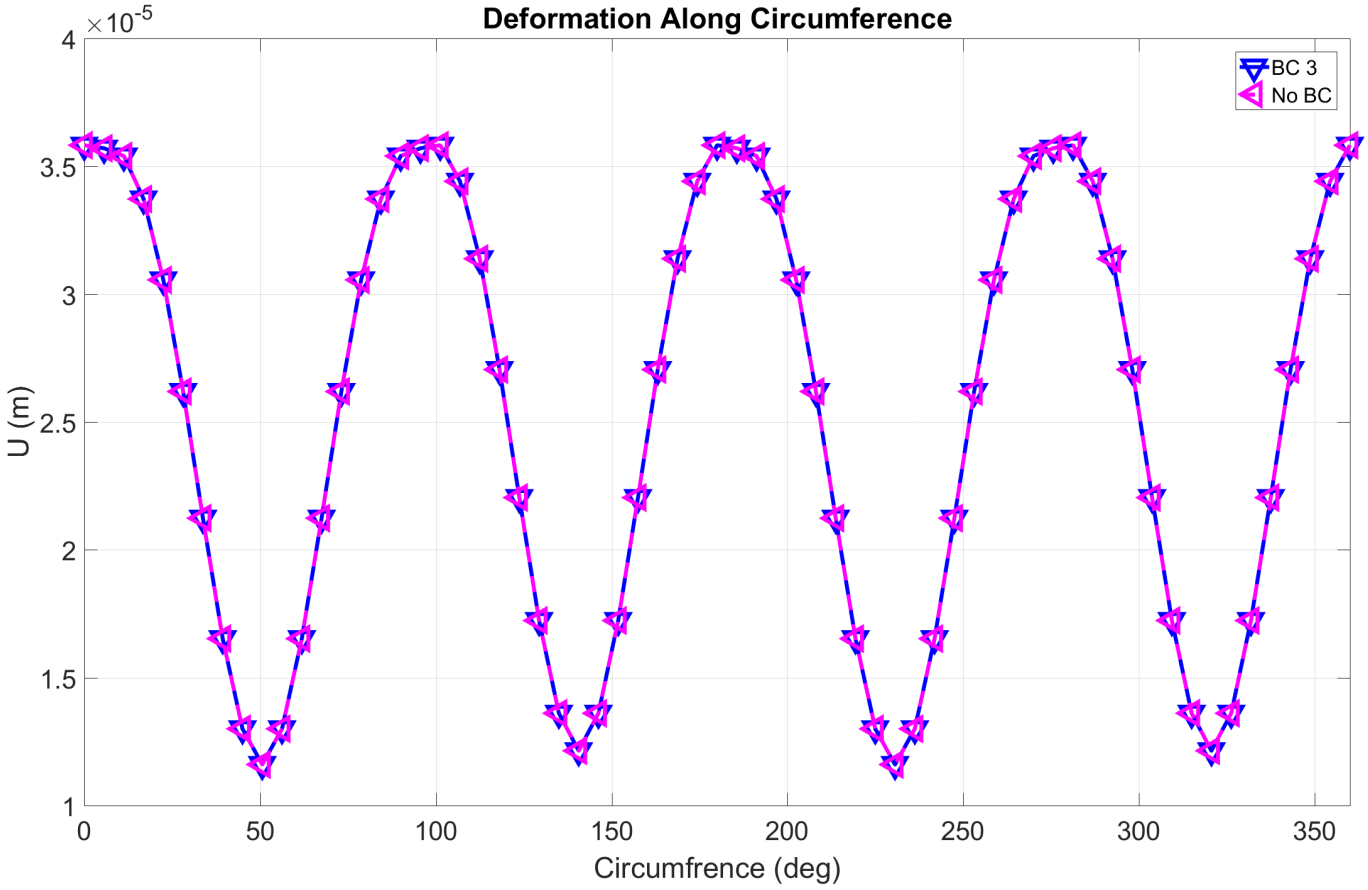

Figure 4.7. Plot of deformation (meters) vs. circumference (degrees) for BC 3 and unconstrained cases

Table 4.1. Magnitude of deformation (meters) at connections (boundary condition study)

		Case			
Connection (# of Rings)	**Location within Structure**	**BC 1**	**BC 2**	**BC 3**	**Unconstrained**
2	Bottom	2.84e-05	2.84e-05	3.57e-05	3.57e-05
	Top	4.52e-05	4.52e-05	3.57e-05	3.57e-05
4	Bottom	0	0	1.16e-05	1.16e-05
	Middle	1.68e-05	1.68e-05	1.16e-05	1.16e-05
	Top	2.43e-05	2.43e-05	1.16e-05	1.16e-05

These results for the celestial icosahedron are in line with the results presented by Adorno-Rodriguez for the icosahedron. Adorno-Rodriguez's study showed that constraining the icosahedron's top and bottom vertices in the lateral directions (U1 and U2 in his case) leads to a symmetric response of the structure [23],[24].

Figures 4.8-4.11 show the plots of the deformation at the tracked point against the percentage of sea-level pressure being applied at that time. All four cases result in a linear relationship between the applied pressure and the resulting deformation. The frame alone acts linearly. If any nonlinear response takes place, it is due to the application of the skin.

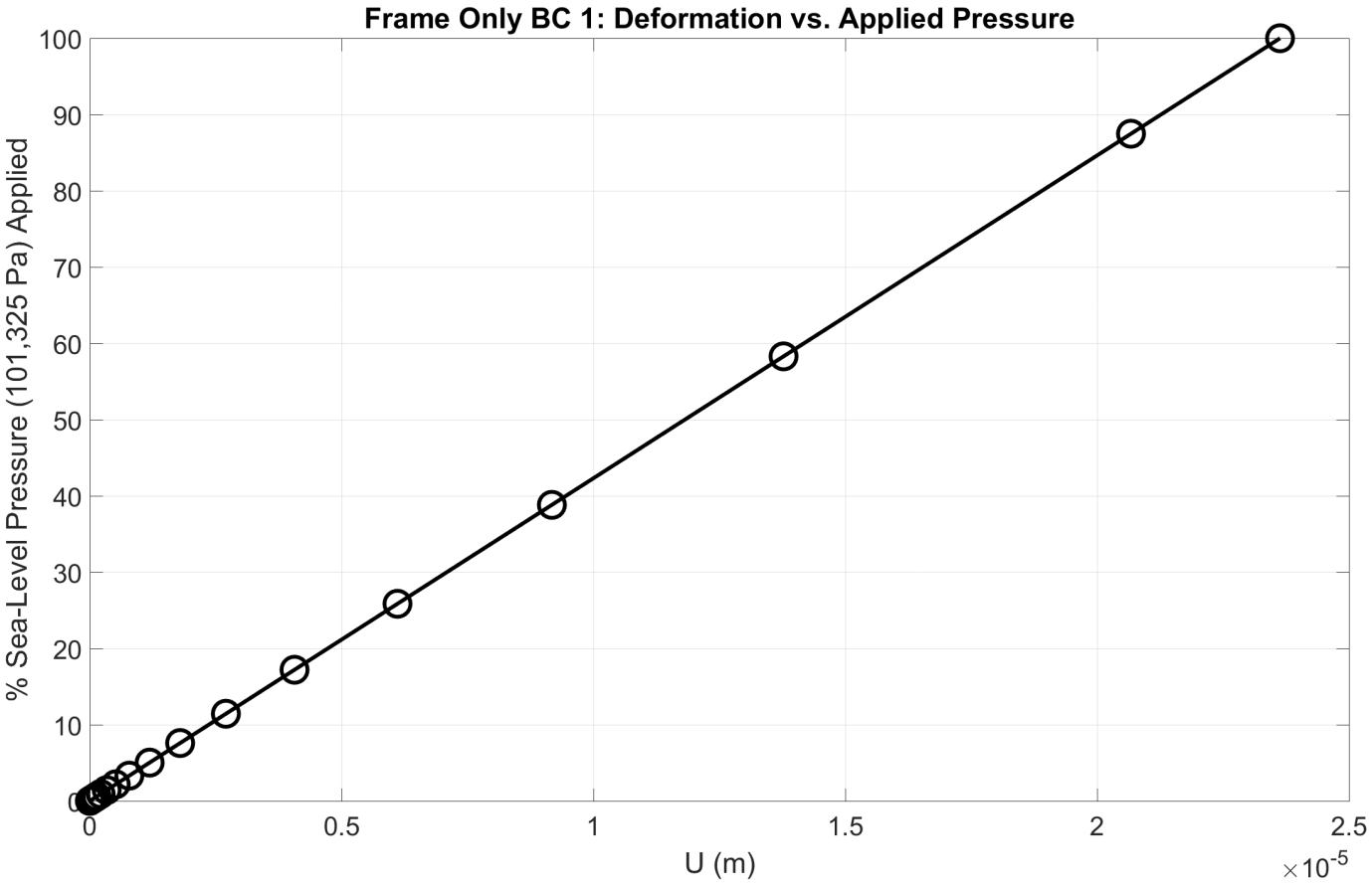

Figure 4.8. Plot of deformation (meters) vs. the percentage of sea-level pressure (101,325 Pa) applied for BC 1

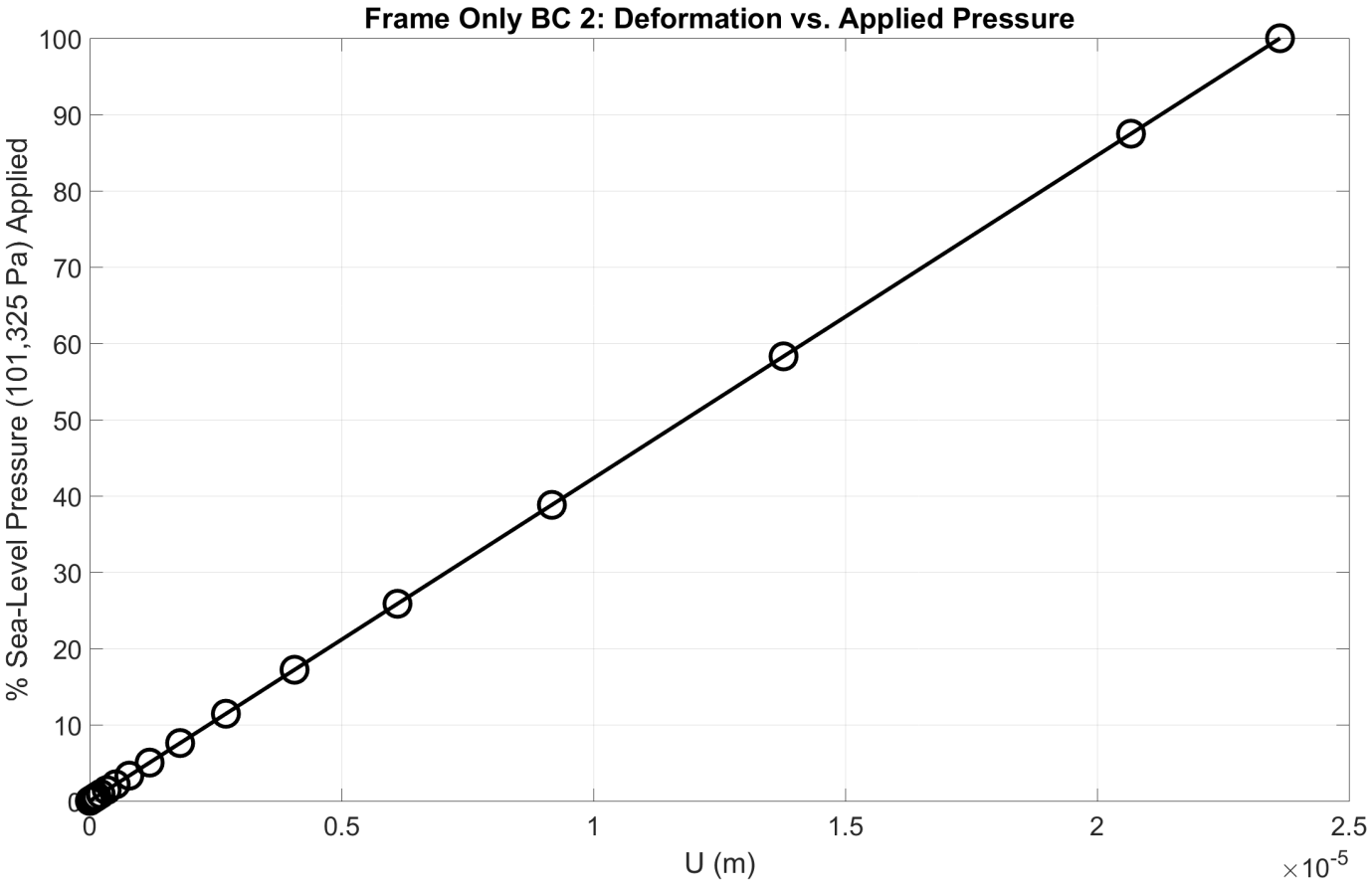

Figure 4.9. Plot of deformation (meters) vs. the percentage of sea-level pressure (101,325 Pa) applied for BC 2

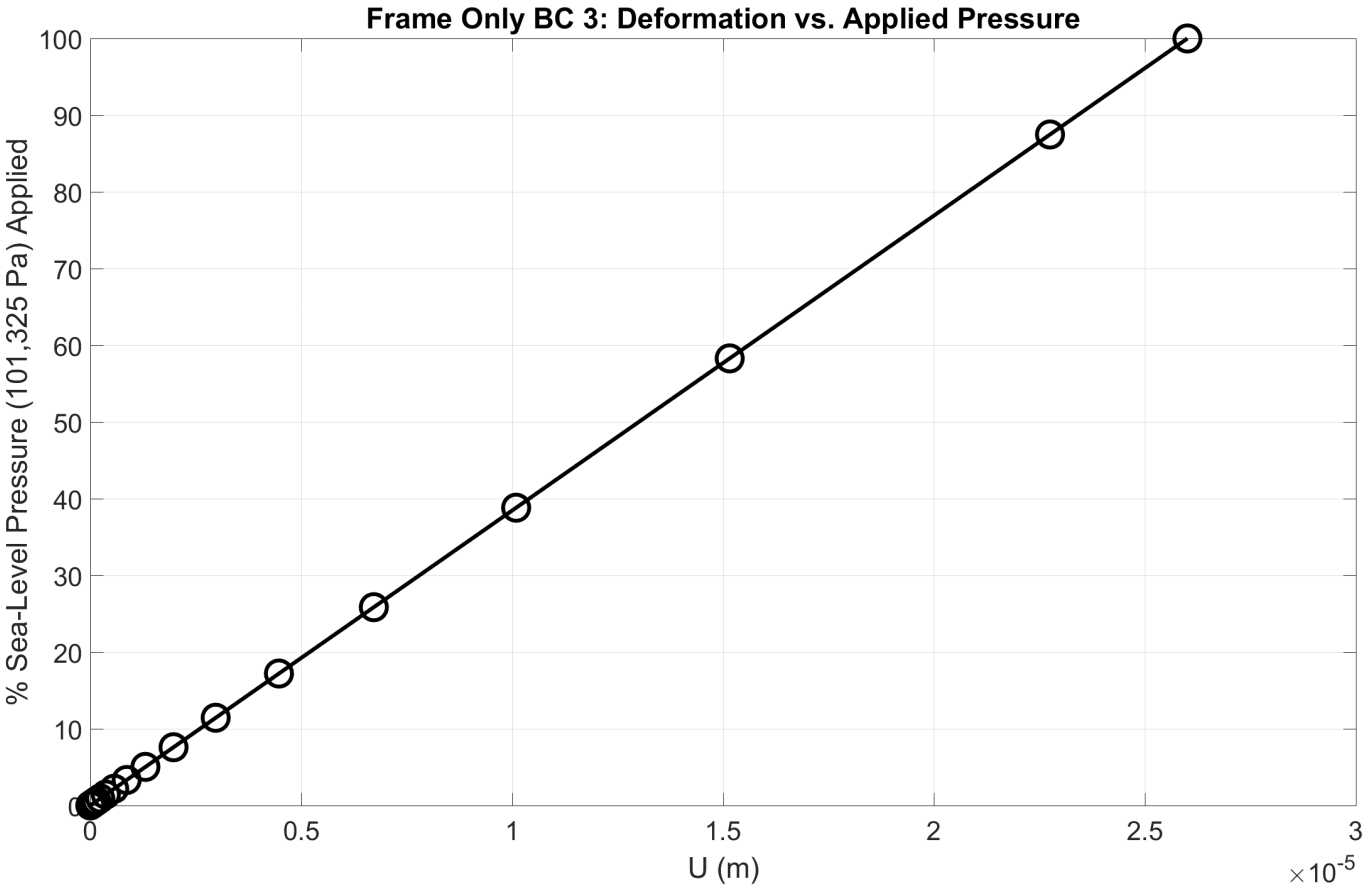

Figure 4.10. Plot of deformation (meters) vs. the percentage of sea-level pressure (101,325 Pa) applied for BC 3

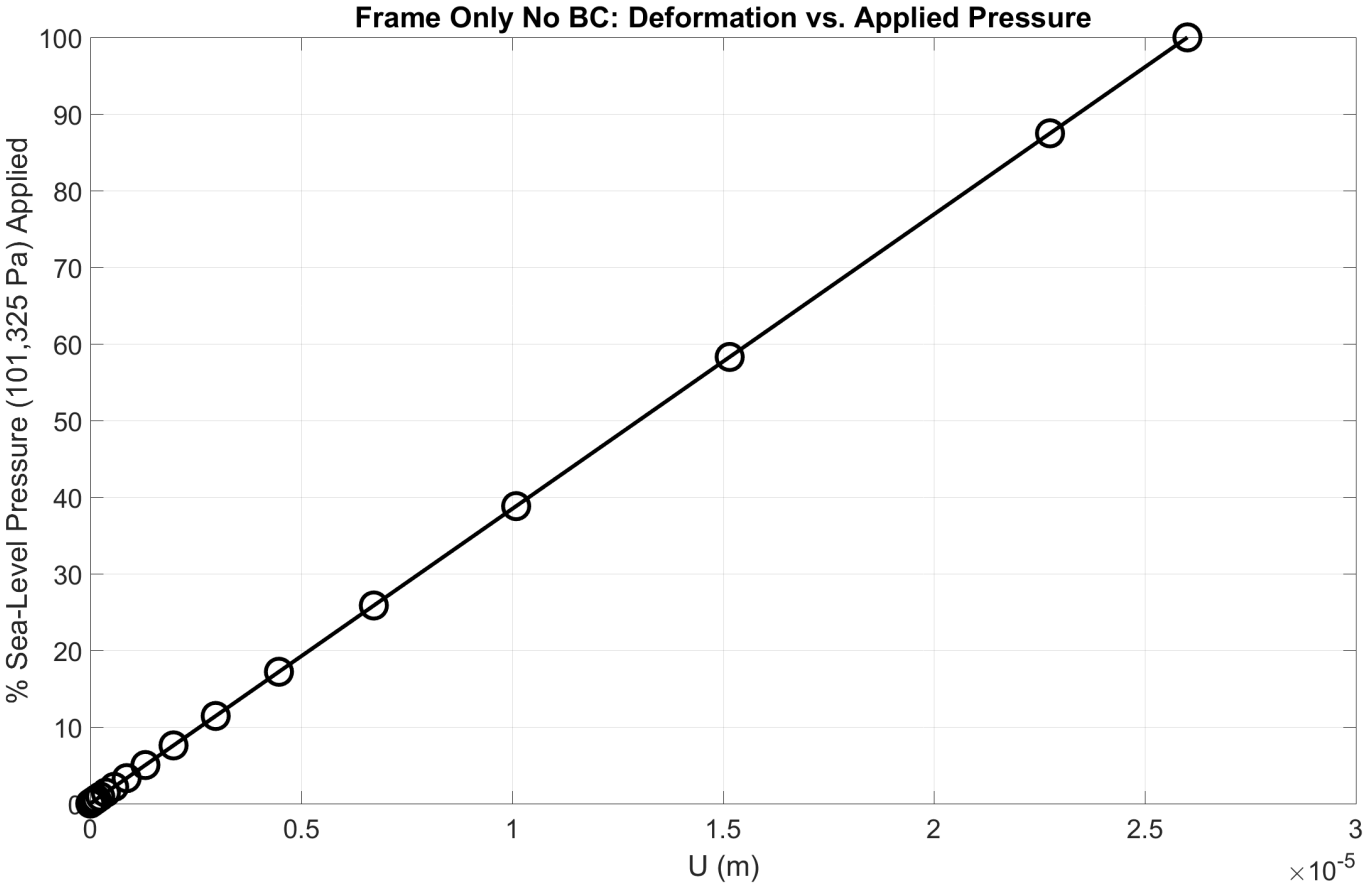

Figure 4.11. Plot of deformation (meters) vs. the percentage of sea-level pressure (101,325 Pa) applied for the unconstrained case

4.3 0.8001 Meter Diameter Model

The minimum weight-to-buoyancy (W/B) ratio achieved for a model with a 0.8001 meter structural diameter is 0.8994. The structure has a skin thickness of 7.85e-07 meters with beam radii and thicknesses equal to 8.00e-03 and 2.00e-04 meters respectively. The structure weighs 283.66 grams, giving the it the ability to carry a payload of up to 31.72 grams. The results for all of the iterations of the 0.8001 meter diameter model are tabulated in Table 4.2.

Table 4.2. 0.8001 meter diameter results

D (m)	r_{beam} (m)	t_{beam} (m)	t_{skin} (m)	FS_{frame}	FS_{skin}	FS_{total}	W/B_{frame}	W/B_{skin}	W/B_{total}
0.8001	8.00e-03	2.00e-04	1.00e-05	1.61	5.04	1.61	0.8879	0.1273	1.0152
0.8001	8.00e-03	2.00e-04	1.00e-06	1.57	1.77	1.57	0.8896	0.0128	0.9023
0.8001	8.00e-03	2.00e-04	9.50e-07	1.57	1.72	1.57	0.8896	0.0121	0.9017
0.8001	8.00e-03	2.00e-04	9.00e-07	1.57	1.67	1.57	0.8895	0.0115	0.9010
0.8001	8.00e-03	2.00e-04	8.50e-07	1.57	1.60	1.57	0.8895	0.0108	0.9003
0.8001	8.00e-03	2.00e-04	8.00e-07	1.57	1.52	1.52	0.8894	0.0102	0.8996
0.8001	8.00e-03	2.00e-04	7.50e-07	1.58	1.45	1.45	0.8894	0.0096	0.8989
0.8001	8.00e-03	2.00e-04	7.75e-07	1.57	1.48	1.48	0.8894	0.0099	0.8993
0.8001	8.00e-03	2.00e-04	7.85e-07	1.57	1.50	1.50	0.8894	0.0100	0.8994

It is worth noting that the factor of safety (FS) fell below 1.50 for a skin thickness equal to 7.50e-07 meters. Because of that, the following iterations incrementally increased the skin thickness until the FS requirement was met. A similar process was carried out for the 1.2192 meter diameter model as well as the minimum diameter model. The plots in Figures 4.12 and 4.13 show the effect of the skin thickness on the design's total FS and W/B ratio respectively. Note that the first iteration (1.00e-05 meter skin thickness) is omitted from these plots for scaling purposes.

With the exception of the results corresponding to the largest and smallest skin thicknesses (1.00e-05 and 7.50e-07 meters respectively), the tabulated results (Table 4.2) show that the frame's FS is unchanged for varying skin thicknesses. Additionally, the tabulated results, as well as the plotted results (Figure 4.12), show that the model's overall FS is not affected by a reduction of skin thickness until the skin thickness is less than 8.50e-07 meters. The model's total FS is not dependent on

skin thickness for skin thicknesses greater than or equal to 8.50e-07 meters because the maximum, limiting Von Mises (VM) stress is contained within the frame. For skin thicknesses between 8.50e-07 and 8.00e-07 meters, the maximum, limiting VM stress in the model is transfered from the frame to the skin, causing the total FS to become dpendent on the skin thickness. Once the total FS becomes dependent upon the skin thickness, a linearly proportional relationship between the skin thickness and the model's total FS develops. A smaller skin thickness results in a lower FS.

In Figure 4.13 it is clear that there is a relatively linear relationship between the structure's total W/B ratio and the skin thickness. Smaller thicknesses result in lower W/B ratios. This shows that the decreased weight of a smaller skin thickness has a larger overall effect on the total W/B than the corresponding loss in buoyancy due to the skin being less rigid.

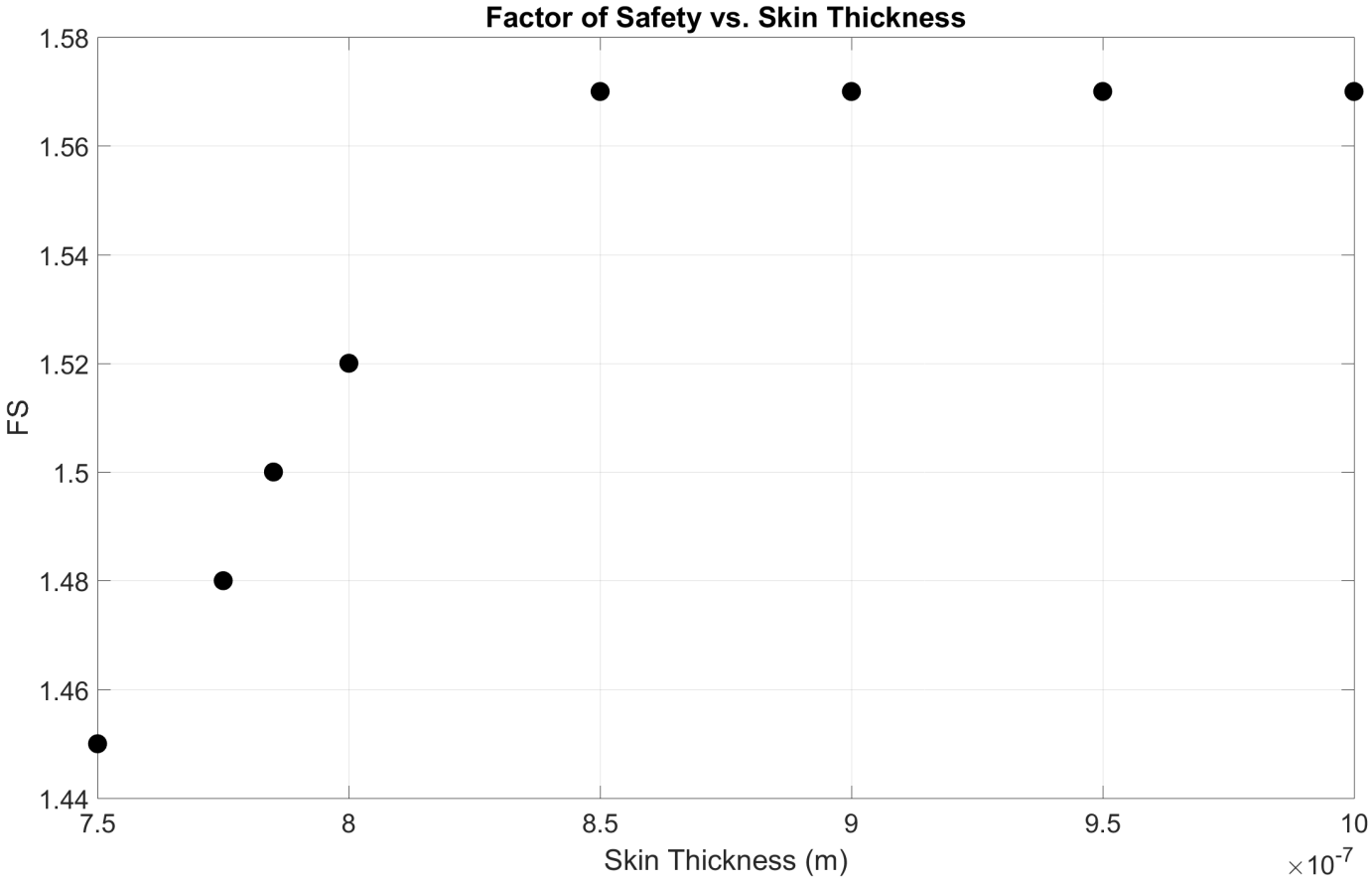

Figure 4.12. Plot of 0.8001 meter diameter models' FS vs. respective skin thicknesses

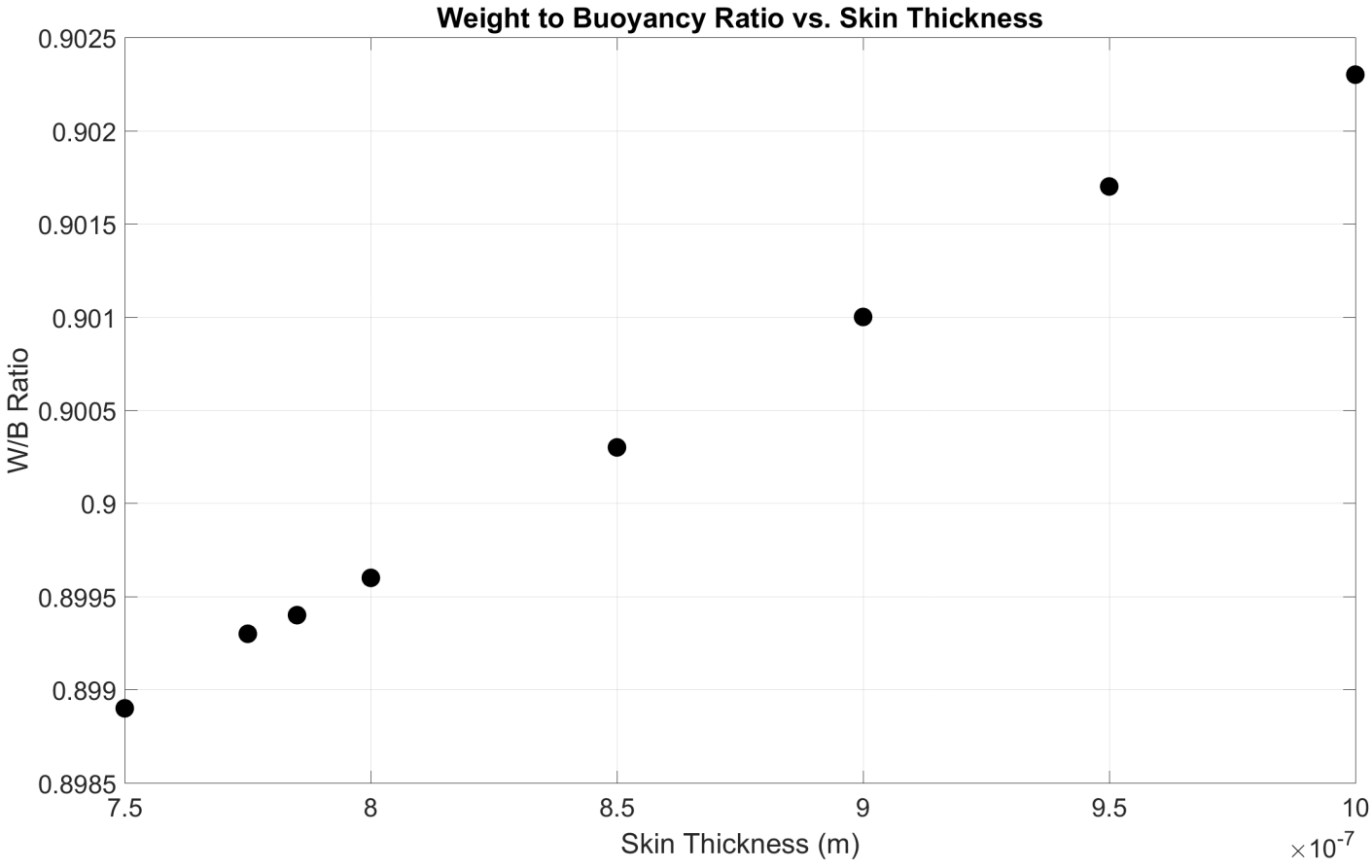

Figure 4.13. Plot of 0.8001 meter diameter models' W/B ratios vs. respective skin thicknesses

Figures 4.14 and 4.15 show the contour plots for the feasible design's deformation (magnitude) and VM stress respectively. The maximum deformation for the 0.8001 meter diameter model is 4.137e-02 meters. As is expected, the largest deformations occur in the skin at the centers of the curved triangular sections. The maximum VM stress for the model is 3.338e+10 Pascals. The largest stresses occur in the membrane along the beam, specifically at the centers of the beam sections (midpoints between ring connections).

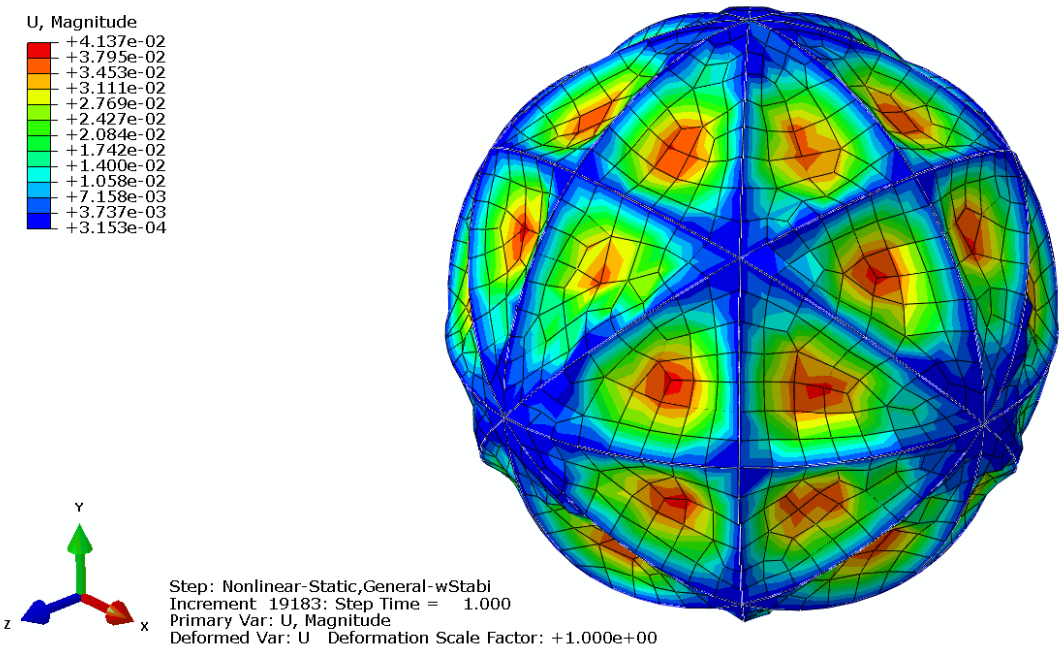

Figure 4.14. Deformation contour plot for the feasible 0.8001 meter diameter model

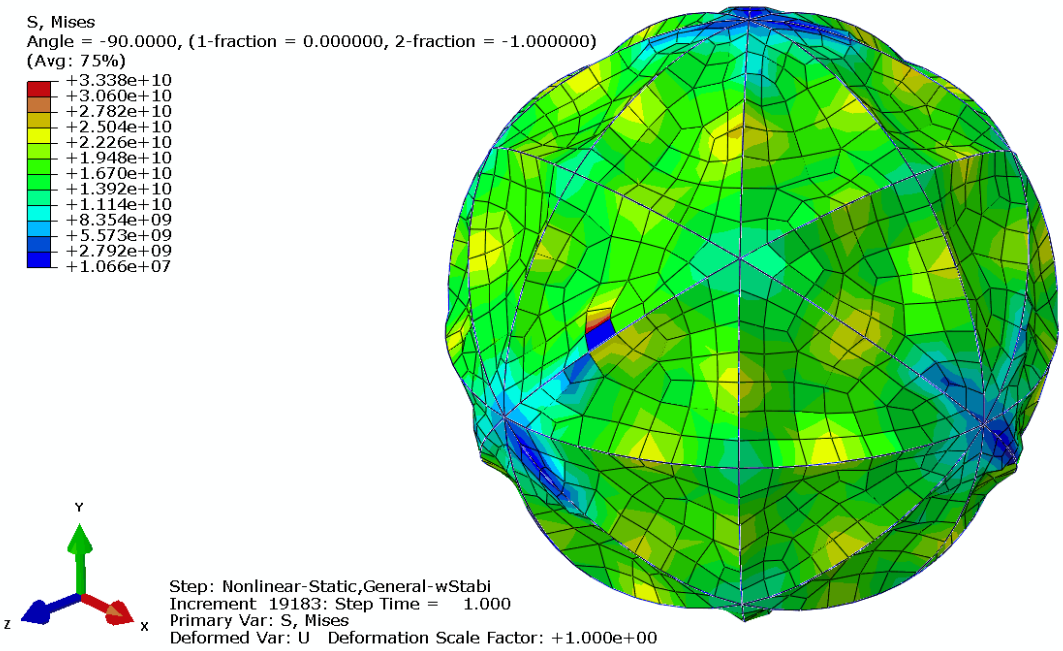

Figure 4.15. Von Mises stress contour plot for the feasible 0.8001 meter diameter model

Figures 4.16 and 4.17 show the plots of the magnitude of the deformation deformation at the tracked point within the frame and the skin respectively for the 0.8001 meter diameter model. For the most part the frame acts linearly. Up until around 10 percent of the total applied load, some nonlinear behavior does occur. After that point, a strong linear relationship is observed between the applied pressure and the deformation. Figure 4.17 on the other hand shows a nonlinear relationship between the applied load and the deformation within the skin. At around 10 percent of the applied pressure, a snapback phenomena is observed. After this point a more standard nonlinear trend follows.

The nonlinear behavior, in both the frame and the skin, may be attributed to the automatic adaptive stabilization that is used for the analysis. Between 0 and 10 percent of the total applied pressure, the total internal energy of the system may not be great enough for the stabilization to take effect. Because the membrane elements that make up the skin need the stabilization in order to handle transverse loads,

large deformations are observed in the skin for relatively low percentages of applied pressure. At around 10 percent of the total applied pressure, the internal energy seems to reach a threshold value where the adaptive stabilization is able to take effect. Once this happens, the skin is able to handle transverse loads, and all of the nonlinear behavior is transfered from the frame into the skin. The cause of the snapback behavior observed in the skin is still unknown. The phenomena may be a product of the stabilization settings that were used for this analysis.

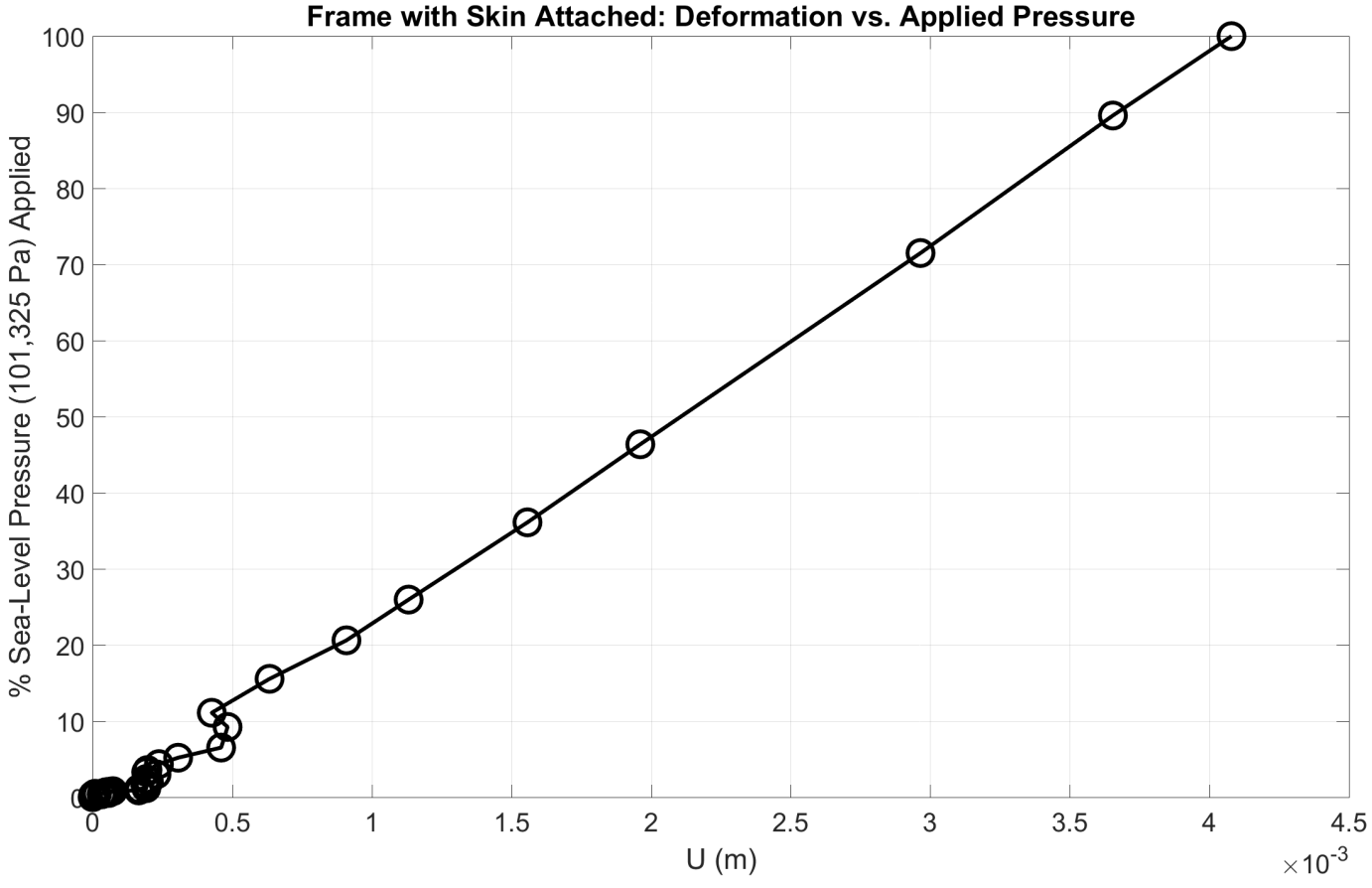

Figure 4.16. Plot of deformation (meters) vs. the percentage of sea-level pressure (101,325 Pa) applied for the frame with the skin attached of the 0.8001 meter diameter model

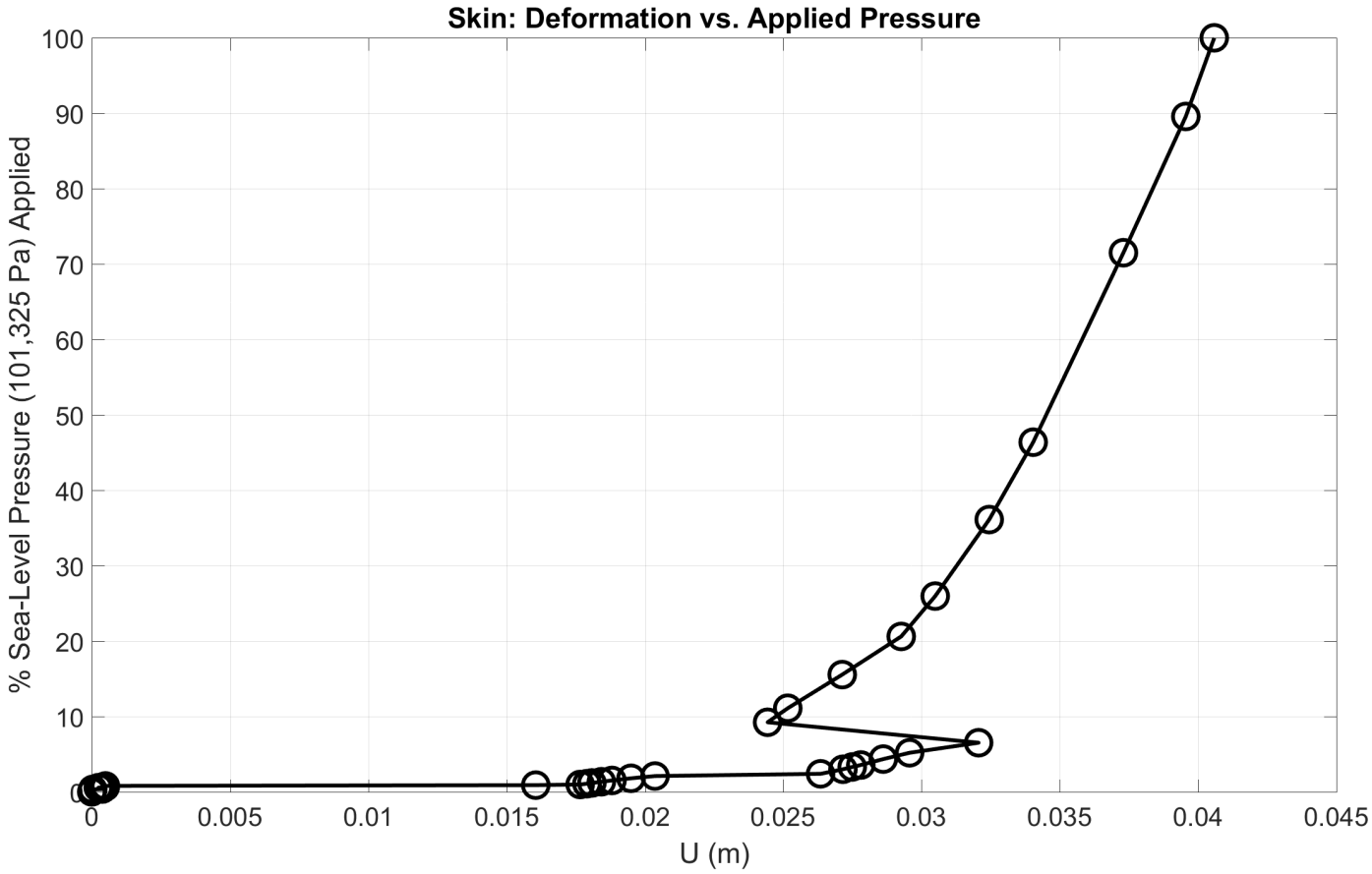

Figure 4.17. Plot of deformation (meters) vs. the percentage of sea-level pressure (101,325 Pa) applied for the skin of the 0.8001 meter diameter model

4.4 1.2192 Meter Diameter Model

The minimum W/B ratio for a 1.2192 meter structural diameter is 0.7257. The beam radius for the frame of this structure is 1.0925e-02 meters, the corresponding beam thickness of the frame is 2.73125e-04 meters. The structure weighs 804.53 grams with a maximum payload of 304.06 grams. The tabulated results for each iteration of the model can be found in Table 4.3.

Table 4.3. 1.2192 meter diameter results

D (m)	r_{beam} (m)	t_{beam} (m)	t_{skin} (m)	FS_{frame}	FS_{skin}	FS_{total}	W/B_{frame}	W/B_{skin}	W/B_{total}
1.2192	8.00e-03	2.00e-04	7.85e-07	0.44	1.44	0.44	0.4078	0.0070	0.4148
1.2192	1.20e-02	3.00e-04	7.85e-07	1.53	1.10	1.10	0.8622	0.0066	0.8687
1.2192	1.00e-02	2.50e-04	7.85e-07	0.87	1.22	0.87	0.6082	0.0067	0.6149
1.2192	1.05e-02	2.625e-04	7.85e-07	1.01	1.18	1.01	0.6667	0.0066	0.6733
1.2192	1.10e-02	2.75e-04	7.85e-07	1.17	1.14	1.14	0.7286	0.0066	0.7352
1.2192	1.09e-02	2.725e-04	7.85e-07	1.14	1.15	1.14	0.7160	0.0066	0.7226
1.2192	1.095e-02	2.7375e-04	7.85e-07	1.16	1.15	1.15	0.7223	0.0066	0.7289
1.2192	1.0925e-02	2.73125-04	7.85e-07	1.15	1.15	1.15	0.7191	0.0066	0.7257

The effect of the variation of the beam radius (along with the corresponding beam thickness for a c-ratio=0.025) on the structure's overall FS as well as W/B ratio is illustrated in Figures 4.18 and 4.19 respectively. The model's total FS is not directly affected by the changing beam dimensions until the beam radius is less than or equal to 1.09e-02 meters. For beam radii less than or equal to that value, the maximum VM stress in the model is transfered from the skin to the frame, and a proportional relationship exists between the beam dimensions and the model's total FS. A lower FS occurs for smaller beam dimensions.

There is a proportional relationship between the structure's total W/B ratio and the beam radius (with the corresponding beam thickness). Larger beam radii result in higher W/B ratios. This shows that the overall W/B ratio is impacted more by the increase in weight of the frame compared to the increase in total buoyancy resulting from a more rigid structure.

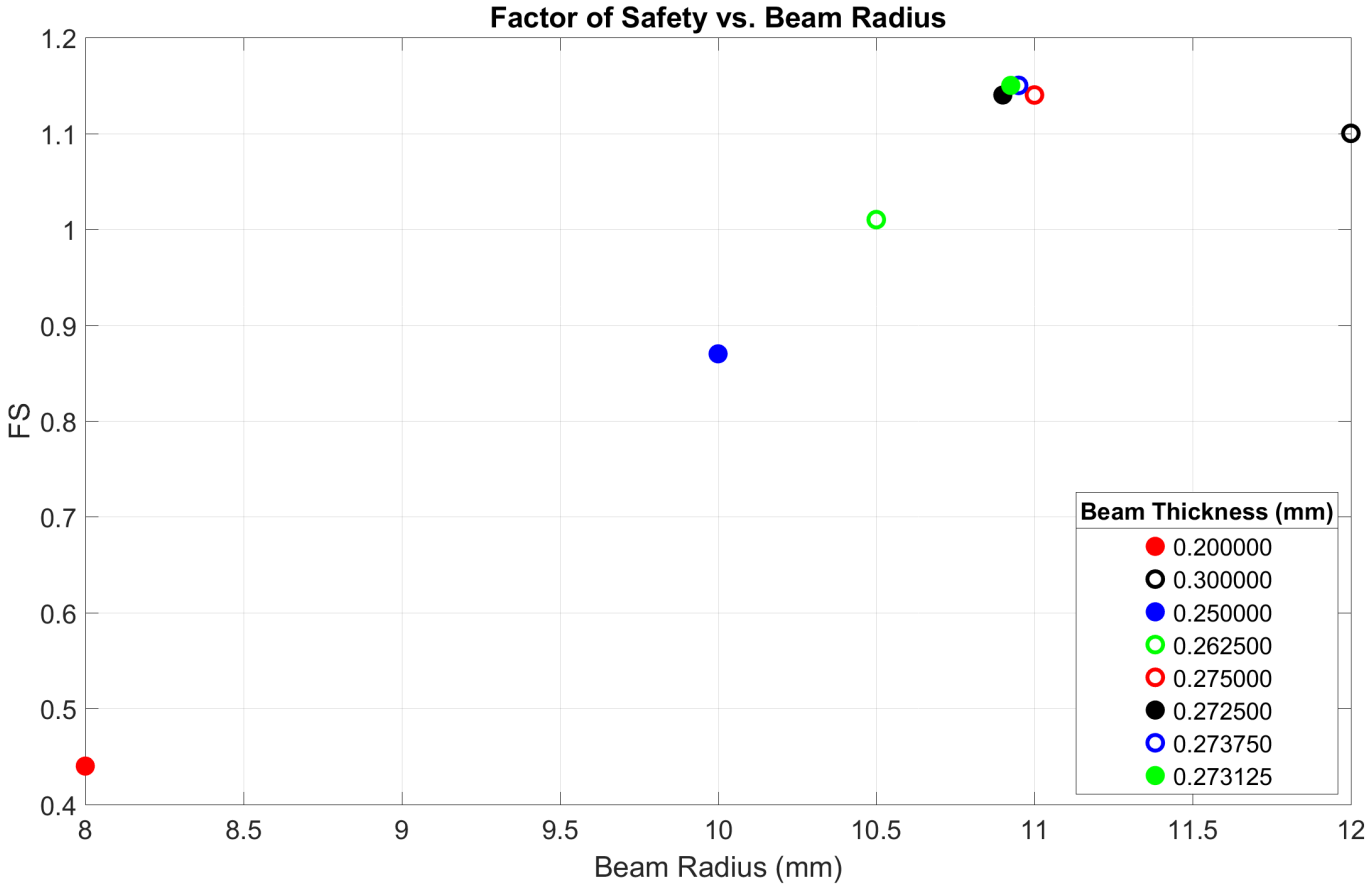

Figure 4.18. Plot of 1.2192 meter diameter models' FS vs. respective beam radii

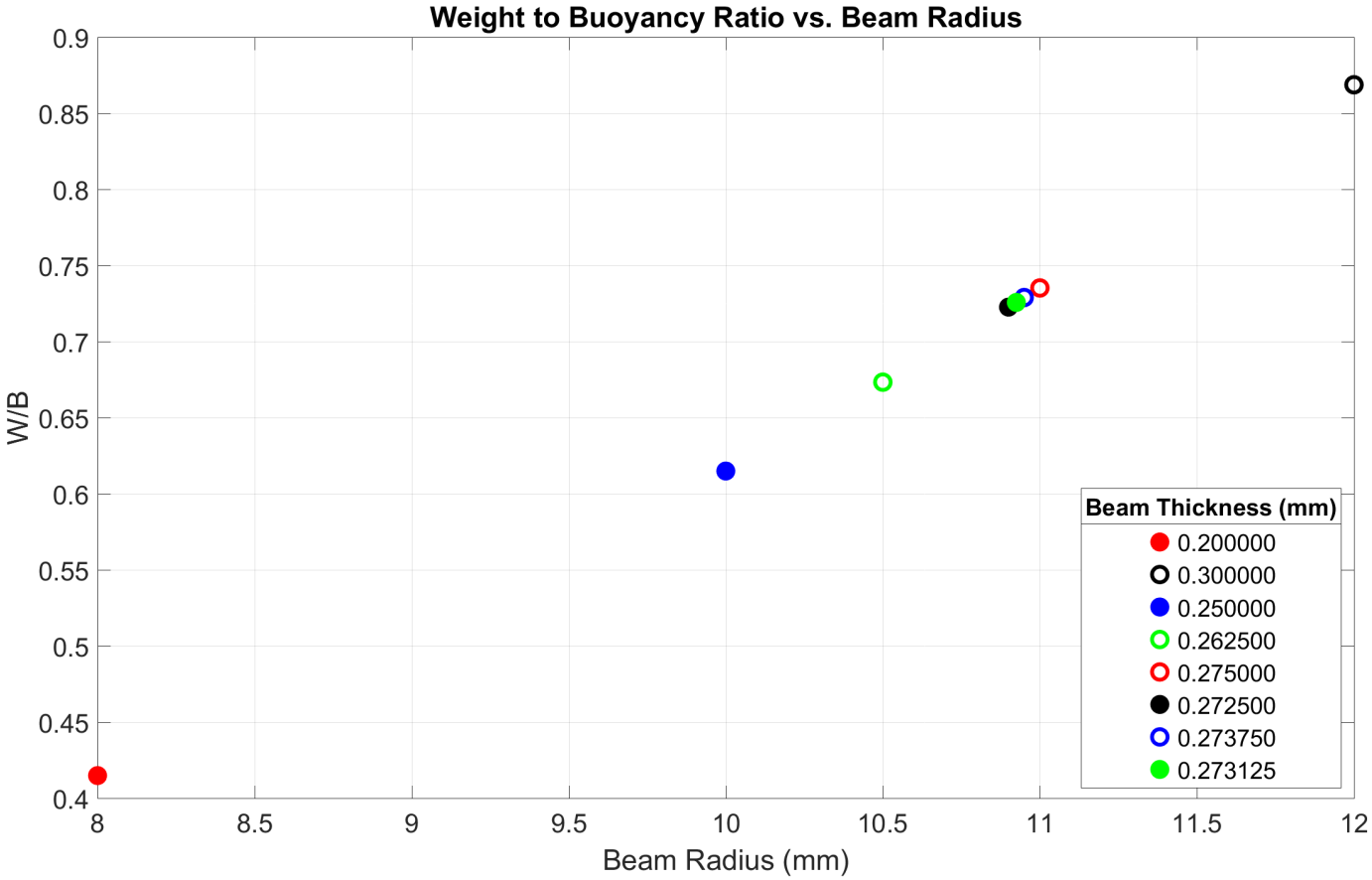

Figure 4.19. Plot of 1.2192 meter diameter models' W/B ratios vs. respective beam radii

The deformation and VM stress contour plots for the feasible 1.2192 meter diameter design can be found in Figures 4.20 and 4.21 respectively. The maximum deformation for the 1.2192 meter model is 7.131e-02 meters. As was seen on the 0.8001 meter diameter model, the largest deformations occur in the skin at the centers of each of the circular triangular sections. The maximum VM stress is 4.357e+10 Pascals. The largest stress values occur in the membrane covering the mid-point of the beams between ring connections.

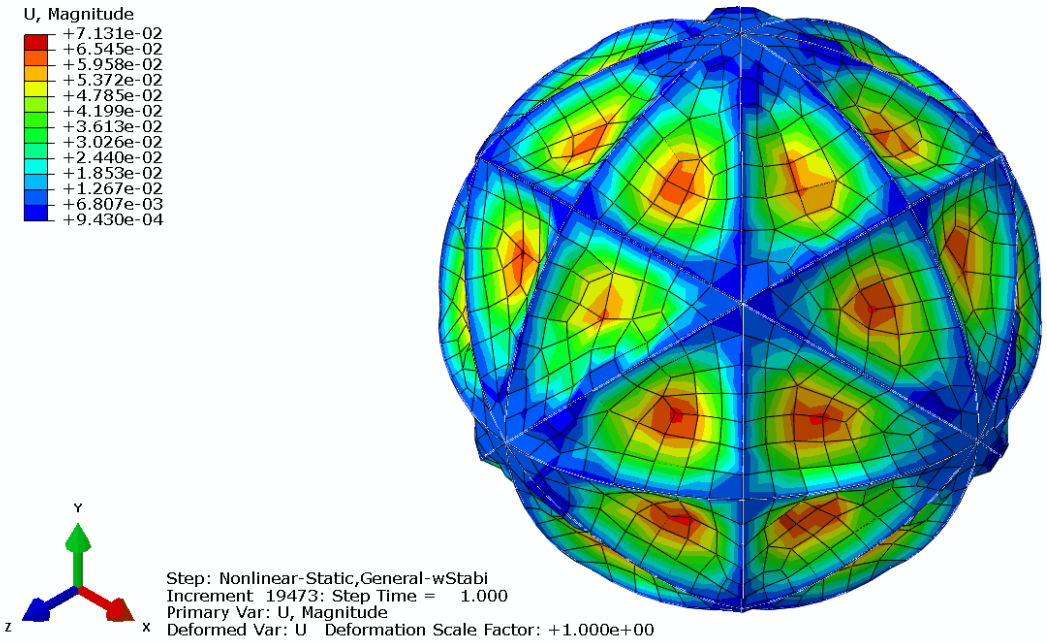

Figure 4.20. Deformation contour plot for the feasible 1.2192 meter diameter model

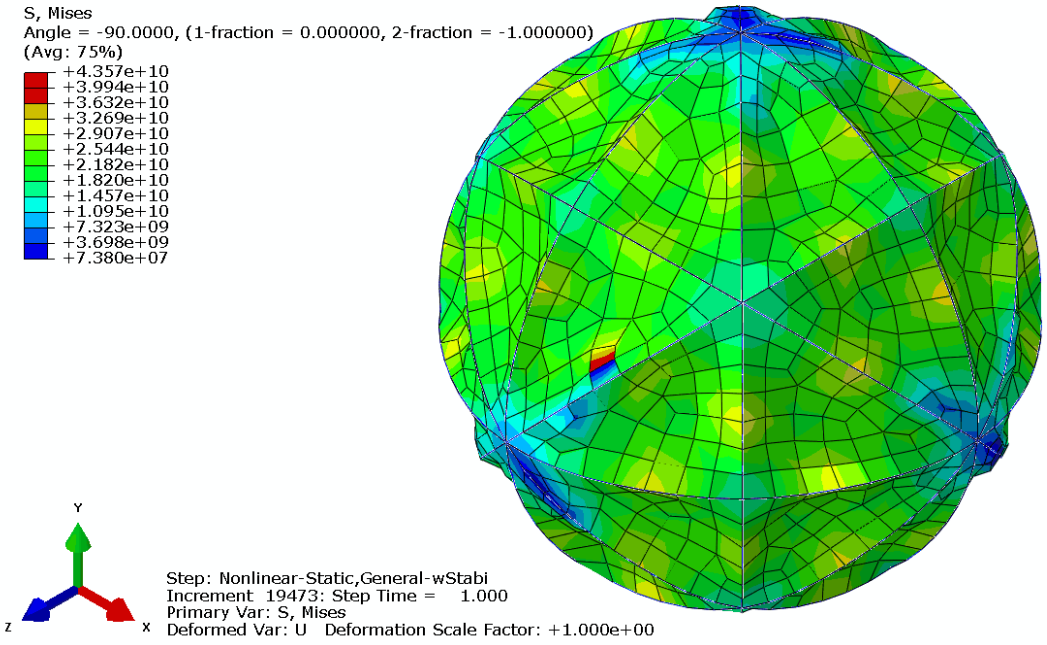

Figure 4.21. Von Mises stress contour plot for the feasible 1.2192 meter diameter model

Figures 4.22 and 4.23 show the plots of the magnitude of the deformation at the tracked point within the frame and the skin respectively for the 1.2192 meter diameter model. Both the frame and the skin of the 1.2192 meter diameter model follow the similar trends as the frame and skin of the 0.8001 meter diameter model. Fluctuations are observed in the frames response between 0 and 10 percent of the total applied pressure, and then the response goes linear. At this same point a snapback is observed in the skin's response. The automatic adaptive stabilization appears to take effect at around this point in the analysis; this trend was also observed in the 0.8001 meter diameter model.

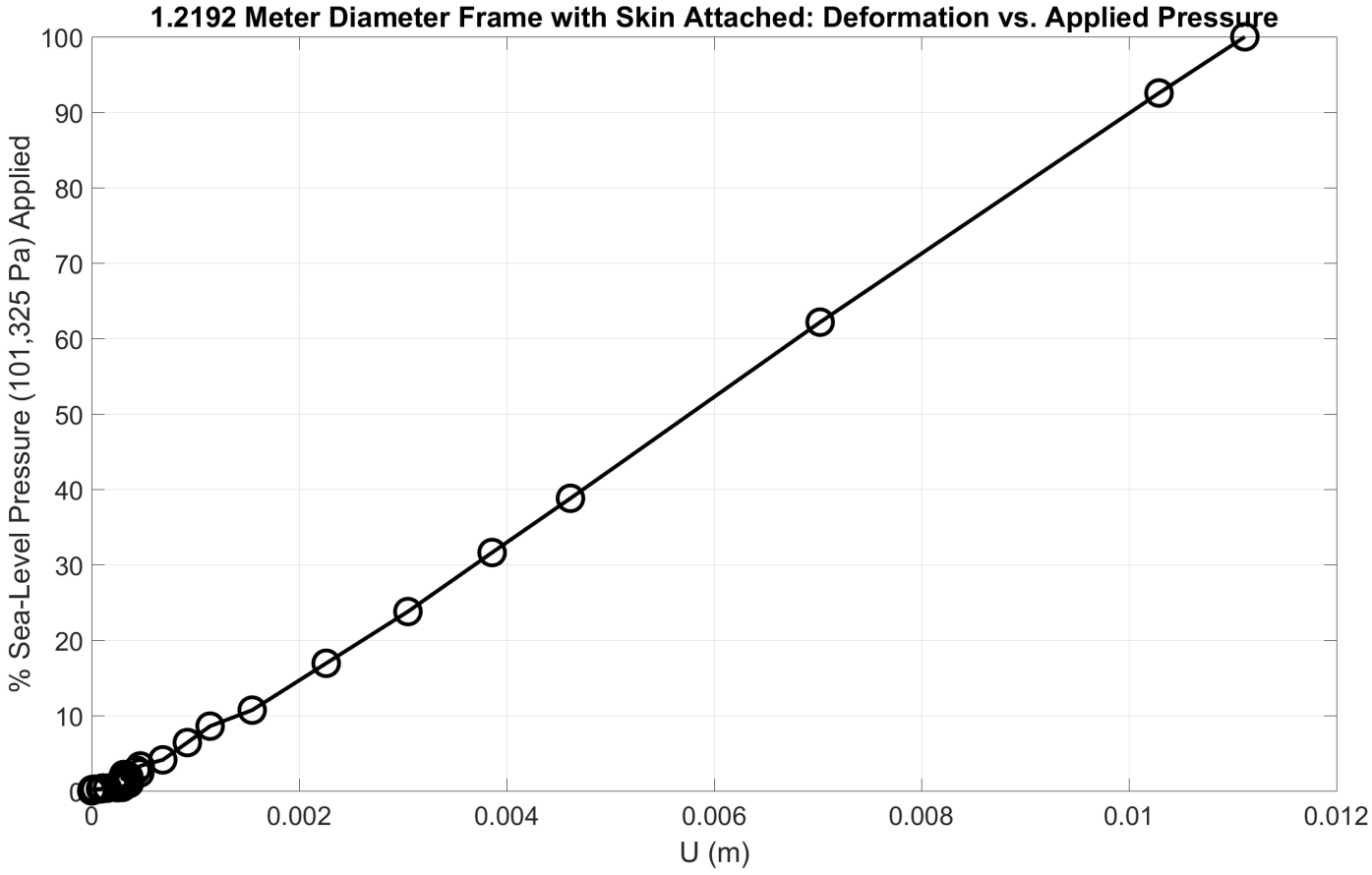

Figure 4.22. Plot of deformation (meters) vs. the percentage of sea-level pressure (101,325 Pa) applied for the frame with the skin attached of the 1.2192 meter diameter model

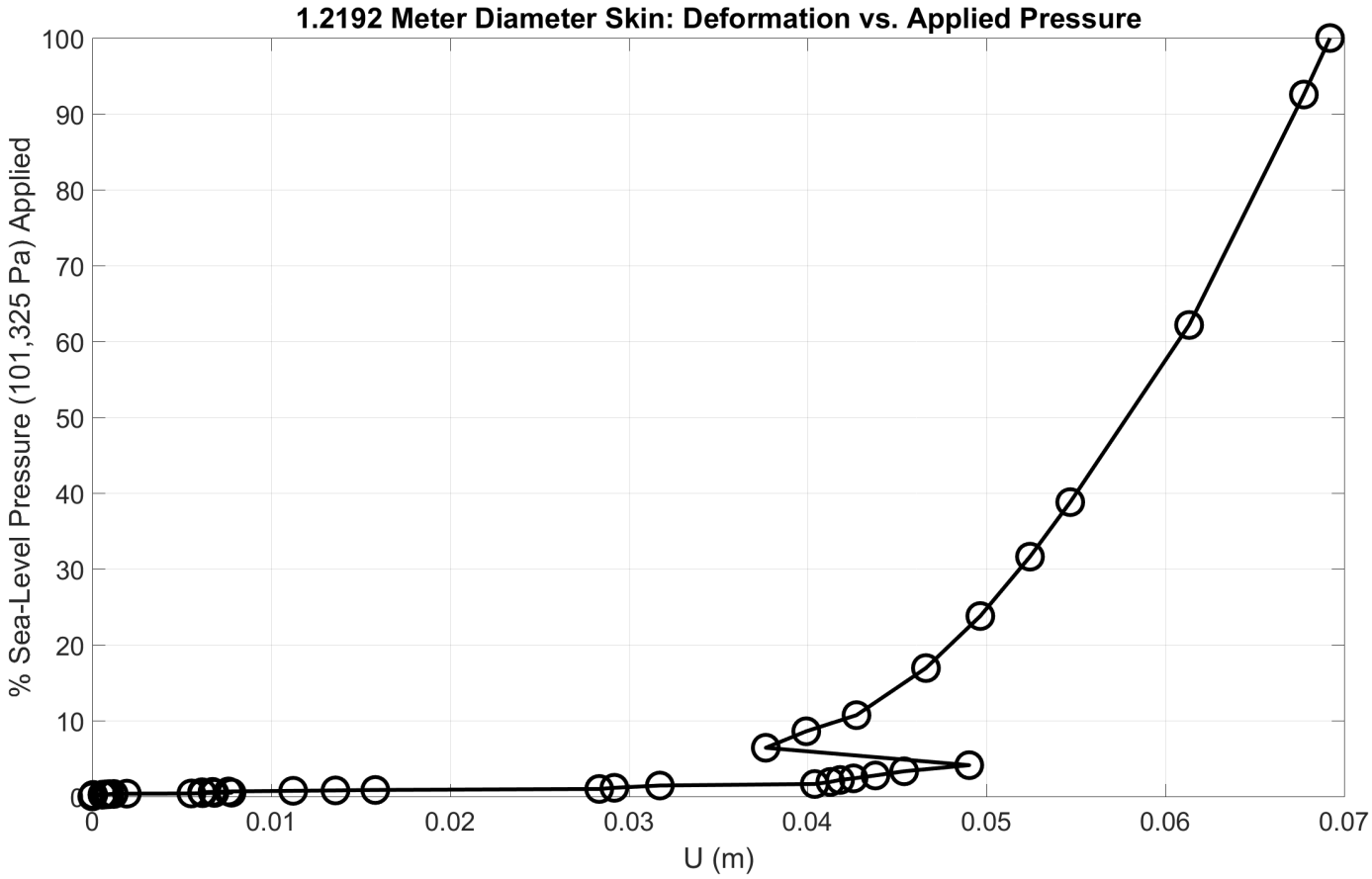

Figure 4.23. Plot of deformation (meters) vs. the percentage of sea-level pressure (101,325 Pa) applied for the skin of the 1.2192 meter diameter model

A tabulated comparison of the the feasible 1.2192 meter diameter models for the hexakis and celestial icosahedron designs can be found in Table 4.4. For the same FS, the celestial icosahedron design has a maximum payload of almost 100 grams more than the hexakis icosahedron's.

Table 4.4. 1.2192 meter diameter comparison

	Hexakis Icosahedron [7]	Celestial Icosahedron
Frame Material	CNT	CNT
Skin Material	Graphene	Graphene
D (m)	1.2192	1.2192
r_{beam} (m)	8.00e-03	1.0925e-02
t_{beam} (m)	2.00e-04	2.73125e-04
t_{skin} (m)	5.00e-07	7.85e-07
FS_{total}	1.15	1.15
W/B_{total}	0.7654	0.7257
Payload (g)	208.80	304.06

4.5 Minimum Diameter Model

The smallest diameter for a feasible celestial icosahedron design was found to be 0.7576 meters. The feasible design had a skin thickness equal to 7.70e-07 meters. The weight of this structure was 268.37 grams. This structure does not have the ability to carry a payload while maintaining positive buoyancy. The results for each iteration of the minimum diameter study can be found tabulated in Table 4.5.

Table 4.5. Minimum diameter results

D (m)	r_{beam} (m)	t_{beam} (m)	t_{skin} (m)	FS_{frame}	FS_{skin}	FS_{total}	W/B_{frame}	W/B_{skin}	W/B_{total}
0.8000	8.00e-03	2.00e-04	7.85e-07	1.58	1.50	1.50	0.8896	0.0100	0.8996
0.7500	8.00e-03	2.00e-04	7.85e-07	1.90	1.53	1.53	1.0093	0.0106	1.0200
0.7750	8.00e-03	2.00e-04	7.85e-07	1.73	1.52	1.52	0.9465	0.0103	0.9569
0.7625	8.00e-03	2.00e-04	7.85e-07	1.80	1.52	1.52	0.9772	0.0105	0.9877
0.7563	8.00e-03	2.00e-04	7.85e-07	1.85	1.52	1.52	0.9930	0.0106	1.0036
0.7594	8.00e-03	2.00e-04	7.85e-07	1.83	1.52	1.52	0.9851	0.0105	0.9956
0.7578	8.00e-03	2.00e-04	7.85e-07	1.84	1.52	1.52	0.9890	0.0105	0.9996
0.7570	8.00e-03	2.00e-04	7.85e-07	1.84	1.52	1.52	0.9910	0.0106	1.0016
0.7570	8.00e-03	2.00e-04	7.50e-07	1.85	1.48	1.48	0.9910	0.0101	1.0011
0.7574	8.00e-03	2.00e-04	7.85e-07	1.83	1.52	1.52	0.9900	0.0105	1.0006
0.7574	8.00e-03	2.00e-04	7.50e-07	1.85	1.48	1.48	0.9900	0.0101	1.0001
0.7576	8.00e-03	2.00e-04	7.85e-07	1.84	1.52	1.52	0.9895	0.0105	1.0001
0.7576	8.00e-03	2.00e-04	7.75e-07	1.84	1.51	1.51	0.9895	0.0104	0.9999
0.7576	8.00e-03	2.00e-04	7.65e-07	1.84	1.49	1.49	0.9895	0.0103	0.9998
0.7576	8.00e-03	2.00e-04	7.675e-07	1.84	1.50	1.50	0.9895	0.0103	0.9998
0.7575	8.00e-03	2.00e-04	7.675e-07	1.84	1.50	1.50	0.9898	0.0103	1.0001
0.7576	8.00e-03	2.00e-04	7.70e-07	1.84	1.50	1.50	0.9895	0.0103	0.9999

The effect of the variation of the structural diameter, as well as the skin thickness, on the structure's overall FS and W/B ratio is illustrated in Figures 4.24 and 4.25 respectively. In general, smaller structural diameters result in larger total FS. Structures with smaller diameters are more rigid than structures with larger diameters. At a constant structural diameter, we see a proportional relationship between the skin

thickness and the structure's total FS. Larger skin thicknesses result in higher FS. For the small changes in diameter plotted in Figure 4.24 ($\leq$0.008 meters), a given skin thickness's corresponding FS is not affected by a change in diameter. In this range of diameters, all of the models' maximum stresses are found in the skin.

Larger diameter structures yield lower W/B ratios than smaller diameter structures. This observation is line with the cube-square rule referenced in Section 1.4. For a given structural diameter, skin thickness is proportional to the structure's total W/B ratio. Larger skin thicknesses result in higher W/B ratios.

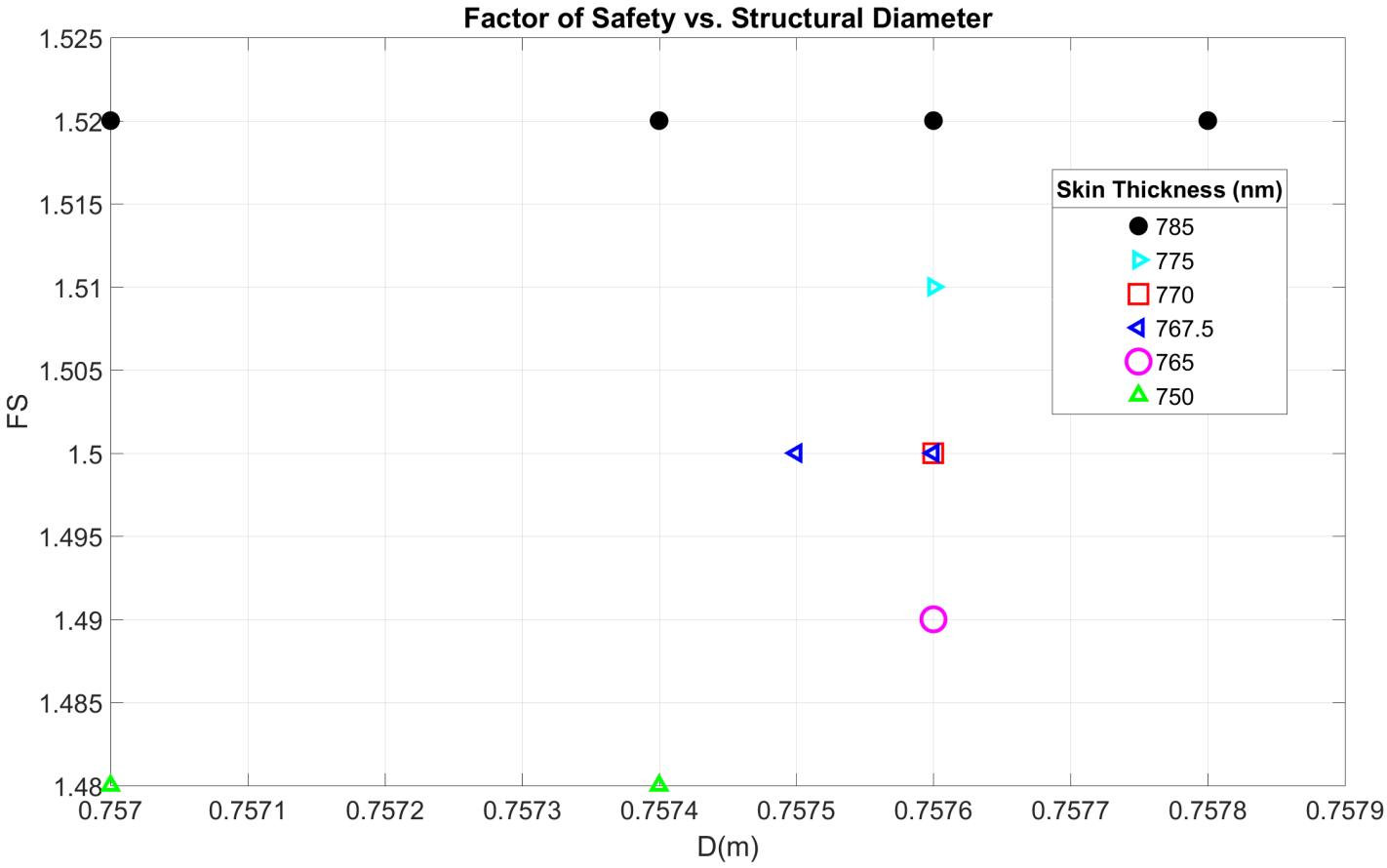

Figure 4.24. Plot of minimum diameter models' FS vs. respective structural diameters

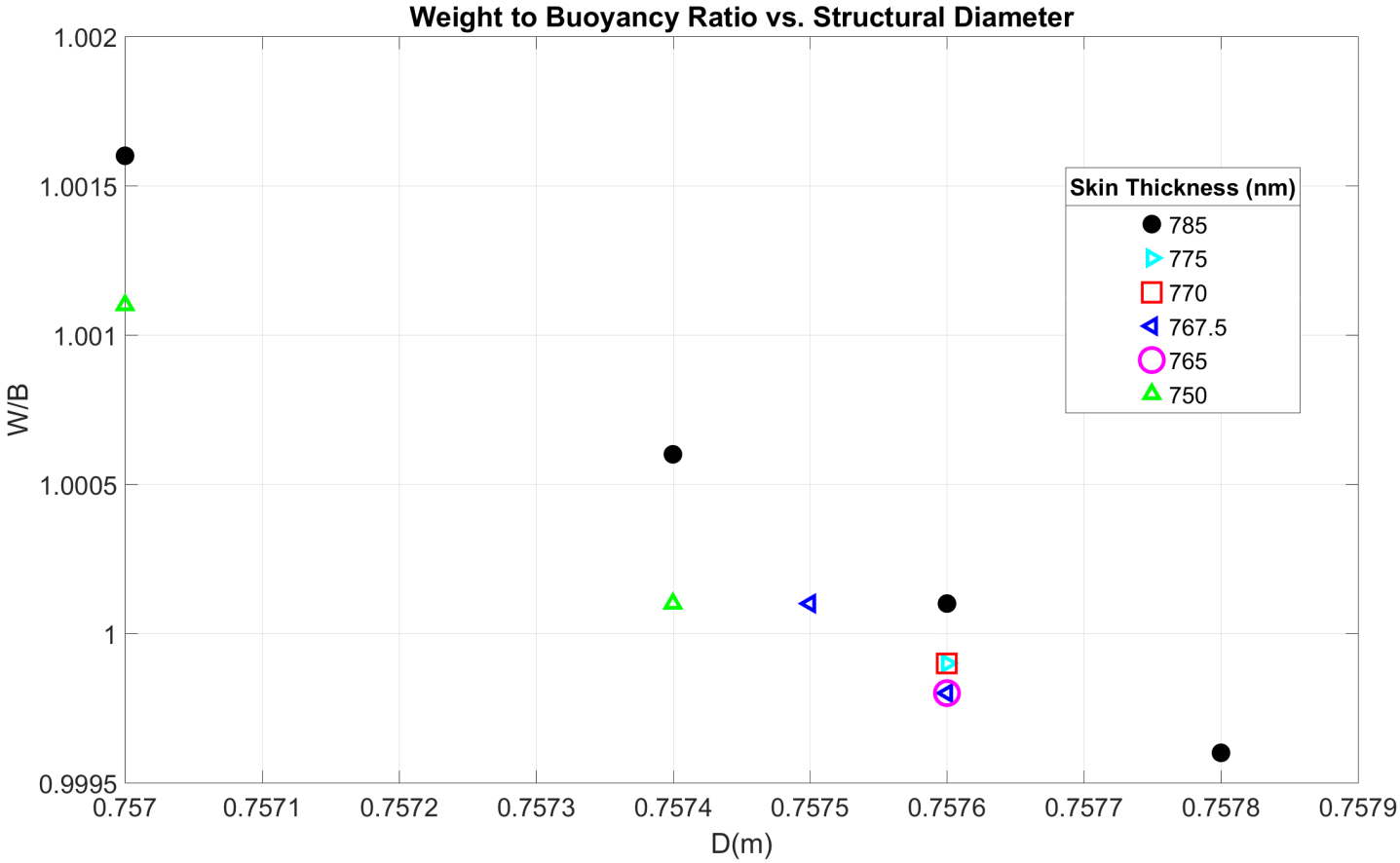

Figure 4.25. Plot of minimum diameter models' W/B ratios vs. respective structural diameters

The deformation and VM stress contour plots for the feasible minimum diameter design (0.7576 meters) can be found in Figures 4.26 and 4.27 respectively. The maximum deformation for the minimum diameter model is 3.835e-02 meters. In line with the previous two studies, the largest deformations are located in the skin at the centers of each of the circular triangular sections. The maximum VM stress is 3.344e+10 Pascals. The highest stresses are located within the skin located on the mid-point of the beam.

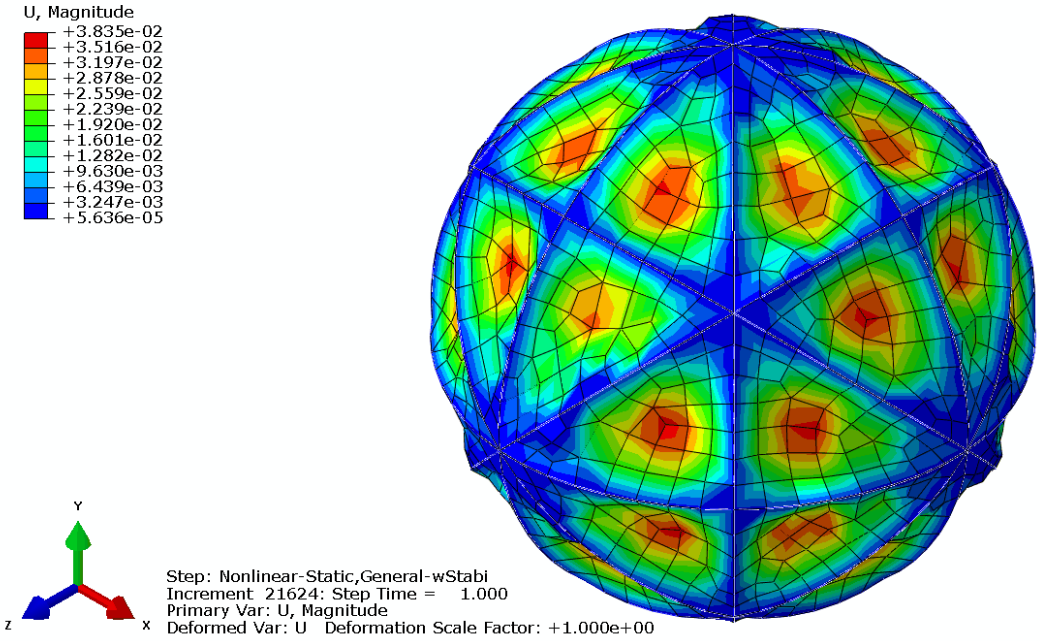

Figure 4.26. Deformation contour plot for the feasible minimum diameter model (0.7576 meters)

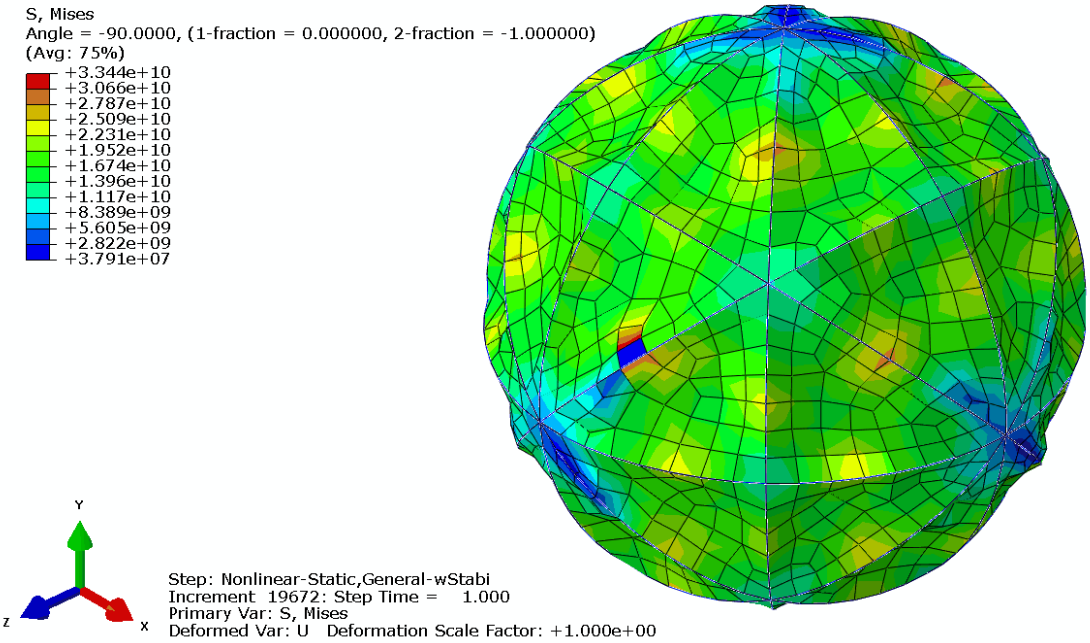

Figure 4.27. Von Mises stress contour plot for the feasible minimum diameter model (0.7576 meters)

Figures 4.28 and 4.29 show the plots of the deformation at the tracked point within the frame and skin respectively for the minimum diameter model. Once again, similar nonlinear behavior is present within the frame and the skin. The smaller, 0.7576 meter diameter model differs from the larger models in that the stabilization appears to take effect later in the analysis at around 15 percent of the total applied pressure. The 0.7576 meter diameter model also differs from the larger models in that the snapback behavior is not observed. This may be due to the parameters used in the automatic adaptive stabilization. Alternatively, the lack of snapback behavior may be due to the increased rigidity of the smaller model.

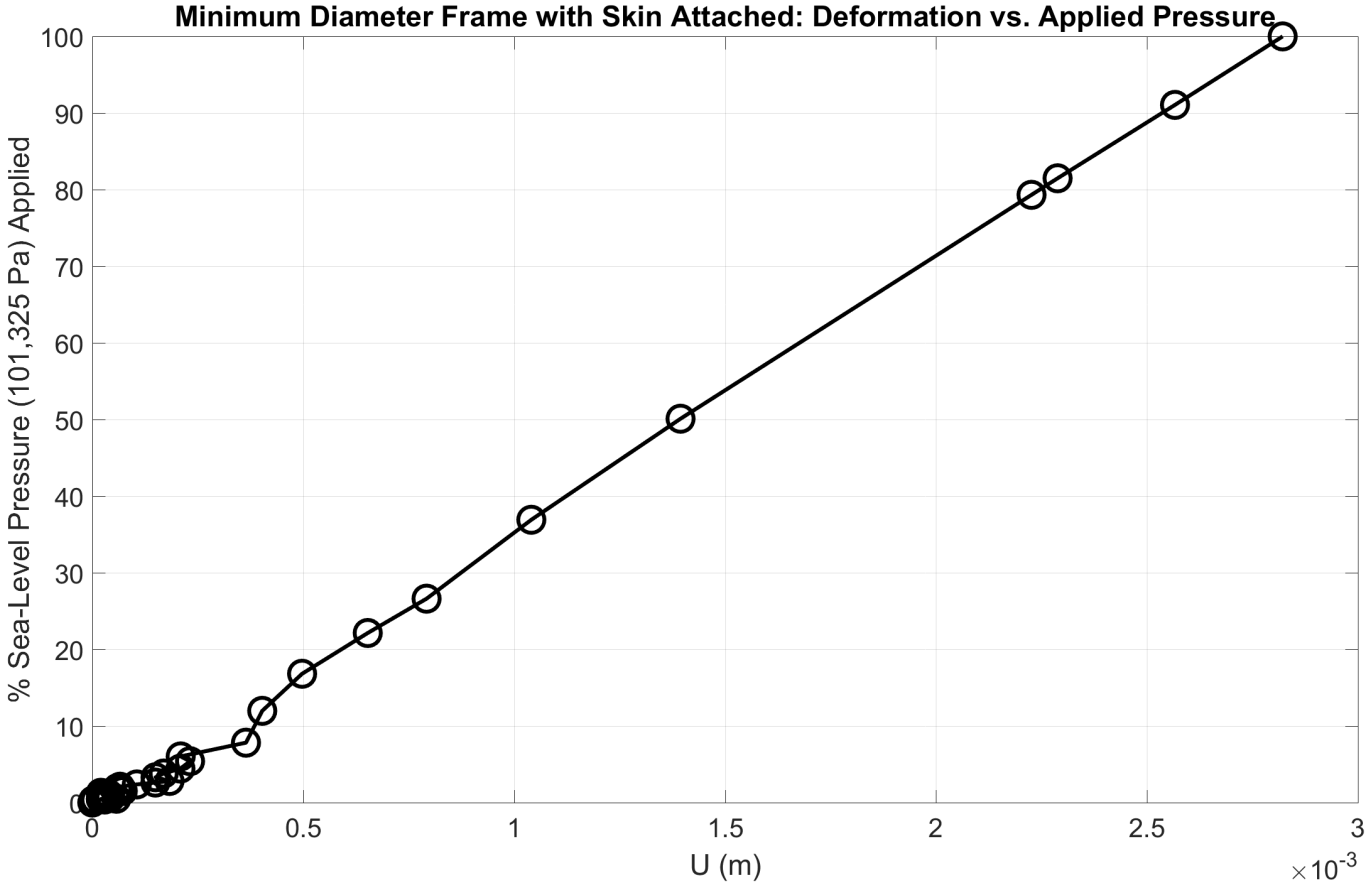

Figure 4.28. Plot of deformation (meters) vs. the percentage of sea-level pressure (101,325 Pa) applied for the frame with the skin attached of the minimum diameter model

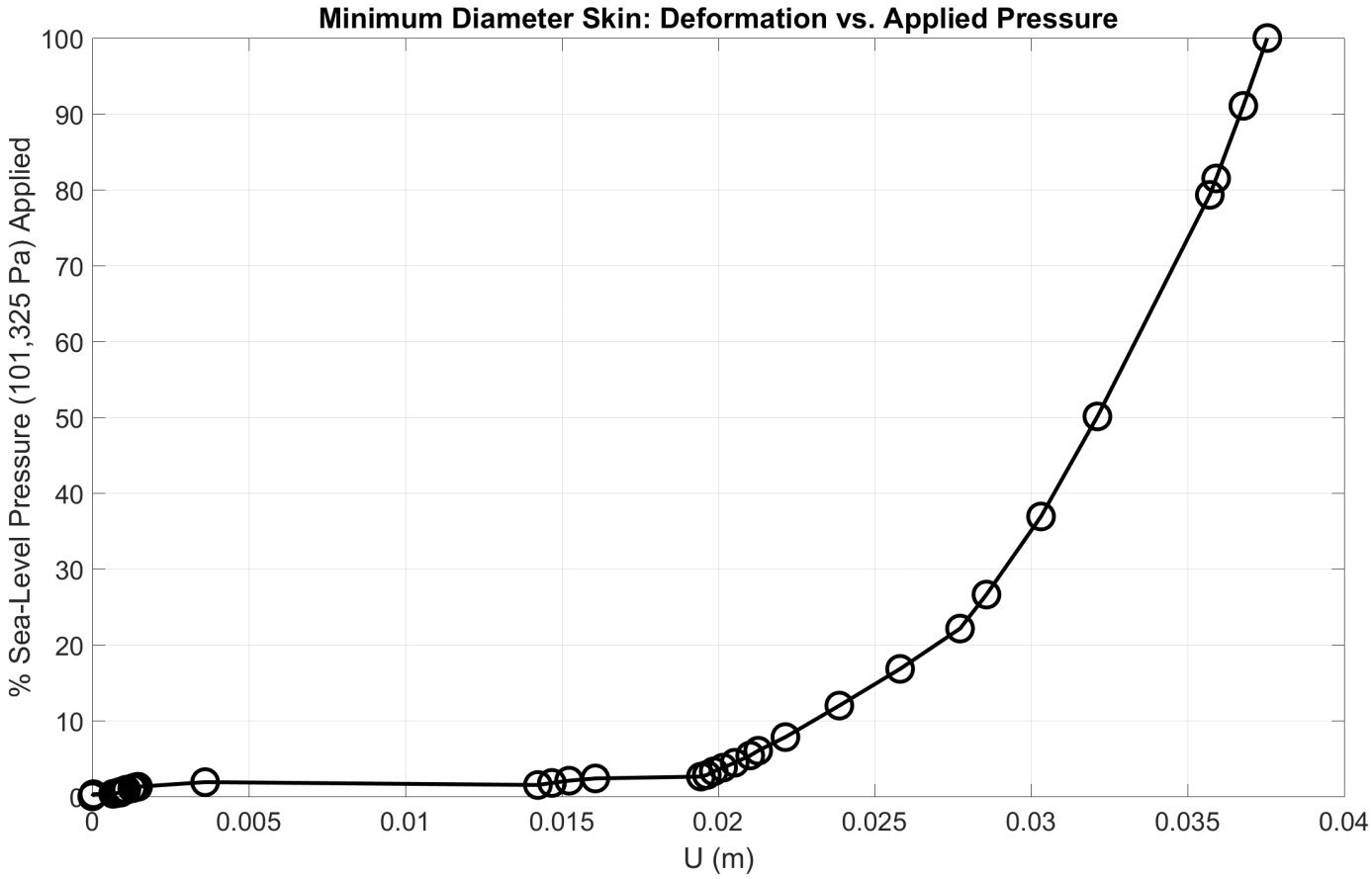

Figure 4.29. Plot of deformation (meters) vs. the percentage of sea-level pressure (101,325 Pa) applied for the skin of the minimum diameter model

4.6 Summary

The results described in this chapter show the overall feasibility of the celestial icosahedron design for a VLTAV. The boundary condition study reveals the linear, symmetric nature of the frame under laterally constrained and unconstrained vertices, and the three models of different diameters demonstrate the feasibility of specific designs. Nonlinear behavior was observed in the skins of the three full models. The specifications of the three different models can be found in Table 4.6.

Table 4.6. Summary of feasible designs

D (m)	0.8001	1.2192	0.7576
Frame Material	CNT	CNT	CNT
Skin Material	Graphene	Graphene	Graphene
r_{beam} (m)	8.00e-03	1.0925e-02	8.00e-03
t_{beam} (m)	2.00e-04	2.73125e-04	2.00e-04
t_{skin} (m)	7.85e-07	7.85e-07	7.70e-07
FS_{total}	1.50	1.15	1.50
W/B_{total}	0.8994	0.7257	0.9999
Payload (g)	31.72	304.06	0

V. Conclusions and Recommendations

With the boundary condition study, as well as the analyses of the 0.8001 meter, 1.2192 meter, and minimum diameter models, it is concluded that the celestial icosahedron is a feasible design for a vacuum lighter than air vehicle (VLTAV).

The boundary condition study showed that a symmetric response is present within the frame of the celestial icosahedron design under a simulated sea-level pressure load when boundary condition 3 (U1=U3=0) is applied to the top and bottom vertices. Because of the symmetry that was achieved with the use of boundary condition 3, lower maximum values for the magnitude of deformation were experienced by the frame. By tracking the deformation of a point on the frame as the load was applied, the frame was verified to have had a linear response when no skin is attached.

The 0.8001 meter diameter model was produced to find the minimum weight-to-buoyancy (W/B) ratio possible for a model capable of fitting through an Americans with Disabilities Act (ADA) approved doorway. The minimum W/B ratio achieved for this model was 0.8994, resulting in a maximum payload of 31.72 grams. The total factor of safety (FS) for the 0.8001 meter diameter model was not affected by the skin thickness until the skin thickness was less than or equal to 8.00e-07 meters. For skin thicknesses less than or equal to 8.00e-07 meters, a linear relationship between the skin thickness and the total FS was observed; a smaller skin thickness resulted in a lower FS.

For all the skin thicknesses tested with the 0.8001 meter diameter model, the total W/B ratio was linearly dependent on the skin thickness; smaller skin thicknesses resulted in lower W/B ratios, proving that the decrease in weight due to smaller skin thickness values have a larger overall effect on the model's total W/B ratio than the corresponding loss in buoyancy caused by a less rigid, thinner skin.

In order to validate the linearity study conducted on the frame without the skin

attached, the same tracked point was studied for all three of the models with the skin attached. A generally linear response was observed in the frame of the 0.8001 meter diameter model with the skin attached. A point within the skin was then tracked, and a nonlinear response was observed. Notably, snapback behavior occurred at around 10 percent of the total applied load. The behavior at around 10 percent of the total applied pressure may be attributed to automatic adaptive stabilization used for this analysis. This shows that the majority of the nonlinear behavior present in the 0.8001 meter diameter model lies within the skin.

The 1.2192 meter (4 foot) diameter model was produced in order to compare the celestial icosahedron's performance to that of the hexakis icosahedron. Overall, the celestial icosahedron preformed better than the hexakis icosahedron. For the same materials and FS, the celestial icosahedron is able to carry almost 100 grams more in payload than hexakis icosahedron.

Beam radii, along with the corresponding beam thickness, for the 1.2192 meter diameter model were varied. For beam radii less than or equal to 1.09e-02 meters, a proportional relationship was observed between the beam dimensions and the model's overall FS; smaller beam dimensions yield lower total FS. For beam radii greater than 1.09e-02 meters, the maximum Von Mises (VM) stress is contained in the skin.

For the 1.2192 meter diameter model, a linear relationship was observed between the beam radii, along with the corresponding beam thicknesses, and the model's total W/B ratio; smaller beam radii resulted in lower overall W/B ratios. This verifies that the overall W/B ratio is effected more by the increase in the weight of the frame than the increase in the buoyancy of the structure produced by a more rigid model.

The linearity study for the 1.2192 meter diameter model yielded similar results as the 0.8001 meter diameter model. Aside from small fluctuations occurring at around 10 percent of the total applied pressure, a strong linear relationship was present in

the frame. The skin of the 1.2192 meter diameter model displayed nonlinear behavior with a snapback occurring at around 10 percent of the total applied pressure.

The minimum diameter model was produced in order to determine the smallest diameter achievable for a celestial icosahedron VLTAV to achieve positive buoyancy with no payload. The minimum diameter obtained was 0.7576 meters and showed very similar FS and W/B ratio trends as the previous two models. In general, the diameter of the structure and the model's total FS were linearly proportional; a smaller diameter resulted in a larger FS. For changes in diameter less than 0.008 meters, though, the total FS corresponding to a given skin thickness is unchanged. Similar to the 0.8001 meter diameter model, larger skin thicknesses on the minimum diameter model resulted in a higher FS for the entire structure.

The structure's diameter and its total W/B ratio are linearly dependent; a larger diameter results in a lower W/B ratio. For a given structural diameter, a smaller skin thickness resulted in a lower overall W/B ratio. Once again, the relationship between skin thickness and overall W/B ratio was linear in nature.

The linearity study for the minimum diameter model yielded similar results in the frame. Linear behavior was present after about 15 percent of the total applied pressure, with small fluctuations occurring up until the 15 percent mark. The skin's behavior on the other hand differed for the minimum diameter model compared to the larger 0.8001 meter and 1.2192 meter diameter models. Although nonlinear behavior was present within the skin of the minimum diameter model, the snapback behavior present in the other two models did not occur.

For all three of the models analyzed, the largest deformations were observed at the centers of each of the curved triangular sections. Likewise, the largest VM stress values occurred in the membrane covering the mid-points of the beams between the ring connections. The frames of each model showed mostly linear behavior with the

skins exhibiting nonlinear behavior.

This research produced three feasible models of different diameters (0.8001, 1.2192, and 0.7576 meters), all of which met their respective W/B ratio and FS requirements. Although further research is necessary in order to produce an operational, celestial icosahedron VLTAV, the celestial icosahedron is a design that has a lot of potential.

5.1 Future Research

As this study was preliminary in nature, there is much more research to be conducted on the celestial icosahedron VLTAV. As far as quasi-static analysis goes, more precise optimization methods can be employed in formulating feasible designs.

A major area of research that needs to be conducted on the celestial icosahedron is a continuation of the linearity study conducted on the three full models. A more in depth analysis of what is going on in the frame and skin at about 10 percent of the total applied load needs to be carried out. The behavior observed in this research may be due to numerical inaccuracies within the finite element model (FEM), or it could be the product of some physical phenomena not yet known.

In line with the studies conducted on the icosahedron and hexakis icosahedron designs, dynamic finite element analysis (FEA) studies must be conducted in the future. Furthermore, validation of this research may be carried out through experimental studies. An additively manufactured model of the frame structure has been constructed which may be used for experimental testing, to include compression tests and wind tunnel tests. Finally, it is necessary that air evacuation methods be tested for this particular design.

Appendix A. Matlab Tutorial

The purpose of this section is to explain the Matlab script found in Appendix B. The script found in Appendix B was created for a celestial icosahedron model 2 feet in diameter. In order to run this script, it is advised that it is kept in a file along with the corresponding input (.inp) file.

The diameter of the structure is manually entered by the user (in feet) on line 19. For ease of use, it is best to start with an .inp file of a standard dimension (1 foot or 1 meter). By doing so, the user can easily change the diameter of the model as desired by uncommenting lines 169-207 and lines 209-248.

Lines 169-207 correspond to the modification of the frame and lines 209-248 correspond to the modification of the skin. It is advised that the user makes these changes separately, frame first and then skin. Make sure that the formatting of the .inp file is correct after each modification as errors have been known to occur. Do not forget to comment out the frame modification lines before moving on to the skin if this is being carried out separately.

Lines 29 and 30 are where the user enters the yield stresses for the frame and skin materials respectively. The skin thickness can be changed by the user at line 33. By entering the skin thickness here, the .inp is updated automatically by the script (lines 35-51).

From here different values are read into Matlab from the .inp file. These values will be needed later for factor of safety (FS) and weight-to-buoyancy (W/B) ratio calculations.

Lines 287-292 are used to run the .inp file. The number of processors used to run the .inp can be input in line 290 where the script says "cpus=#." Lines 294-298 are only used to terminate a job if that is deemed necessary by the user. Typically those lines are always kept commented out unless needed.

For large jobs, it is best to comment out all of the script that comes after line 292 until after the job has completed. Once the job has completed, the user must comment out lines 287-292 to keep the job from running again (and overwriting the data and files already saved).

The remaining lines (303-430) read in data from the .dat file which is produced after a completed job. This data is used to calculate the model's FS and W/B ratio. The results, as well as the dimensions of the model are printed out at the end. Figure B.1 is an example of one of those printouts.

Appendix B. Matlab Code

```
%%  Weight to Buoyancy and FS Calculations for Celestial Icosahedron
... w/ CNT Frame and Graphene skin
... 2 ft structural Diameter
... smallest manufacturable pipe dimensions
... 500 nanometer skin thickness

close all
clear all
clc

%% print materials used in construction of model
fprintf('-----------------------------------------------------------------\n')
fprintf('MODEL\n');
fprintf('-----------------------------------------------------------------\n\n')
fprintf('Frame Material: Carbon Nanotube (CNT) Composite\n\n')
fprintf('Skin Material : Graphene\n\n')

%% structural diameter
Diameter_ft = 2;                    % structural diamter in feet
Diameter_m = Diameter_ft*.3048;     % diameter in meters

fprintf('Diameter: %4.2f ft (%4.4f m)\n\n', Diameter_ft,Diameter_m)

%% constants
g0 = 9.81;      % acceleration of gravity at SL (m/s^2)
rho_air = 1.225;    % mass density of air at SL (kg/m^3)

%% material properties (yield stresses)
Sy_frame = 3.8e9; % yield stress for CNT composite (Pa)
```

```
30 Sy_skin = 5e10; % yield stress for Graphene (Pa)
31
32 %% skin thickness
33 t_skin = 1.92464*10^(-5);     % skin thickness from Cranston's model (m)
34
35 %% change skin thickness in .inp file
36 % find location of skin thickness in .inp file
37 fid=fopen('Sample.inp');
38 txt =textscan(fid,'%s','delimiter','\n');
39 rows = txt{1,1};
40 irows_begin = find(ismember(rows,'*Membrane Section, elset="Skin ...
       Instance__PickedSet31", material="Skin Material", poisson=0.33'));
41 irows_end = find(ismember(rows,'*System'));
42 fclose(fid);
43
44 % print new skin thickness in .inp file
45 M_before = rows(irows_begin+1:irows_end-1);
46 M = sprintf('%0.5g,',t_skin);  %Change t_skin in INP file
47 rows = [rows(1:irows_begin); M; rows(irows_end:end);];
48
49 fid = fopen('Sample.inp','wt');
50 fprintf(fid,'%s\n', rows{:});
51 fclose(fid);
52
53 %% read in frame dimensions (pipe radius and thickness) from .inp file
54 fid=fopen('Sample.inp');
55 txt =textscan(fid,'%s','delimiter','\n');
56 lines = txt{1,1};
57 before = find(ismember(lines,'*Beam Section, elset="Frame ...
       Instance__I2", material="Frame Material", poisson = 0.33, ...
       temperature=GRADIENTS, section=PIPE'));
58 after = find(ismember(lines,'** PART INSTANCE: Skin Instance'));
```

```
59 results = lines(before+1:after-1);
60 fclose(fid);
61 frame_dim = results(1);
62
63 % convert dimensions from string to double
64 b = regexp(frame_dim,'\d+(\.)?(\d+)?','match');
65 frame_dim=str2double([b{:}]);
66
67 % frame dimension
68 r_frame = frame_dim(1); % radius of beam (frame) (meters)
69 t_frame = frame_dim(2); % thickness of beam (frame) (meters)
70
71 %% read in skin dimensions (thickness) from .inp file
72 fid=fopen('Sample.inp');
73 txt =textscan(fid,'%s','delimiter','\n');
74 lines = txt{1,1};
75 before = find(ismember(lines,'*Membrane Section, elset="Skin ...
       Instance__PickedSet31", material="Skin Material", poisson=0.33'));
76 after = find(ismember(lines,'*System'));
77 results = lines(before+1:after-1);
78 fclose(fid);
79 skin_dim = results(1);
80
81 % convert dimensions from string to double
82 b = regexp(skin_dim,'\d+(\.)?(\d+)?','match');
83 skin_dim=str2double([b{:}]);
84
85 % skin thickness
86 t_skin = skin_dim(1)*10^(-skin_dim(2)); % thickness of skin (m)
87
88 %% print part dimensions (pipe radius/thickness and skin thickness)
89 fprintf('Frame Radius: %4.2e m\n\n',r_frame)
```

```
90 fprintf('Frame Thickness: %4.2e m\n\n',t_frame)
91
92 fprintf('Skin Thickness: %4.2e m\n\n',t_skin)
93
94 fprintf('-----------------------------------------------------------------\n')
95 fprintf('RESULTS\n');
96 fprintf('-----------------------------------------------------------------\n\n')
97
98 %% read in frame material's density from .inp file
99 fid=fopen('Sample.inp');
100 txt =textscan(fid,'%s','delimiter','\n');
101 lines = txt{1,1};
102 before = find(ismember(lines,'*Material, name="Frame Material"'));
103 after = find(ismember(lines,'*Elastic'));
104 results = lines(before+2:after-1);
105 fclose(fid);
106 frame_dens = results(1);
107
108 % convert density from string to double
109 b = regexp(frame_dens,'\d+(\.)?(\d+)?','match');
110 frame_prop=str2double([b{:}]);
111
112 % frame material's density
113 rho_frame = frame_prop(1); % mass density of frame material (kg/m^3);
114
115 %% read in skin material's density from .inp file
116 fid=fopen('Sample.inp');
117 txt =textscan(fid,'%s','delimiter','\n');
118 lines = txt{1,1};
119 before = find(ismember(lines,'*Material, name="Skin Material"'));
120 after = find(ismember(lines,'** STEP: ...
       Nonlinear-Static,General-wStabi'));
```

```
121 results = lines(before+2:after-1);
122 fclose(fid);
123 skin_dens = results(1);
124
125 % convert density from string to double
126 b = regexp(skin_dens,'\d+(\.)?(\d+)?','match');
127 skin_prop=str2double([b{:}]);
128
129 % skin material's density
130 rho_skin = skin_prop(1); % mass density of frame material (kg/m^3);
131
132 %% read number of skin nodes from .inp
133 fid=fopen('Sample.inp');
134 txt =textscan(fid,'%s','delimiter','\n');
135 lines = txt{1,1};
136 before = find(ismember(lines,'** PART INSTANCE: Skin Instance'));
137 after = find(ismember(lines,'*Element, type=M3D4R'));
138 results = lines(before+3:after-2);
139 fclose(fid);
140 nodes = results;
141
142 % convert to double
143 b = regexp(nodes,'(\-)?\d+(\.)?(\d+)?','match');
144 last_node=str2double([b{end}]);
145 first_node=str2double([b{1}]);
146
147 % node 1 coord (x,y,z)
148 num_of_skin_nodes = (last_node(1)-first_node(1))+1;
149
150 %% read number of frame nodes from .inp
151 fid=fopen('Sample.inp');
152 txt =textscan(fid,'%s','delimiter','\n');
```

```
153 lines = txt{1,1};
154 before = find(ismember(lines,'** PART INSTANCE: Frame Instance'));
155 after = find(ismember(lines,'*Element, type=B31'));
156 results = lines(before+3:after-2);
157 fclose(fid);
158 nodes = results;
159
160 % convert to double
161 b = regexp(nodes,'(\-)?\d+(\.)?(\d+)?','match');
162 last_node=str2double([b{end}]);
163 first_node=str2double([b{1}]);
164
165 % node 1 coord (x,y,z)
166 num_of_frame_nodes = (last_node(1)-first_node(1))+1;
167
168
169 % %% read in frame's nodal coordinates (pre-deformation) from .inp ...
      file and scale for diamter (based off of 1ft ref diameter)
170 % for i = 1:num_of_frame_nodes
171 %
172 % fid=fopen('Sample.inp');
173 % txt =textscan(fid,'%s','delimiter','\n');
174 % lines = txt{1,1};
175 % before = find(ismember(lines,'** PART INSTANCE: Frame Instance'));
176 % after = find(ismember(lines,'*Element, type=B31'));
177 % results = lines(before+3:after-2);
178 % fclose(fid);
179 % frame_node_locs= results;
180 %
181 % % convert to double
182 % b = regexp(frame_node_locs,'(\-)?\d+(\.)?(\d+)?','match');
183 % frame_node=str2double([b{i}]);
```

```
% frame_node_num(i) = frame_node(1);
% frame_node_x(i) = frame_node(2);
% frame_node_y(i) = frame_node(3);
% frame_node_z(i) = frame_node(4);
% end
%
% nodal_coord_frame = ...
    [frame_node_num',Diameter_ft*frame_node_x',Diameter_ft*frame_node_y',Diameter_ft*fra
     % frame's nodal coord (numbered) (m) scaled
%
% %% edit .inp file for new frame nodal coord
% fid=fopen('Sample.inp');
% txt =textscan(fid,'%s','delimiter','\n');
% lines = txt{1,1};
% before = find(ismember(lines,'** PART INSTANCE: Frame Instance'));
% after = find(ismember(lines,'*Element, type=B31'));
% fclose(fid);
%
% a = nodal_coord_frame';
% % print new frame nodal coord
% M_before = rows(before+3:after-2);
% M = sprintf('%3.0f, %0.10f, %0.10f, %0.10f\n',a(:));
% rows = [rows(1:(before+2)); M; rows((after):end);];
% fid = fopen('Sample.inp','wt');
% fprintf(fid,'%s\n', rows{:});
% fclose(fid);

% %% read in skin's nodal coordinates (pre-deformation) from .inp ...
    file and scale for diameter
% for i = 1:num_of_skin_nodes
%
% fid=fopen('Sample.inp');
```

```
213 % txt =textscan(fid,'%s','delimiter','\n');
214 % lines = txt{1,1};
215 % before = find(ismember(lines,'** PART INSTANCE: Skin Instance'));
216 % after = find(ismember(lines,'*Element, type=M3D4R'));
217 % results = lines(before+3:after-2);
218 % fclose(fid);
219 % skin_node_locs= results;
220 %
221 % % convert to double
222 % b = regexp(skin_node_locs,'(\-)?\d+(\.)?(\d+)?','match');
223 % skin_node=str2double([b{i}]);
224 % skin_node_num(i) = skin_node(1);
225 % skin_node_x(i) = skin_node(2);
226 % skin_node_y(i) = skin_node(3);
227 % skin_node_z(i) = skin_node(4);
228 % end
229 %
230 % nodal_coord_skin = ...
      [skin_node_num',Diameter_ft*skin_node_x',Diameter_ft*skin_node_y',Diameter_ft*skin_n
       % skin's nodal coord (numbered) scaled (*2) (m)
231 %
232 % %% edit .inp file for new skin nodal coord
233 % fid=fopen('Sample.inp');
234 % txt =textscan(fid,'%s','delimiter','\n');
235 % lines = txt{1,1};
236 % before = find(ismember(lines,'** PART INSTANCE: Skin Instance'));
237 % after = find(ismember(lines,'*Element, type=M3D4R'));
238 % fclose(fid);
239 %
240 % b = nodal_coord_skin';
241 %
242 % % print new skin nodal coord
```

```
243 % M_before = rows(before+3:after-2);
244 % M = sprintf('%3.0f, %0.10f, %0.10f, %0.10f\n',b(:));  %Change ...
       t_skin in INP file
245 % rows = [rows(1:(before+2)); M; rows((after):end);];
246 % fid = fopen('Sample.inp','wt');
247 % fprintf(fid,'%s\n', rows{:});
248 % fclose(fid);
249
250
251 %% read in skin's new nodal coordinates (pre-deformation) from .inp file
252 for i = 1:num_of_skin_nodes
253
254 fid=fopen('Sample.inp');
255 txt =textscan(fid,'%s','delimiter','\n');
256 lines = txt{1,1};
257 before = find(ismember(lines,'** PART INSTANCE: Skin Instance'));
258 after = find(ismember(lines,'*Element, type=M3D4R'));
259 results = lines(before+3:after-2);
260 fclose(fid);
261 node_locs= results;
262
263 %convert to double
264 b = regexp(node_locs,'(\-)?\d+(\.)?(\d+)?','match');
265 skin_node=str2double([b{i}]);
266 skin_node_num(i) = skin_node(1);
267 skin_node_x(i) = skin_node(2);
268 skin_node_y(i) = skin_node(3);
269 skin_node_z(i) = skin_node(4);
270 end
271
272 undef_skin_coords = [skin_node_x',skin_node_y',skin_node_z'];    % ...
       skin's nodal coordinates before deformation (m)
```

```
273
274 % edit .inp file for desired outputs in .dat file
275 fid=fopen('Sample.inp');
276 txt =textscan(fid,'%s','delimiter','\n');
277 Orows = txt{1,1};
278 Oirows_begin = find(ismember(Orows,'*Output, history, ...
       variable=PRESELECT'));
279 Oirows_end = find(ismember(Orows,'*End Step'));
280 fclose(fid);
281
282 OM = sprintf('**\n*EL PRINT, FREQUENCY=1000000\nMISES\n**\n*NODE ...
       PRINT, FREQUENCY=1000000\nU');  % request to print elemental von ...
       mises stress and nodal deformation
283 Orows = [Orows(1:Oirows_begin); OM; Orows(Oirows_end:end);];
284
285 fid = fopen('Sample.inp','wt');
286 fprintf(fid, '%s\n', Orows{:});
287 fclose(fid);
288
289 %% run .inp file w/6 processors
290 t = {'Sample'}; % .inp file names
291 for i = 1
292 string = strcat('abaqus job=',t{i},' cpus=6'); % make sure the job ...
       name uses squiggly brackets
293 dos(string) % this will run the string in the command line
294 end
295
296 % %%terminate job if errors occur
297 % for i = 1
298 % string = strcat('abaqus terminate job=',t{i}); % make sure the job ...
       name uses squiggly brackets
299 % dos(string) % this will run the string in the command line
```

```
% end


%% read in max von mises stress for the frame part from .dat file
fid=fopen('Sample.dat');
txt =textscan(fid,'%s','delimiter','\n');
lines = txt{1,1};
before = find(ismember(lines,'THE FOLLOWING TABLE IS PRINTED FOR ALL ...
    ELEMENTS WITH TYPE B31 AT THE INTEGRATION POINTS'));
after = find(ismember(lines,'THE FOLLOWING TABLE IS PRINTED FOR ALL ...
    ELEMENTS WITH TYPE M3D4R AT THE INTEGRATION POINTS'));
results = lines(before+2:after-8);
fclose(fid);
frame_max = results(end);

% convert to double
b = regexp(frame_max,'\d+(\.)?(\d+)?','match');
Max_VM_Frame=str2double([b{:}]);

% frame's max vm stress
Max_VM_Frame = Max_VM_Frame(1)*10^(Max_VM_Frame(2));  % maximum VM ...
    stress in the frame (Pa)

% calculate frame's factor of safety
FS_frame = Sy_frame/Max_VM_Frame;

% print factor of safety (frame)
fprintf('Factor of Safety (Frame) = %4.2f\n\n',FS_frame)

%% read in max von mises stress for the skin part from .dat file
fid=fopen('Sample.dat');
txt =textscan(fid,'%s','delimiter','\n');
```

```
329 lines = txt{1,1};
330 before = find(ismember(lines,'THE FOLLOWING TABLE IS PRINTED FOR ALL ...
       ELEMENTS WITH TYPE M3D4R AT THE INTEGRATION POINTS'));
331 after = find(ismember(lines,'N O D E   O U T P U T'));
332 results = lines(before+2:after-9);
333 fclose(fid);
334 skin_max = results(end);
335
336 % convert  string to double
337 b = regexp(skin_max,'\d+(\.)?(\d+)?','match');
338 Max_VM_Skin=str2double([b{:}]);
339
340 % skin's max vm stress
341 Max_VM_Skin = Max_VM_Skin(1)*10^(Max_VM_Skin(2));  % maximum VM ...
       stress in the skin (Pa)
342
343 % calculate skin's factor of safety
344 FS_skin = Sy_skin/Max_VM_Skin;
345
346 % print factor of safety (skin)
347 fprintf('Factor of Safety (Skin) = %4.2f\n\n',FS_skin)
348
349 %% read in skin's deformation (U) values from .dat file
350 for i = 1:(num_of_skin_nodes)
351
352 fid=fopen('Sample.dat');
353 txt =textscan(fid,'%s','delimiter','\n');
354 lines = txt{1,1};
355 before = find(ismember(lines,'THE FOLLOWING TABLE IS PRINTED FOR ALL ...
       NODES'));
356 results = ...
       lines(((before+(3+num_of_frame_nodes+2))):((before+(3+num_of_frame_nodes+2+num_of_sk
```

```
357 fclose(fid);
358 deformations = results;
359
360 % convert to double
361 b = regexp(deformations,'(\-)?\d+(\.)?(\d+)?','match');
362 U=str2double([b{i}]);
363
364 U_x(i) = U(2)*10^(U(3));
365 U_y(i) = U(4)*10^(U(5));
366 U_z(i) = U(6)*10^(U(7));
367 end
368
369 nodal_U = [U_x',U_y',U_z']; % skin's nodal coordinates before ...
       deformation (m)
370
371 %% add skin's deformation values to pre-def nodal coordinates to ...
       give nodal coordinates after deformation
372 def_skin_coords = undef_skin_coords + nodal_U;       % coordinates ...
       corresponding to the nodes of the deformed skin
373
374 %% weight calculations
375 structureRadius = Diameter_m/2;    % radius of structure (meters)
376 circum = 2*pi*structureRadius;  % circumference of the sphere (meters)
377
378 v_ring = (pi*(r_frame^2-(r_frame-t_frame)^2)*circum); % volume of an ...
       individual ring (m^3)
379 v_ring_intersect = ...
       ((6*(2-1)*((2*(r_frame-(r_frame-t_frame)))/cosd(0))*pi*(r_frame^2-(r_frame-t_frame)^
       % volume of intersections (m^3)
380 v_frame = (v_ring*9)-(v_ring_intersect);    % volume of frame (m^3)
381
382 SA_skin = 0.00608;  % surface area of skin section taken from query ...
```

```
    function in CAE (m^2) for 1 ft diam
383
384 SA_skin_scaled = 4*pi*(Diameter_ft*sqrt(((48*SA_skin)/(4*pi))))^2;  ...
    % surface area of skin for 2 ft diameter
385
386 v_skin = SA_skin_scaled*t_skin;  % volume of skin (m^3)
387
388 w_frame = v_frame*rho_frame*g0; % weight of frame (N)
389 w_skin = v_skin*rho_skin*g0;    % weight of skin (N)
390
391 W = w_frame+w_skin;     % total weight of the structure (N)
392
393 %% buoyancy calculations
394 % initial volume enclosed before deformation
395
396 DTs = delaunayTriangulation(undef_skin_coords);
397 [K,v] = convexHull(DTs);
398
399 v_i = v + (0.5*v_skin);     % initial enclosed volume excluding skin ...
    thickness and frame volume (m^3) (v_skin halved to account for ...
    midsection located at the coord of sphere of same radius)
400
401 % volume enclosed after deformation
402 coord1s = def_skin_coords(1:end,1);
403 coord2s = def_skin_coords(1:end,2);
404 coord3s = def_skin_coords(1:end,3);
405
406 Pskin = [coord1s, coord2s, coord3s];
407 DTs = delaunayTriangulation(Pskin);
408
409 [K,v] = convexHull(DTs);
410 volume_skin_def = v;    % volume enclosed by the coordinates ...
```

```
    corresponding to the nodes of the deformed skin (m^3)
411
412 v_deformed = v + (0.5*v_skin);    % internal volume after ...
    deformation (m^3)
413
414 B_i = v_i*rho_air*g0;       % buoyancy before deformation (N)
415 B_f = v_deformed*rho_air*g0;  % buoyancy after deformation  (N)
416
417
418 %% final weight to buoyancy ratio (frame)
419 WB_frame = w_frame/B_f;
420 fprintf('Weight to Buoyancy Ratio (Frame) = %4.4f\n\n',WB_frame)
421
422 %% final weight to buoyancy ratio (skin)
423 WB_skin = w_skin/B_f;
424 fprintf('Weight to Buoyancy Ratio (Skin) = %4.4f\n\n',WB_skin)
425
426 %% weight:buoyancy after deformation
427 WB_f = W/B_f;     % weight to buoyancy ratio after deformation
428
429 % print final weight to buoyancy ratio
430 fprintf('Total Weight to Buoyancy Ratio = %4.2f\n\n',WB_f)
```

```
-------------------------------------------------
MODEL
-------------------------------------------------

Frame Material: Carbon Nanotube (CNT) Composite

Skin Material : Graphene

Diameter: 2.63 ft (0.8001 m)

Frame Radius: 8.00e-03 m

Frame Thickness: 2.00e-04 m

Skin Thickness: 8.00e-07 m

-------------------------------------------------
RESULTS
-------------------------------------------------

Factor of Safety (Frame) = 1.57

Factor of Safety (Skin) = 1.52

Weight to Buoyancy Ratio (Frame) = 0.8894

Weight to Buoyancy Ratio (Skin) = 0.0102

Total Weight to Buoyancy Ratio = 0.8996
```

Figure B.1. Sample Matlab results output

Bibliography

[1] *Abaqus Analysis User's Manual*, Dassault Systémes, 2014.

[2] B. Cranston, "Conceptual design, structural analysis, and design space exploration of a vacuum lighter than air vehicle," Ph.D. dissertation, Air Force Institute of Technology, Wright Patterson AFB, Ohio, 2014.

[3] D. Noel, "Lighter than air craft using vacuum," *Correspondence, Speculations in Science and Technology*, vol. 6, no. 3, p. 262–266, 1983.

[4] (2016, May) What goes up. [Online]. Available: https://www.library.wisc.edu/specialcollections/2016/05/19/what-goes-up/

[5] T. T. Metlen, "Design of a lighter than air vehicle that achieves positive buoyancy in air using a vacuum," Master's thesis, Air Force Institute of Technology, Wright Patterson AFB, Ohio, 2012.

[6] B. Cranston, M. AlGhofaily, and A. Palazotto, "Design and structural analysis of unique structures under an internal vacuum," *Aerospace Science and Technology*, vol. 68, p. 68–76, 2017.

[7] J. Schwemmer, "Optimal design of a hexakis icosahedron vacuum based lighter than air vehicle," Master's thesis, Air Force Institute of Technology, Wright Patterson AFB, Ohio, 2017.

[8] J. Schwemmer, A. Palazotto, and J. Chrissis, "Optimal design of a hexakis icosahedron vacuum based lighter than air vehicle," 2016.

[9] K. Kendig, *Sink or Float?: Thought Problems in Math and Physics*, 1st ed. Mathematical Association of America, 2008, vol. 33.

[10] (2014, January) Archimedes' principle. [Online]. Available: https://physics.weber.edu/carroll/archimedes/principle.htm

[11] Y. Deng and P. Wang, *Ancient Chinese inventions: 3000 years of science and technology.* China Intercontinental Press, 2008.

[12] L. Ege, *Balloons and Airships.* London, United Kingdom: Macmillan, 1974.

[13] D. H. Robinson, *Giants in the Sky: A History of the Rigid Airship.* Henley-On-Thames: G T Foulis & Co Ltd, 1973.

[14] (2013, July) Zeppelin. [Online]. Available: https://bluejayblog.wordpress.com/2013/07/08/zeppelin/

[15] M. Crawford, "Dismantling the helium empire," *Science*, vol. 237, no. 4812, pp. 238–240, 1987.

[16] T. H. F. Lana-Terzi and J. Ledeboer, *The Aerial Ship.* Nabu Press, 2010.

[17] A. Akhmeteli and A. Gavrilin, "Layered shell vacuum balloons," Feb. 23 2006, uS Patent App. 11/127,613. [Online]. Available: http://www.google.com/patents/US20060038062

[18] L. W. Just, "Dynamic response analysis of an icosahedron shaped lighter than air vehicle," Master's thesis, Air Force Institute of Technology, Wright Patterson AFB, Ohio, 2015.

[19] L. Just and A. N. Palazotto, "The evaluation of an icosahedron' eigenvalue," *57th AIAA/ASCE/AHS/ASC Structures, Structural Dynamics and Materials Conference*, 2016. [Online]. Available: http://dx.doi.org/10.2514/6.2016-0202

[20] *U.S. Standard Atmosphere.* National Aeronautics and Space Administration, 1976.

[21] J. W. Snyder, "A study of quasi-static and dynamic analyses of a hexakis icosahedron frame for use in a vacuum lighter-than-air vehicle," Master's thesis, Air Force Institute of Technology, Wright Patterson AFB, Ohio, 2017.

[22] J. Snyder and A. N. Palazotto, "A study of quasi-static and dynamic analyses of a hexakis icosahedron frame for use in a vacuum lighter-than-air vehicle," *58th AIAA/ASCE/AHS/ASC Structures, Structural Dynamics and Materials Conference*, pp. 1–12, 2017.

[23] R. Adorno-Rodriguez, "Nonlinear structural analysis of an icosahedron and its application to lighter than air vehicles under a vacuum," Master's thesis, Air Force Institute of Technology, Wright Patterson AFB, Ohio, 2014.

[24] R. Adorno-Rodriguez and A. N. Palazotto, "Nonlinear structural analysis of an icosahedron under an internal vacuum," *57th AIAA/ASCE/AHS/ASC Structures, Structural Dynamics and Materials Conference*, pp. 878–883, 2015. [Online]. Available: http://dx.doi.org/10.2514/1.C033284

[25] M. AlGhofaily, "Finite element analysis and experimentation of an icosahedron frame under compression," Master's thesis, Air Force Institute of Technology, Wright Patterson AFB, Ohio, 2015.

[26] (2017) Copper, cu; cold-worked. [Online]. Available: http://www.matweb.com/search/DataSheet.aspx?MatGUID=ca486cc7cefa44d98ee67d2f5eb7d21f

[27] R. D. Cook, D. S. M. M. E. Plesha, and R. J. Witt, *Concepts and Applications of Finite Element Analysis*, 4th ed. New York, NY: John Wiley & Sons Inc., 2002.

[28] (2004) Chapter 4: Entrances, doors, and gates. [Online]. Available: https://www.access-board.gov/guidelines-and-standards/buildings-and-sites/

about-the-ada-standards/guide-to-the-ada-standards/chapter-4-entrances,
-doors,-and-gates

REPORT DOCUMENTATION PAGE

Form Approved
OMB No. 0704–0188

1. REPORT DATE *(DD–MM–YYYY)*	2. REPORT TYPE	3. DATES COVERED *(From — To)*
22 March 2018	Master's Thesis	September 2016 — March 2018

4. TITLE AND SUBTITLE

QUASI-STATIC NONLINEAR ANALYSIS OF A CELESTIAL ICOSAHEDRON SHAPED VACUUM LIGHTER THAN AIR VEHICLE

5a. CONTRACT NUMBER

5b. GRANT NUMBER

5c. PROGRAM ELEMENT NUMBER

6. AUTHOR(S)

Moore, Kyle D. 2d Lt, USAF

5d. PROJECT NUMBER

5e. TASK NUMBER

5f. WORK UNIT NUMBER

7. PERFORMING ORGANIZATION NAME(S) AND ADDRESS(ES)

Air Force Institute of Technology
Graduate School of Engineering and Management (AFIT/EN)
2950 Hobson Way
WPAFB OH 45433-7765

8. PERFORMING ORGANIZATION REPORT NUMBER

AFIT-ENY-MS-18-M-280

9. SPONSORING / MONITORING AGENCY NAME(S) AND ADDRESS(ES)

Air Force Office of Scientific Research
875 North Randolph Street, Suite 325 Room 3112
Arlington, VA 22203-1768
Dr. Jaimie Tiley
jaimie.tiley@usaf.mil

10. SPONSOR/MONITOR'S ACRONYM(S)

AFOSR

11. SPONSOR/MONITOR'S REPORT NUMBER(S)

12. DISTRIBUTION / AVAILABILITY STATEMENT

DISTRIBUTION STATEMENT A:
APPROVED FOR PUBLIC RELEASE; DISTRIBUTION UNLIMITED.

13. SUPPLEMENTARY NOTES

14. ABSTRACT

Due to the many drawbacks associated with a traditional lighter than air vehicle, there is a desire for a vacuum lighter than air vehicle which generates lift from an internal vacuum. To date, two feasible designs (the icosahedron and the hexakis icosahedron) for this so called vacuum lighter than air vehicle have been studied at the Air Force Institute of Technology. This research looks to show the feasibility of a new design for a vacuum lighter than air vehicle, the celestial icosahedron. This research includes a boundary condition study which proves the symmetric nature of the celestial icosahedron's frame with laterally constrained and unconstrained vertices. This research also presents three feasible designs of various structural diameters (0.8001, 1.2192, and 0.7576 meters) for the celestial icosahedron.

15. SUBJECT TERMS

Finite Element Analysis, Lighter than Air Vehicles, Structural Analysis, Nonlinear Quasi-Static

16. SECURITY CLASSIFICATION OF:			17. LIMITATION OF ABSTRACT	18. NUMBER OF PAGES	19a. NAME OF RESPONSIBLE PERSON
a. REPORT	b. ABSTRACT	c. THIS PAGE			Dr. A. Palazotto, AFIT/ENY
U	U	U	UU	122	19b. TELEPHONE NUMBER *(include area code)* (937) 785-3636 x4599; anthony.palazotto@afit.edu